THE DEVELOPMENT AND EVALUATION OF MULTI-MODAL TARGETED AND NON-TARGETED MICROBUBBLES

THE DEVELOPMENT AND EVALUATION OF MULTI-MODAL MICROBUBBLES AND NEW STRATEGIES FOR TARGETED ULTRASOUND, NUCLEAR AND OPTICAL IMAGING

By

AIMEN ZLITNI, B.Sc.

A Thesis

Submitted to the School of Graduate Studies

In Partial Fulfillment of the Requirements

For the Degree

Doctor of Philosophy

McMaster University

DOCTOR OF PHILOSOPHY (2016) McMaster University

Chemical Biology Hamilton, Ontario

TITLE: The Development and Evaluation of Multi-Modal Microbubbles and New Strategies for Targeted Ultrasound, Nuclear and Optical Imaging

AUTHOR: Aimen Zlitni, B.Sc. (King Saud University)

SUPERVISOR: Professor John Fitzmaurice Valliant

Number of Pages: XXXV, 212

Abstract

Gas filled microbubbles (MBs) stabilized by a shell (e.g. lipids) are commonly used as ultrasound (US) contrast agents. Attaching biomolecules to the surface of MBs allows for molecular US imaging of various diseases. With the increased interest in targeted US imaging, new platforms to prepare disease-targeted MBs are necessary. Furthermore, attaching signaling agents to MBs creates multi-modal imaging opportunities, enhancing visualization and quantification of disease biomarkers.

In this thesis, MBs labeled with ^{99m}Tc and/or rhodamine dye by taking advantage of the strong interaction between biotin and streptavidin are reported. Radiolabeling of MBs was achieved in good radiochemical yield (~ 30%). ^{99m}Tc-labeled MBs were targeted to vascular endothelial growth factor receptor 2 (VEGFR2) using an anti-VEGFR2 antibody and to prostate specific membrane antigen (PSMA) using small-molecule based PSMA inhibitors. *In vitro* evaluations showed successful binding of MBs to the target while *in vivo* targeting assessments were unsuccessful.

New strategies to target MBs to the site of interest were then developed through the use of the bioorthogonal reaction between tetrazine (Tz) and trans-cyclooctene (TCO). A biotinylated derivative of Tz was loaded on streptavidin coated MBs to create a Tz-derivatized MB (MB_{Tz}). Targeting MB_{Tz} to extracellular markers of cancer such as VEGFR2, PSMA and urokinase

plasminogen activator receptor (uPAR) *in vitro* was achieved using TCO-conjugated antibodies. *In vivo* targeting was successful for VEGFR2 and PSMA, but not uPAR.

Translating the new strategy to other US contrast agents was then investigated. Gas vesicles (GVs) produced in *halobacteria* were conjugated with TCO using amide-coupling chemistry. A ^{99m}Tc-labeled derivative of Tz was loaded on TCO-GVs (RCY= 59%) and their distribution assessed by SPECT/CT imaging and *ex vivo* tissue counting. Having established a convenient platform to conjugate molecules to GVs and MBs, future work focuses on developing a new generation of human compatible molecular US imaging probes.

Acknowledgments

I would like to thank my supervisor, Dr. John Valliant, for giving me this great opportunity to conduct my graduate research in his lab. The amount of experience I gained is immeasurable. Thank you for providing me with a beautiful project that needed a lot of creativity and "thinking outside the box"; for giving me so much independence yet providing me with guidance throughout my graduate work; for allowing me to learn and get hands on experience with all the interdisciplinary fields necessary in my project and for always reminding me that "we must learn to walk before we can run". This and many other lessons with life and science will stay with me forever.

I would like to thank my committee members, Dr. Fred Capretta and Dr. Harald Stöver for their guidance and constructive feedback, as well as Dr. Stuart Foster and Melissa Yin for their help and advice with all ultrasound imaging experiments.

I would like to extend my gratitude to my beautiful family for their unconditional love, motivation and support: my mom and dad for always being there for me and for pushing me to reach the stars; my aunt Fatin (aka: Tanta); my big sis Soumaya for her constant support and being a great role model (and a tough act to follow lol), my lil sis (not so little anymore) for always providing me with the support, the good chats and making me look or sound old every now and then.

I also thank past and present members of the Valliant research group whom contributed to this pleasant experience. More specifically, I want to thank Dr. Chitra Sundarajan and Dr. Anika Louie for providing me with all the guidance and help when I first started in the lab; Dr. Afaf Genady whom I was lucky to work and collaborate with during my project, I owe a lot of my knowledge and skills in organic synthesis to you; the biologists in the group, Shannon Czorny, Megan Blacker and Nancy Janzen (aka: SHMANCY) for all their hands-on training and help with any biology-related experiments; CPDC group, Dr. Ryan Simms, Dr. John Forbes, Dr. Matt Moran, Dr. Bob Wu, Dr. Alla Darwish and Dr. Stuart Mahoney for all the scientific discussions and advice; Peter Cooper and Lily Southcott for being awesome thesis students to supervise; and finally Laura Banevicius, Dr. James Dzandzi, Holly, Sam and ZoyNab for their constant support and unconditional friendship.

I would like to extend special thanks to members of the Department of Chemistry and Chemical Biology, more specifically Tammy Feher (aka: Momma Tammy) for her constant administrative support and genuinely caring attitude; the Chem. office staff, and all the great friends I met in this university, noteably Dr. Vinodh Rajendra, Dr. Brad Cowie, Danith Dissanayake, Greg Bahun, Nikki Banko, Justin Liddycoat, Vanessa Mestre, Heidi Stoute and the Kelly's.

Last but not least, I would like to thank my better half Christina Petlura, for providing unwavering support, encouragement, nutritional advice ☺ and

patience throughout my graduate school experience. You are my rock and you bring out the best of me xoxo.

Dedication

I would like to dedicate this dissertation to all the loved ones who couldn't share this beautiful experience with us: My grand parents: Mimi, Zouzou and Oummi; as well as my dear friend Yurij Petlura. You might be gone but your memories will live in our hearts and minds forever.

Publications

Peer reviewed journal articles

(125)I-Tetrazines and Inverse-Electron-Demand Diels-Alder Chemistry: A Convenient Radioiodination Strategy for Biomolecule Labeling, Screening, and Biodistribution Studies.

Silvia A. Albu, Salma A. Al-Karmi, Alyssa Vito, James P. K. Dzandzi, **Aimen Zlitni**, Denis Beckford-Vera, Megan Blacker, Nancy Janzen, Ramesh M. Patel, Alfredo Capretta,, and John F. Valliant. Bioconjugate Chemistry 2016; 27: 207–216.

Synthesis, Characterization and Radiolabeling of Carborane-Functionalized Tetrazines for Use in Inverse Electron Demand Diels-Alder Ligation Reactions.

Afaf R. Genady, Joanne Tan, Mohamed E. El-Zaria, **Aimen Zlitni**, Nancy Janzen, and John F. Valliant. Journal of Organometallic Chemistry 2015; 791: 204-213.

Catching Bubbles: Targeting Ultrasound Microbubbles Using Bioorthogonal

Inverse-Electron-Demand Diels-Alder Reactions.

Aimen Zlitni, Nancy Janzen, F. Stuart Foster and John F. Valliant. *Angew. Chem. Int. Ed. Engl.* 2014, *53*, 6459–6463.

The synthesis, magnetic purification and evaluation of (99m)Tc-labeled microbubbles.

Neva Lazarova, Patrick W Causey, Jennifer A Lemon, Shannon K Czorny, John R Forbes, **Aimen Zlitni**, Afaf Genady, F Stuart Foster, John F Valliant. Nucl Med Biol. 2011; 38(8):1111-18.

Published meeting abstracts

The preparation and preclinical evaluation of ^{99m}Tc-labeled microbubbles for bimodal ultrasound and SPECT imaging.

Aimen Zlitni, Afaf R. Genady, Nancy Janzen and John F. Valliant. Nucl Med Biol. 2014; 41(7): 628.

Synthesis, Characterization and Imaging of a ^{99m}Tc(I)-Tetrazine Tridentate Ligand Complex for Bioorthogonal Chemistry.

Zainab Ahmad, Megan Blacker, **Aimen Zlitni**, Holly Bilton, John Valliant. J. Label. Compd. Radiopharm. 58 (2015) S138.

Manuscripts ready for submission

The Development and Evaluation of Prostate Specific Membrane Antigen (PSMA)-Targeted US Microbubbles using Bioorthogonal Chemistry.

Aimen Zlitni, Melissa Yin, Nancy Janzen, Stuart Foster and John F. Valliant. Journal of Cancer Research.

Manuscripts in preparation for submission

The development of a new sequence for targeted US imaging using tetrazine-coated microbubbles and bioorthogonal chemistry.

Aimen Zlitni*, Melissa Yin*, John F. Valliant and Stuart Foster. Journal of Ultrasound in Medicine and Biology as a technical note.

*Co-authors

***In Vivo* Biodistribution of Radiolabeled Gas Vesicles in Mice using Single Photon Emission Computed Tomography (SPECT) and MicroCT.**

Johann Le Floc'h, **Aimen Zlitni**, Melissa Yin, Holly Bilton, Mikhail G. Shapiro, John Valliant, Stuart F. Foster. Journal of Ultrasound in Medicine and Biology.

Patents

Targeted Molecular Imaging Contrast Agents.

John F. Valliant and **Aimen Zlitni**. Aug 2015, WO/2015/117235A1

Table of contents

List of Figures

List of Supporting Figures

List of Tables

List of Schemes

List of Abbreviations

A

ACN:	Acetonitrile
aq:	Aqueous
AREB:	Animal Research Ethics Board
a.u.:	Arbitrary unit
Å:	Angstrom

B

BCA:	Bicinchoninic acid
BFC:	Bifunctional chelate
Biotin-TFP-ester:	Biotin tetrafluorophenyl ester
Boc:	ter-butoxycarbonyl
BSA:	Bovine serum albumin

C

Cbz:	Carbobenzyloxy
$CDCl_3$:	Deuterated chloroform
CD_3OD:	Deuterated methanol
Ci:	Curie
CMC:	Critical micelle concentration
CNS:	Central nervous system
CPM:	Counts per minute
CT:	Computed tomography
Cy5:	Cyanine 5 dye
δ:	Chemical shift (NMR)

D

DCM:	Dichloromethane
DIC:	N,N'-diisopropylcarbodiimide
DIPEA:	Diisopropylethylamine
DMACA:	4-(Dimethylamino)cinnamaldehyde
DMF:	Dimethylformamide
DMPC:	Dimyristoyl phosphatidylcholine
DMSO:	Dimethyl sulfoxide
DNP:	2,4-Dinitro phenyl
DPPA:	Dipalmitoyl phosphoric acid
DPPC:	Dipalmitoyl phosphatidylcholine
DPPG:	Dipalmitoyl phosphatidylglycerol
DSPC:	Distearoyl phosphatidylcholine
dTE:	Differential targeted enhancement
E	
EDTA:	Ethylenediaminetetraacetic acid
ESI-MS:	Electrospray ionization- mass spectrometry
EtOH:	Ethanol
F	
FBS:	Fetal Bovine Serum
FDA:	Food and Drug Administration
FITC:	Fluorescein isothiocyanate
Fmoc:	Fluorenylmethyloxycarbonyl
G	
Glu:	Glutamic acid
GBq:	Giga-Bequerel

GPI:	Glycosyl-phosphatidylinositol
GVs:	Gas vesicles
γ:	Gamma
H	
HATU:	O-(7-Azabenzotriazol-1-yl)-N,N,N',N'-tetramethyluronium hexafluorophosphate
HIFU:	High intense focus ultrasound
HOAt:	1-Hydroxy-7-azabenzotriazole
HPLC:	High performance liquid chromatography
hr:	Hour(s)
HRMS:	High-resolution mass spectrometry
HSA:	Human Serum Albumin
Hz:	Hertz
I	
ICAM-1:	Intercellular adhesion molecule-1
%ID/g:	Percentage injected dose per gram
IgG:	Immunoglobulin G
J	
J:	Coupling constant (NMR)
K	
kBq:	kiloBecquerel
K_d:	Dissociation constant
kDa:	kiloDalton
keV:	Kiloelectron volt
L	
Lys:	Lysine

M

Mad-CAM-1:	Mucosal addressin cellular adhesion molecule-1
MALDI-TOF MS:	Matrix Assisted Laser Desorption/Ionization-Time Of Flight Mass Spectrometry
MBs:	Microbubbles
MeOH:	Methanol
MI:	Molecular Imaging
min:	Minute(s)
MPEG 5000-DPPE:	Polyethyleneglycol 5000-Dipalmitoyl phosphatidylethanolamine
MRI:	Magnetic Resonance Imaging

N

NAALADase:	N-acetylated-γ-linked-acidic dipeptidase
NMR:	Nuclear magnetic resonance

P

PA:	Palmitic Acid
PBS:	Phosphate buffered saline
PEG:	Polyethylene glycol
PET:	Positron Emission Tomography
PLGA:	Poly(lactic-co-glycolic acid)
PMPA:	2-(phosphonomethyl)pentanedioic acid
ppm:	Parts per million
PSMA:	Prostate specific membrane antigen
PTS:	Parallel tagging strategy
PVDF:	Polyvinylidenedifluoride

R

RCP:	Radiochemical purity
RCY:	Radiochemical yield
RES:	Reticuloendothelial system
R_t:	Retention time
S	
SAAC:	Single amino acid chelate
SDS-PAGE:	Sodium Dodecyl Sulfate Polyacrylamide Gel Electrophoresis
sec:	Second(s)
SFB:	N-succinimidyl-4-[^{18}F]fluorobenzoate
SPECT:	Single Photon Emission Computed Tomography
T	
TAAG:	Triazole appending agent
TAMRA:	5 – Carboxytetramethylrhodamine
TBME:	Tertiary butyl methyl ether
tBu:	Tertiary butyl
TCO:	Trans-cyclooctene
TEA:	Triethylamine
TIPS:	Triisopropylsilane
TFA:	Trifluoroacetic acid
TFP:	Tetrafluorophenyl
THF:	Tetrahydrofuran
TLC:	Thin layer chromatography
Tz:	Tetrazine
$t_{½}$:	Half-life
2D:	Two-dimensional

U

uPAR:	Urokinase plasminogen activator receptor
US:	Ultrasound
UV light:	Ultraviolet light

V

VCAM-1:	Vascular cell adhesion molecule-1
VEGFR2:	Vascular endothelial growth factor receptor 2

1 Chapter 1: Introduction

1.1 Molecular imaging

Molecular imaging (MI) is a rapidly growing field that involves noninvasively visualizing biochemical changes associated with diseases like cancer and diabetes in living systems.[1] MI can be used to improve early diagnosis of diseases, expedite the evaluation of new treatments and act as a tool for studying cancer biology *in vivo* in both animal models and human subjects.[1] Contrast and signaling agents that enable MI by emitting or perturbing signals that are detected by the appropriate imaging device are highly varied. They include those derived from small molecules, biomolecules, polymers and nano- or micron-sized biomaterials.[1]

Several MI modalities exist where each has unique signaling mechanism and contrast agents. Table 1.1 is a summary of common techniques, which include magnetic resonance imaging (MRI), single photon emission computed tomography (SPECT), positron emission tomography (PET), ultrasound (US) and optical/fluorescent imaging. Each modality has unique advantages and disadvantages which has resulted in efforts to combine imaging modalities in the hopes of taking advantage of their strengths and overcoming their limitations.[2]

Table 1.1 Summary of the different modalities used in MI and their respective advantages and disadvantages.[3]

Imaging modality	Advantages	Disadvantages	Signaling or contrast agent
US	High spatial resolution High temporal resolution Real-time imaging Low cost	Operator dependency Targeted imaging limited to vascular compartment Limited depth penetration	Microbubbles
MRI	High spatial resolution High depth penetration High soft tissue contrast	Cost Imaging time Low sensitivity	Paramagnetic agents
SPECT/PET	High sensitivity High depth penetration Broad range of probes available	Cost Limited spatial resolution No anatomical definition	Radioisotopes
Optical imaging	High sensitivity Broad range of probes	Limited clinical translation Limited depth penetration	Fluorescent dyes

1.2 Ultrasound Imaging

Because of its relative low cost, availability and portability, US imaging is the second most widely used imaging technique in medicine.[4] It allows for real-time imaging without exposing patients to radiation. In US imaging, US pulses are transmitted from a transducer that is placed on the skin. The pulses of US waves travel through the different structures in the body where it gets partially

reflected or scattered. The US transducer subsequently detects a portion of the scattered sound waves and converts them into electrical pulses. 2D US images are then generated from the digitized electrical pulses.[2] US imaging has been widely used as a preliminary screening tool and for quick follow-up examinations from multiple disciplines including cardiology, oncology and gynecology.[5]

Applications of US imaging have traditionally focused on generating anatomical information. This has spurred on the development of echogenic contrast agents, which include gas-filled microbubbles (MBs), to amplify the US signal associated with a physical or biochemical process (e.g. blood flow, receptor expression). MBs have several orders of magnitude higher US reflective properties than blood, which improves the performance and sensitivity of US imaging.[5,6] For example, MBs in conjunction with US made it feasible to use US to generate images associated with functional and molecular vascular characteristics including detecting and characterizing focal liver lesions,[7] contrast echocardiography[8] and evaluating cerebral circulation for stroke[9] and brain death diagnosis.[10]

1.3 Microbubbles

MBs are contrast agents used for US imaging that amplify the US signal by interacting with the US waves. Once exposed to US, MBs start to oscillate reflecting the US waves and producing harmonic signals. Using contrast-imaging technologies (e.g. amplitude modulation or pulse inversion) the harmonic signals

produced by surrounding tissue can be greatly reduced compared to that from MBs. This drastically decreases the background noise and makes it feasible to quantify the signal coming from just the MBs (Figure 1.1 and 1.2).[11,12]

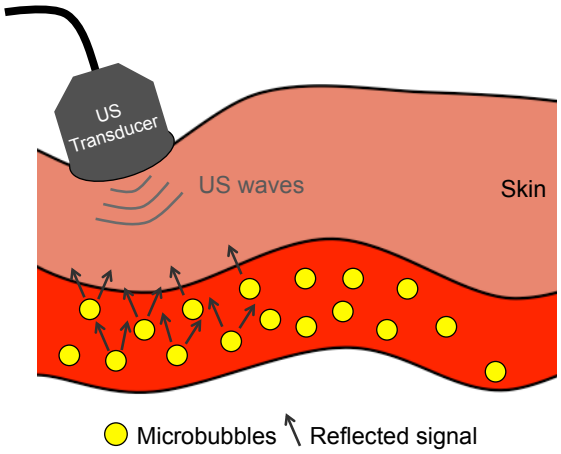

Figure 1.1 Schematic illustrating MBs reflecting US waves produced from a transducer *in vivo*.

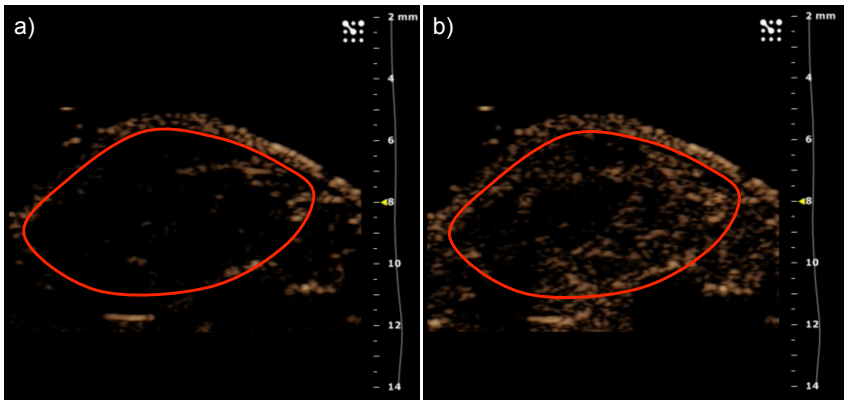

Figure 1.2 Nonlinear contrast mode US image of a subcutaneous A431 human epidermoid carcinoma tumour in a mouse before administering MBs (a) and after MBs injection via the tail vein (b). Higher US signal enhancement is observed within the tumour after administering the MBs. Tumour margins are highlighted

with the red line.*

MBs are typically composed of gas particles less than 10 μm in diameter surrounded by a highly condensed monolayer. The first generation of MBs did not have a stabilizing shell resulting in their larger size and short circulation time (seconds). Second generation agents consist of air filled bubbles stabilized by a shell that is lipid, protein or polymer based. These bubbles have a better size distribution but have limited circulation time (less than 5 min). This was improved in the third generation of MBs where the gas core was replaced with an inert gas, mainly perfluorocarbons, which increased their stability and circulation time (up to 15 min)[13] (Table 1.2).

* Zlitni, A. Valliant, J.F. Unpublished results.

Table 1.2 Summary of the different generations of MBs used in the clinic, their composition and manufacturer.[13-15]

Generation	Microbubble	Company	Gas core	Shell
First	Echovist®	Schering AG	Air	None
Second	Levovist®	Schering AG	Air	Galactose and PA
	Albunex®	Molecular Biosystems Inc.	Air	HSA
Third	Optison®**	GE Healthcare	C_3F_8	HSA
	SonoVue**	Bracco Diagnostic Inc.	SF_6	DSPC/DPPG/PA
	Definity®**	Bristol-Myers Squibb Medical Imaging	C_3F_8	DPPC/DPPA/MPEG 5000-DPPE
	Imagent®**	Alliance Pharm. Corp.	C_6F_{14}/Nitrogen	DMPC
	Sonazoid®**	GE Healthcare	C_4F_{10}	Hydrogenated egg phosphatidylserine

**FDA approved for clinical use. PA: palmitic acid; HSA: human serum albumin; DSPC: Distearoyl phosphatidylcholine; DPPG: Dipalmitoyl phosphatidylglycerol; DPPC: Dipalmitoyl phosphatidylcholine; DPPA: Dipalmitoyl phosphoric acid; DMPC: Dimyristoyl phosphatidylcholine; MPEG5000-DPPE: Polyethyleneglycol 5000-Dipalmitoyl phosphatidylethanolamine.

1.4 Molecular US imaging

New generation of MBs that are targeted to markers expressed on the surface of endothelial cells of diseases such as angiogenesis and inflammation further expanded the utility of US to include molecular imaging applications.[4] In order to differentiate between the signal obtained from bound MBs compared to

that from circulating MBs, sequences such as the destruction replenishment sequence should be used.[3] MBs are targeted to the site of disease by linking a biomolecule to the surface, which is designed to bind a specific biomarker at the site of the disease or injury (Figure 1.3). Due to their size, MBs are restricted to the vascular space; making them only capable to target markers expressed on the surface of the vascular endothelium.[16] This limitation notwithstanding, US imaging can detect MBs in high specificity and sensitivity, producing images that provide useful information on the expression levels of key biomarkers.[6] Furthermore, targeted MBs have shown potential to be used as vehicles for delivering therapeutics to the site of the disease.[13] Consequently, the combination of targeted drug loaded MBs and US imaging represents a combination therapeutic and diagnostic tool ("theranostic").

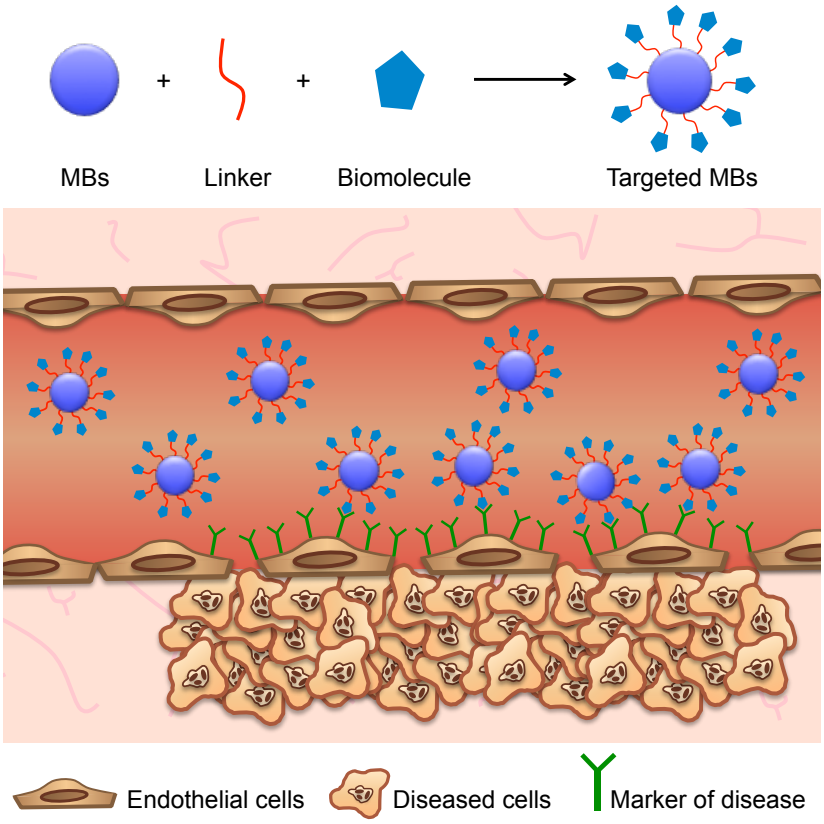

Figure 1.3 Schematic representation of the components of targeted MBs and their binding to biomarkers expressed on the endothelium.

1.4.1 Methods of preparing targeted MBs

Several strategies have been developed to target MBs.[14,16] One approach involves adding a targeting ligand to the shell component(s) before formulating the MBs. This approach maximizes product yield and ensures purity because every step in the process is performed separately. However, it is mostly suited for small organic targeting ligands (e.g. peptides, carbohydrates, vitamins and hormones).

A second strategy involves formulating the MBs followed by attaching a

targeting ligand to the surface. This approach is best suited for ligands that would be sensitive to the conditions needed to prepare MBs (e.g. sonication, high-speed mixing, elevated temperatures). The ligand can be attached to the surface of the MBs through covalent or non-covalent binding. The latter typically relies on the well-characterized biotin-streptavidin interaction which has a dissociation constant (K_d) of ~10^{-15} M.[17,18] In this approach, biotin is first attached to the lipids of the MB's shell. Excess streptavidin is then added to the MBs mixture and binds to the biotin on the shell. After incubation, any non-bound streptavidin can be removed by low-speed centrifugation. The biotinylated ligand of interest is then added and binds to streptavidin on the surface of the MBs. The popularity of this approach is due to its ease and general applicability since biotin can be readily anchored to various ligands and streptavidin-coated MBs are commercially available. Unfortunately, it is not used in clinical settings due to the potential immunogenic response upon administration of a foreign protein (streptavidin).[16,19] The need for multiple centrifugation steps under sterile conditions can also be technically challenging in the clinic.[14] It is however an ideal method for developing preclinical probes where the use of US is increasing as a result of the development of high resolution scanners for small animal imaging.

To covalently link targeting ligands to preformed MBs it is possible to use a lipid derivative containing a terminal carboxylic acid within the MBs shell to

link to a free amino group of a ligand of interest. This can be achieved through carbodiimide chemistry[20] or by activating the free carboxyl group to an N-hydroxysulfosuccinimide (active) ester.[21] The main drawback of these two approaches is low surface functionalization yield and variability in overall yield.[21]

An alternate covalent approach relies on the preparation of MBs coated with maleimides. This way, targeting ligands having free thiol groups can be readily conjugated by forming a stable thioether bond.[22] This method has shown promise since the number of side reactions is very low and oxidation of the thiol groups is negligible especially under a perfluorocarbon atmosphere.[16]

1.4.2 Criteria for molecular US imaging agents

There are several requirements that must be satisfied to create effective targeted molecular US imaging agents. The target of interest should be extracellular and expressed in high numbers compared to normal tissue. In addition, to use US to monitor the effect of treatment, the expression levels of the target must be significantly altered after therapy. A third key criterion is that in order for the contrast agent to overcome the effect of shear forces found in capillaries, it is essential that the targeting molecule when conjugated bind rapidly and strongly to the target with high specificity. Finally, because MBs do not extravasate, they can only target markers expressed on endothelial cells limiting the number of possible targets.[23,24]

1.4.3 Intravascular markers for targeted molecular US imaging

The effectiveness of targeted molecular US imaging in detecting and monitoring different types of diseases such as inflammation and cancer has been reported. In inflammation, various diseases which include inflammatory bowl disease, myocardial ischemia, atherosclerosis and in cardiac transplant rejection were monitored by detecting key biomarkers such as P and E selectin,[25-27] mucosal addressin cellular adhesion molecule-1 (Mad-CAM-1),[28] vascular cell adhesion molecule-1 (VCAM-1)[29] and intercellular adhesion molecule-1 (ICAM-1).[30] In oncology, expression levels of several markers of angiogenesis such as vascular endothelial growth factor receptor 2 (VEGFR2), integrin (i.e. $\alpha_V\beta_3$) and endoglin (CD105) have been explored. The detection of these markers using US targeted MBs was evaluated using multiple cancer types such as ovarian,[31-33] prostate,[34,35] breast,[36] liver,[37] colon[38] and pancreatic cancer.[39,40] Another target that was explored using targeted US imaging was prostate specific membrane antigen (PSMA), which is a glycoprotein expressed on the surface of prostate carcinomas.[41,42]

1.4.4 Translation of targeted molecular US imaging agents to the clinic

To date, most of the preclinical assessments done on targeted MBs were prepared by taking advantage of the streptavidin-biotin interaction. Although this approach is amenable to develop MBs targeted to different sites, such strategy cannot be used in the clinic as mentioned in section 1.4.1. Another more clinically

translatable strategy was focused on directly attaching the MB's shell to the targeting moiety.[16] The problem with this strategy is that it requires long development pathways that demand major modifications on both the shell of the MBs and the targeting moiety. This makes targeted MBs production inconsistent and hard to translate to new targets.

There is one targeted MB (BR55) currently in clinical trials. BR55 consists of a heterodimeric peptide that binds to mouse and human VEGFR2 that is covalently linked to a phospholipid MBs shell.[43] Preclinical assessment of this agent showed high retention of these MBs in tumour vasculature of prostate cancer[34] and two different breast cancer xenografts.[44] Furthermore, accompanying BR55 with US imaging provided the ability to monitor antiangiogenic therapy in a human colon cancer mouse xenograft with high sensitivity.[45] In 2013, BR55 completed preliminary phase 0 clinical trials in Europe for the detection of prostate cancer,[46] ovarian and breast cancer.[47] Currently BR55 is being tested in phase 1 and 2 trials at Stanford University for the assessment of prostate cancer.[48]

BR55 is specific to VEGFR2 therefore to create US MBs against other targets would require re-starting an entirely new development effort that is time consuming and expensive. There is consequently, a need to provide a more versatile and efficient synthetic strategy built from a common platform to prepare human compatible targeted MBs. Ideally the new methodology would be able to

produce one type of MBs that can be adapted with minimal modification for binding to different targets.

1.5 Thesis Overview

The first objective was to develop a platform to prepare and evaluate targeted multi-modal MBs (Chapter 2). The initial effort focused on creating agents that could be used with US, SPECT and optical imaging. Multi-modal imaging can help overcome the limitations of the individual imaging modality and help expedite the evaluation of MBs *in vivo*, notably their overall distribution and ability to bind the target of interest. These efforts, which ran into challenges, resulted in a new objective, which was to use bioorthogonal chemistry to create a new platform technology to functionalize and target MBs. The development of this strategy and demonstration of its ability to target MBs to VEGFR2 is described in Chapter 3. Further exploitation and optimization of the chemistry for creating MBs capable of binding oncology markers PSMA and uPAR are described in Chapters 4 and 5.

For the proof of concept work, the research focused on using biotin and streptavidin as a means to derivatize MBs. This pathway was chosen to be able to provide an expedient approach to test new functionalization strategies using commercially available streptavidin-coated MBs (MicroMarker™ Target-Ready Contrast Agent Kit, VisualSonics Inc., Toronto, Canada). In addition, streptavidin-coated MBs have been used to create other classes of targeted

MBs,[49] providing the opportunity to compare new protocols to US data using MBs prepared by traditional bioconjugation strategies. Initial attempts to adapt the new chemistry to create human-compatible US contrast agents is also presented (Chapter 6).

1.6 References

[1] M. A. Pysz, S. S. Gambhir, J. K. Willmann, *Clin. Radiol.* **2010**, *65*, 500–516.

[2] M. L. James, S. S. Gambhir, *Physiol. Rev.* **2012**, *92*, 897–965.

[3] N. Deshpande, A. Needles, J. K. Willmann, *Clin. Radiol.* **2010**, *65*, 567–581.

[4] L. Abou-Elkacem, S. V. Bachawal, J. K. Willmann, *Eur. J. Radiol.* **2015**, *84*, 1685–1693.

[5] F. Kiessling, S. Fokong, J. Bzyl, W. Lederle, M. Palmowski, T. Lammers, *Adv. Drug Deliv. Rev.* **2014**, *72*, 15–27.

[6] A. L. Klibanov, P. T. Rasche, M. S. Hughes, J. K. Wojdyla, K. P. Galen, J. H. J. Wible, G. H. Brandenburger, *Invest. Radiol.* **2004**, *39*, 187.

[7] D. Strobel, K. Seitz, W. Blank, A. Schuler, C. Dietrich, A. von Herbay, M. Friedrich-Rust, G. Kunze, D. Becker, U. Will, et al., *Ultraschall Med.* **2008**, *29*, 499–505.

[8] S. L. Mulvagh, H. Rakowski, M. A. Vannan, S. S. Abdelmoneim, H. Becher, S. M. Bierig, P. N. Burns, R. Castello, P. D. Coon, M. E. Hagen, et al., *J. Am. Soc. Echocardiogr.* **2008**, *21*, 1179–1201.

[9] J. Allendoerfer, C. Tanislav, *Ultraschall Med.* **2008**, *29,* S210–S214.

[10] S. Welschehold, F. Geisel, C. Beyer, A. Reuland, T. Kerz, *J. Neurol. Neurosurg. Psychiatr.* **2013**, *84*, 939–940.

[11] K. Ferrara, R. Pollard, M. Borden, *Annu. Rev. Biomed. Eng.* **2007**, *9*, 415–447.

[12] F. Forsberg, W. T. Shi, B. B. Goldberg, *Ultrasonics* **2000**, *38*, 93–98.

[13] S. Tinkov, R. Bekeredjian, G. Winter, C. Coester, *J. Pharm. Sci.* **2009**, *98*,1935–1961.

[14] A. L. Klibanov, *Bioconjugate Chem.* **2005**, *16*, 9–17.

[15] J. R. Lindner, *Nat. Rev. Drug Discov.* **2004**, *3*, 527–532.

[16] A. L. Klibanov, *Med. Biol. Eng. Comput.* **2009**, *47*, 875–882.

[17] F.-T. Liu, N. J. Leonard, *J. Am. Chem. Soc.* **1979**, *101*, 996–1005.

[18] N. M. Green, *Biochemical Journal* **1963**, *89*, 599.

[19] P. György, C. S. Rose, R. E. Eakin, E. E. Snell, R. J. Williams, *Science* **1941**, *93*, 477–478.

[20] F. S. Villanueva, R. J. Jankowski, S. Klibanov, M. L. Pina, S. M. Alber, S. C. Watkins, G. H. Brandenburger, W. R. Wagner, *Circulation* **1998**, *98*,

1–5.

[21] A. A. Bogdanov, A. L. Klibanov, V. P. Torchilin, *FEBS Letters* **1988**, *231*, 381–384.

[22] A. Della Martina, E. Allémann, T. Bettinger, P. Bussat, A. Lassus, S. Pochon, M. Schneider, *Eur. J. Pharm. Biopharm.* **2008**, *68*, 555–564.

[23] S. A. Moestue, I. S. Gribbestad, R. Hansen, *Int. J. Mol. Sci.* **2012**, *13*, 6679–6697.

[24] F. Kiessling, S. Fokong, J. Bzyl, W. Lederle, M. Palmowski, T. Lammers, *Adv. Drug Deliv. Rev.* **2013**, *72*, 15–27.

[25] N. Deshpande, A. M. Lutz, Y. Ren, K. Foygel, L. Tian, M. Schneider, R. Pai, P. J. Pasricha, J. K. Willmann, *Radiology* **2012**, *262*, 172–180.

[26] H. Wang, S. Machtaler, T. Bettinger, A. M. Lutz, R. Luong, P. Bussat, S. S. Gambhir, F. Tranquart, L. Tian, J. K. Willmann, *Radiology* **2013**, *267*, 818–829.

[27] X. Leng, J. Wang, A. Carson, X. Chen, H. Fu, S. Ottoboni, W. R. Wagner, F. S. Villanueva, *Mol. Imaging* **2014**, *16*, 1–9.

[28] C. Bachmann, A. L. Klibanov, T. S. Olson, J. R. Sonnenschein, J. Rivera-Nieves, F. Cominelli, K. F. Ley, J. R. Lindner, T. T. Pizarro,

Gastroenterology **2006**, *130*, 8–16.

[29] E. Khanicheh, Y. Qi, A. Xie, M. Mitterhuber, L. Xu, M. Mochizuki, Y. Daali, V. Jaquet, K.-H. Krause, Z. M. Ruggeri, et al., *Arterioscler. Thromb. Vasc. Biol.* **2013**, *33*, 2187–2192.

[30] G. E. R. Weller, E. Lu, M. M. Csikari, A. L. Klibanov, D. Fischer, W. R. Wagner, F. S. Villanueva, *Circulation* **2003**, *108*, 218–224.

[31] M. R. Patel, P. Chu, J. Rosenberg, S. S. Gambhir, *Radiology* **2008**, *248*, 936–944.

[32] N. Deshpande, Y. Ren, K. Foygel, J. Rosenberg, J. K. Willmann, *Radiology* **2011**, *258*, 804–811.

[33] A. Barua, A. Yellapa, J. M. Bahr, S. A. Machado, P. Bitterman, S. Basu, S. Sharma, J. S. Abramowicz, *Int. J. Gynecol. Cancer* **2014**, *24*, 19–28.

[34] I. Tardy, S. Pochon, M. Theraulaz, P. Emmel, L. Passantino, F. Tranquart, M. Schneider, *Invest. Radiol.* **2010**, *45*, 573–578.

[35] P. J. A. Frinking, I. Tardy, M. Theraulaz, M. Arditi, J. Powers, S. Pochon, F. Tranquart, *Ultrasound Med. Biol.* **2012**, *38*, 1460–1469.

[36] S. V. Bachawal, K. C. Jensen, A. M. Lutz, S. S. Gambhir, F. Tranquart, L. Tian, J. K. Willmann, *Clin. Cancer Res.* **2013**, *73*, 1689–1698.

[37] K. Sugimoto, F. Moriyasu, Y. Negishi, N. Hamano, H. Oshiro, N. G. Rognin, T. Yoshida, N. Kamiyama, Y. Aramaki, Y. Imai, *JUM* **2012**, *31*, 1909–1916.

[38] H. Wang, O. F. Kaneko, L. Tian, D. Hristov, J. K. Willmann, *Invest. Radiol.* **2015**, *50*, 322–329.

[39] M. A. Pysz, S. B. Machtaler, E. S. Seeley, J. J. Lee, T. A. Brentnall, J. Rosenberg, F. Tranquart, J. K. Willmann, *Radiology* **2015**, *274*, 790–799.

[40] G. Korpanty, J. G. Carbon, P. A. Grayburn, J. B. Fleming, R. A. Brekken, *Clin. Cancer Res.* **2007**, *13*, 323–330.

[41] L. Wang, L. Li, Y. Guo, H. Tong, X. Fan, J. Ding, H. Huang, *Prostate* **2013**, *73*, 1147–1158.

[42] X. Fan, L. Wang, Y. Guo, Z. Tu, L. Li, H. Tong, Y. Xu, R. Li, K. Fang, *PLoS ONE* **2015**, *10*, e0127419.

[43] S. Pochon, I. Tardy, P. Bussat, T. Bettinger, J. Brochot, M. von Wronski, L. Passantino, M. Schneider, *Invest. Radiol.* **2010**, *45*, 89–95.

[44] J. Bzyl, W. Lederle, A. Rix, C. Grouls, I. Tardy, S. Pochon, M. Siepmann, T. Penzkofer, M. Schneider, F. Kiessling, et al., *Eur. Radiol.* **2011**, *21*, 1988–1995.

[45] M. A. Pysz, K. Foygel, J. Rosenberg, S. S. Gambhir, M. Schneider, J. K.

Willmann, *Radiology* **2010**, *256*, 519–527.

[46] Bracco Diagnostics, Inc, "BR55 in Prostate Cancer: an Exploratory Clinical Trial," can be found under:

https://clinicaltrials.gov/ct2/show/NCT01253213

[47] Bracco Diagnostics, Inc, "A Study of BR55 in Contrast Enhanced Ultrasound Imaging in Patients with Ovarian and Breast Cancer," can be found under:

https://www.clinicaltrialsregister.eu/ctr-search/search?query=2012-000699-40

[48] Bracco Diagnostics, Inc, "A Pilot Trial Using BR55 Ultrasound Contrast Agent in the Assessment of Prostate Cancer" can be found under:

https://clinicaltrials.gov/ct2/show/NCT02142608 and

http://med.stanford.edu/clinicaltrials/trials/NCT02142608

[49] F. Kiessling, S. Fokong, P. Koczera, W. Lederle, T. Lammers, *J. Nucl. Med.* **2012**, *53*, 345–348.

2 Chapter 2: The Development and Evaluation of Multi-Modal MBs for SPECT, Optical and US Imaging

2.1 Introduction

There is increased interest in combining MI modalities in order to take advantage of their strengths and overcome the limitation of each individual technology. A common example of multi-modal imaging is the combination of positron emission tomography and computed tomography (PET-CT), where the nuclear component (PET) gives functional information while CT provides anatomical referencing.[1] With the arrival of new hybrid imaging methods, there has been concomitant interest in developing hybrid imaging probes; one agent that can generate different types of contrast signals.

Different multi-modal US imaging probes have been developed and used for US-MRI,[2,3] US-optical[4,5] or US-nuclear imaging.[6,7] To our knowledge, a tri-modal SPECT-US-optical agent has not been reported. Tagging the MBs with a radioisotope creates the opportunity to assess their distribution and ultimate fate *in vivo* (through SPECT or PET whole-body imaging and *ex vivo* tissue counting). Having a fluorescent dye ligated to the MBs would provide a way of studying binding to specific cellular markers using optical methods.

In this chapter, the preparation, purification and evaluation of MBs labeled with ^{99m}Tc are reported. Specifically, a series of known and novel biotinylated

derivatives of bifunctional radiometal chelates, fluorophores and biomolecules were synthesized and linked to the surface of streptavidin-coated MBs. Subsequently, the optimal radiolabeling conditions were developed along with new ways to ligate MBs to targeting vectors. The *in vitro* and *in vivo* evaluation of the targeted and non-targeted multi-modal MBs was also performed.

2.1.1 Single photon emission computed tomography (SPECT)

Single photon emission computed tomography is an imaging technique that employs gamma (γ) emitting radionuclides (Table 2.1). It is composed of a camera that detects γ-rays emitted from the radionuclides at multiple angles over a 360° rotation along the long access of the subject. The collected 2D images are combined to produce a 3D projection.[1]

Table 2.1 Examples of γ-emitting isotopes used in SPECT imaging

Radioisotope	Radiation emitted (Energy keV)	Half-life
^{99m}**Tc**	γ-ray (142)	6 hours
^{111}**In**	γ-ray (171 (88%), 247 (94%))	2.83 days
^{67}**Ga**	γ-ray (93 (10%), 185 (24%), 296 (22%))	78.3 hours
^{123}**I**	γ-ray (159)	13.2 hours

2.1.2 Technetium-99m (^{99m}Tc) and tridentate chelates

^{99m}Tc is the most widely used radionuclide for SPECT imaging. It is available at a low cost, has a half-life of 6 hr and γ-ray energy of 140 keV. Its

radioactive decay imparts lower doses for patients compared to most other radionuclides.[8] ^{99m}Tc as $^{99m}TcO_4^-$ can be readily obtained from a ^{99}Mo generator in which ^{99}Mo is absorbed onto an alumina column as MoO_4^-. It then decays to pertechnetate ($^{99m}TcO_4^-$) and is eluted with a dilute saline solution on a daily basis.[9,10]

Directly labeling targeting vectors with ^{99m}Tc is not an effective way to make molecular imaging probes. This is because the stability of the product is not typically sufficient to stay intact *in vivo* and multiple products are often formed during labeling. This issue is addressed by using a bifunctional chelator (BFC). A BFC possesses donor groups for binding the metal and another functionality for linking to targeting vectors. One of the most widely investigated oxidation states of Tc is Tc(I) because it forms inert complexes with tridentate chelates. $[^{99m}Tc(CO)_3(H_2O)_3]^+$ can be prepared from $^{99m}TcO_4^-$ using an instant kit in minutes.[8] For the $^{99m}Tc(CO)_3^+$ core, tridentate chelators with heterocyclic donors form stable complexes in high yield.[10] One successful example of a Tc(I) BFC is the single amino acid chelate (SAAC) system, which was prepared from lysine so that it could be incorporated into peptide and other classes of targeting vectors (Figure 2.1).[11]

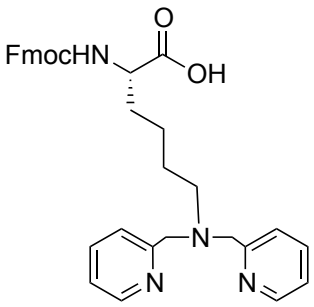

Figure 2.1 Structure of the first Single Amino Acid Chelate (SAAC)

2.1.3 Objectives

Our group reported a method to label US MBs with ^{99m}Tc and purify the product using a magnet capture strategy in order to quantitatively study MBs distribution through *in vivo* imaging or *ex vivo* tissue counting.[12] The initial goal was to repeat the synthesis and then develop a more versatile and robust platform for linking the ^{99m}Tc-SAAC system, optical dyes and targeting vectors to US contrast agents.

Subsequently, a solid-phase synthesis method was created to prepare a biotinylated bifunctional chelate that can be linked to an optical dye and/or targeting vectors for conjugation to MBs. Once prepared, a detailed analysis of the loading capacity on these MBs was conducted in order to determine which of two possible tagging strategies was most feasible: 1) Tagging bubbles with a biotinylated targeting vector and a chelate derivative (parallel tagging strategy), or 2) Tagging with a single biotinylated compound containing both the targeting vector and signaling agent (integrated tagging strategy, Figure 2.2).

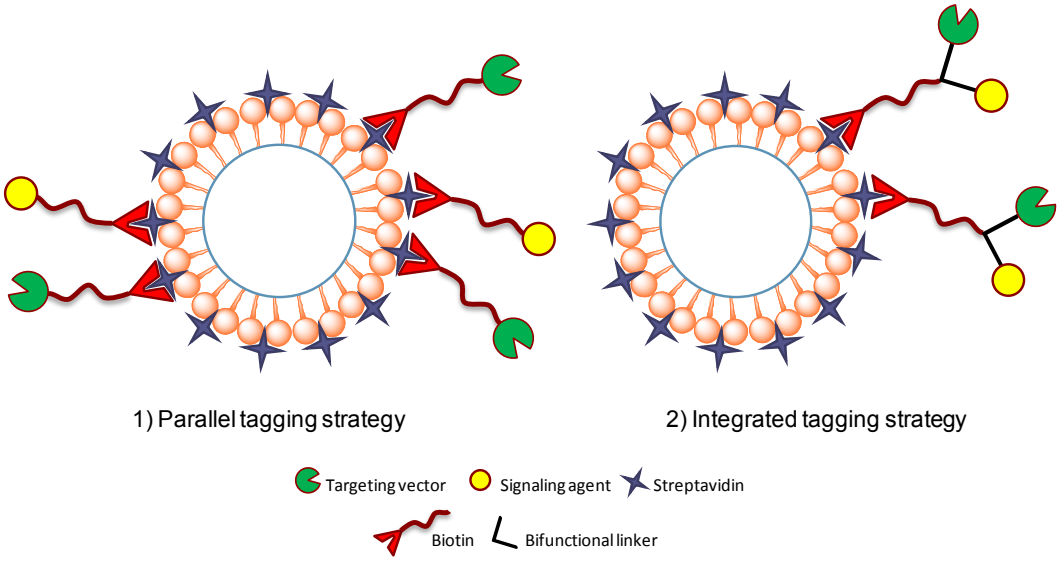

Figure 2.2 Schematic showing the two strategies used to prepare targeted and radio- or fluorescently labeled MBs.

2.2 Preparation and evaluation of non-targeted multi-modal MBs

2.2.1 Strategy

The initial goal was to repeat the synthesis of the biotinylated bis-pyridyl derivative **8** and the magnetic purification strategy to isolate labeled MBs.[12] In parallel, an alternative synthetic route to prepare the same ligand was investigated in hopes to improve the yield of the final product that previously was low. Unfortunately, original routes to synthesize compound **8** (Scheme 2.1 and 2.2) were low yielding. It also did not allow for simple methods to incorporate other chelates, targeting vectors or different contrast agents. To address these issues, a new method using solid-phase synthesis was explored whereby a resin-bound biotin group was linked to the SAAC chelate and other ligands through a

hydrophilic spacer. The approach, which is described in detail below (Scheme 2.4), resulted in the synthesis of a biotinylated derivative linked, through a PEG spacer, to a rhodamine dye and SAAC ligand. This new synthetic route was high yielding and provided a platform to prepare multi-modal biotinylated derivatives.

2.2.2 Synthesis of Biotinylamido-propyl(dipicolyl)amine (L1) (8)

Compound **8** (Scheme 2.1) was prepared by modifying the procedure reported by our group.[13] Dipicolylpropylphtalimide **3** was prepared through a nucleophilic substitution reaction between bromo-propyl phthalimide **1** and dipicolyl amine **2** using sodium carbonate as a base. The reaction was monitored with TLC and electrospray ionization mass spectrometry (ESI-MS) until no further starting material was observed. The desired product was isolated by column chromatography in 50% yield. The phtalimide group in **3** was then removed using hydrazine monohydrate and any side products were extracted with chloroform during the work up. The pH of the aqueous layer, which contained compound **4**, was then adjusted by adding sodium hydroxide and **4** was extracted with chloroform and purified through column chromatography. Biotin-TFP-ester **7** was prepared in 95% yield following the literature method[14] and then treated with **4** in DMF using triethylamine as a base. Following evaporation of the solvent, the produced solid was dissolved in DCM, and resulting ether induced precipitate was collected by filtration and dried under vacuum. Compound **8** was purified by column chromatography and isolated in 63% yield. ^{1}H NMR and ESI-

MS agreed with literature values.

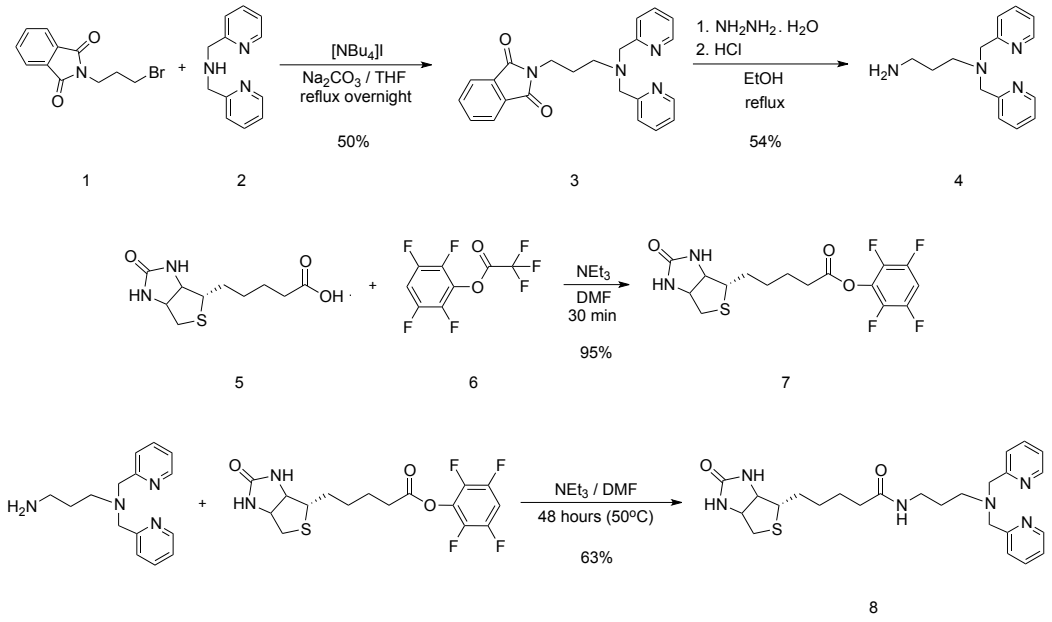

Scheme 2.1 Synthesis of L1 **8**

2.2.3 Synthesis of Re-L1 (16)

Compound **16** was prepared by treating 1,3-diaminopropane **9** with one equivalent of tert-butylphenylcarbonate **10** (Scheme 2.2).[15] The bispyridyl chelate **13** was then obtained through a reductive amination reaction in which the monoprotected diamine **11** was treated with 2-pyridine-carboxaldehyde **12** in the presence of a reducing agent ($NaBH(OAc)_3$). After 16 hr and an aqueous work up to remove any excess of starting material, compound **13** was isolated in 67% yield by extraction with DCM and column chromatography. Compound **14** was then prepared in quantitative yield by heating a solution of **13** and $[Re(CO)_3(H_2O)_3]Br$ to reflux for 4 hr and monitoring the reaction by ESI-MS. The Boc protecting

group in **14** was removed by mixing in a 1:1 TFA:DCM mixture for 4 hr at room temperature. Compound **15** was finally reacted with biotin-TFP-ester **7** using TEA as a base and the final product **16** was obtained in 53% yield after purification.

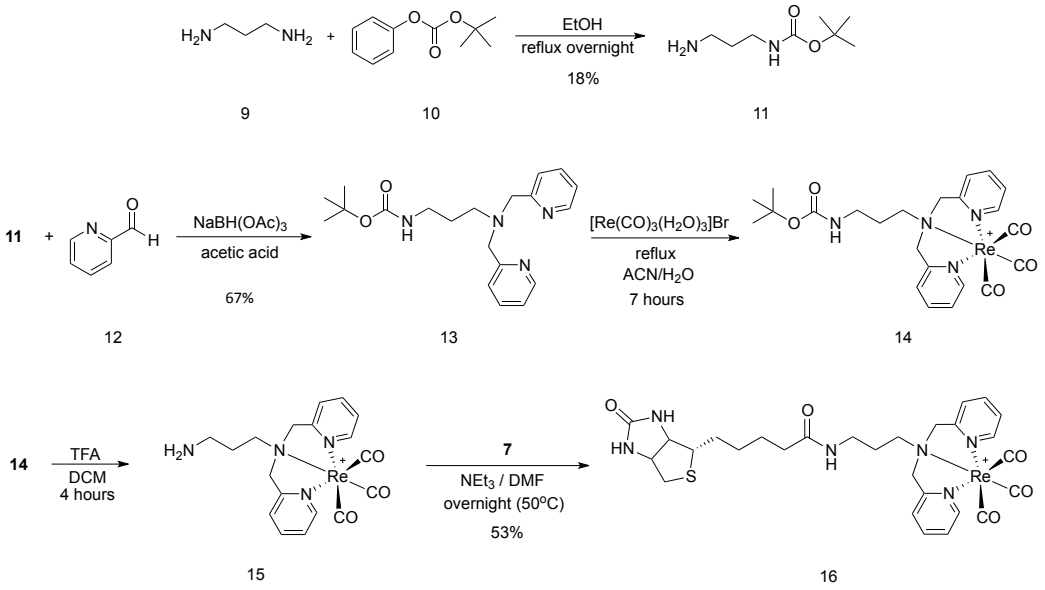

Scheme 2.2 Synthesis of Re-L1 **16**

2.2.4 Synthesis of ^{99m}Tc-L1 (17)

Synthesis of ^{99m}Tc-L1 **17** was prepared by modifying the procedure reported by our group (Scheme 2.3).[16] Compound **8** was dissolved in EtOH and added to a microwave vial containing a solution of $[^{99m}Tc(CO)_3(H_2O)_3]^+$ in saline. The reaction mixture was heated to 110 °C for 5 min, then purified by semi-preparative HPLC and collected. The radiochemical yield obtained was 95% compared to > 99% that was obtained in the literature, which may have been due to loss during HPLC purification.[12] To confirm the identity of **17**, a co-injection

with Re-L1 **14** into the HPLC was conducted showing the two compounds eluted at the same time (Figure 2.3).

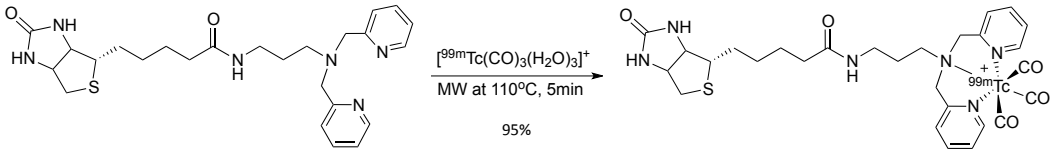

Scheme 2.3 Synthesis of ^{99m}Tc-L1 **17**

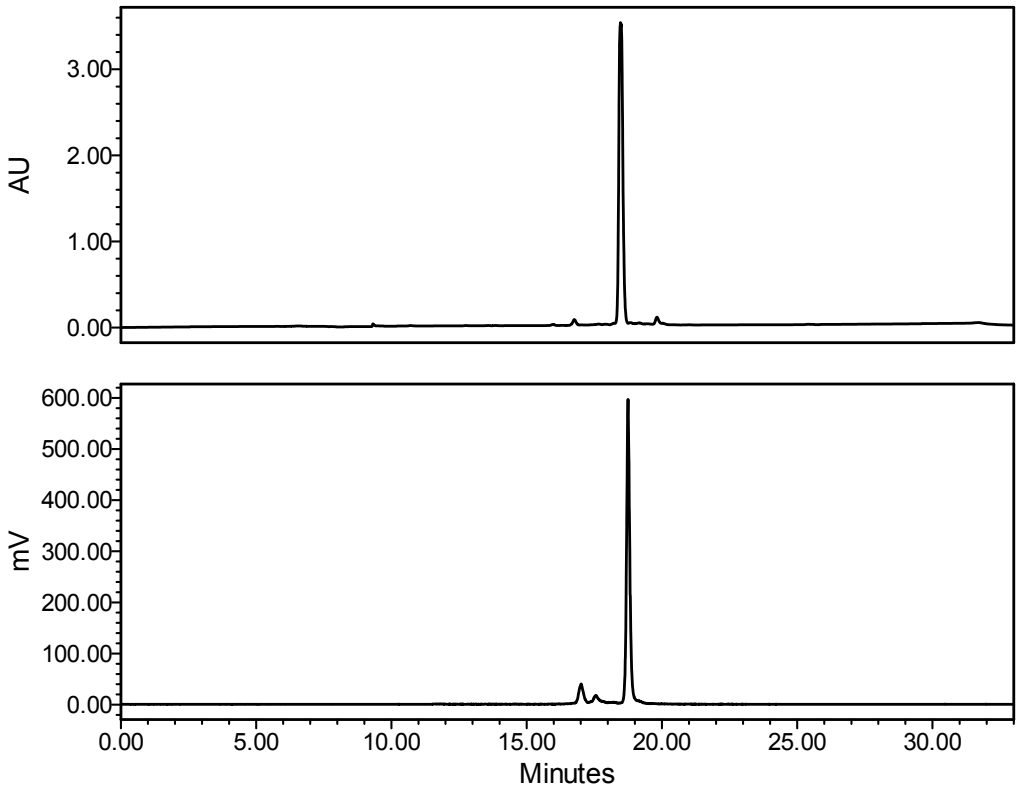

Figure 2.3 Top: HPLC-UV chromatogram of the co-injected Re-L1 and **bottom:** HPLC-γ chromatogram of purified ^{99m}Tc-L1.

2.2.5 Labeling MBs with ^{99m}Tc-L1

Streptavidin coated MBs containing a perfluorocarbon gas core were reconstituted following the manufacturer's instructions. Compound **17** was introduced to the MBs dropwise and the vial allowed to sit at room temperature with periodic agitation for 45 min. Excess **17** was removed by adding streptavidin coated magnetic beads for 20 min and separation was done by placing the vial beside a magnet. For quality control, a sample before and after the magnetic bead purification was diluted in 100 μL of saline, sonicated until the solution became clear and analyzed through a HiTrap size exclusion cartridge connected to an HPLC where the radiochemical yield was 38% (Figure 2.4).

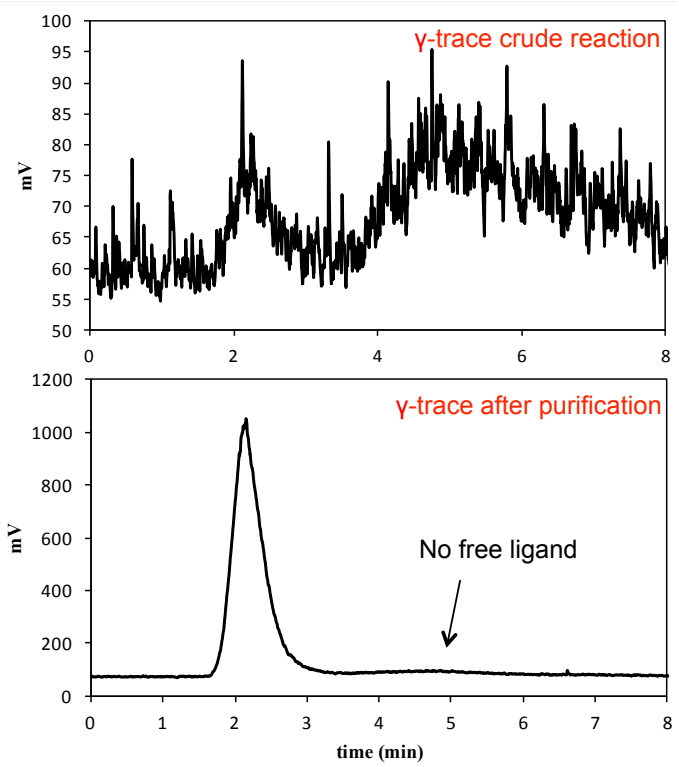

Figure 2.4 Analysis of MBs with a HiTrap size-exclusion cartridge attached to an HPLC. **Top:** HPLC-γ chromatogram of crude reaction mixture containing ^{99m}Tc-L1-MBs and free ^{99m}Tc-L1. **Bottom:** HPLC-γ chromatogram of ^{99m}Tc-L1-MBs after magnetic bead purification. Due to injecting a small amount of the crude mixture, the top γ-trace shows significant background noise.

2.2.6 Synthesis of SAACBiotinTAMRA (19) (D1) and ReSAACBiotinTAMRA (20) (Re-D1)

As mentioned in section 2.2.1, a new approach was needed to prepare multi-ligand based biotin derivatives. To this end commercially available biotin-PEG-Novatag resin **18** was used to prepare compound **19** through solid phase

peptide synthesis. The use of solid phase synthesis was necessary to reduce the purification steps required in liquid phase synthesis that drastically reduced the overall yield of the product. The reaction started by removing the Fmoc group on the resin using 20% piperidine in DMF. The deprotection was visualized by TLC using the Kaiser test.[17] After washing the resin with DMF, DCM and DMF, FmocSAAC-lysine was activated by HATU in the presence of DIPEA in DMF and added to the resin. Following the removal of the next Fmoc group and washing the resin, TAMRA activated by HOAt and DIC in DMF was added. The resin was then washed, dried and kept overnight in a desiccator under vacuum. Compound **19** was then cleaved and released from the resin using a mixture of TFA/H_2O/TIPS and was precipitated in cold TBME and the product isolated in 91% yield (Scheme 2.4). Re-D1 **20** (Figure 2.5) was prepared according to the same scheme using Re-Fmoc-SAAC-Lysine in place of FmocSAAC-lysine[16] in 76% yield.

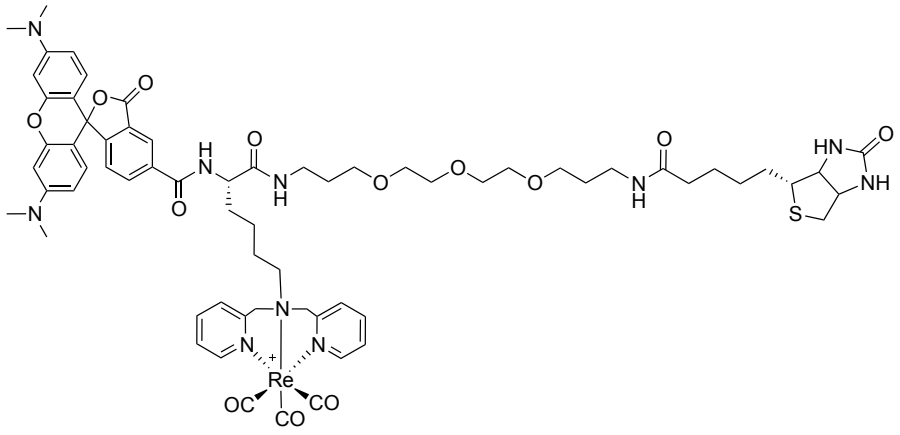

Figure 2.5 Structure of Re-D1 **20**

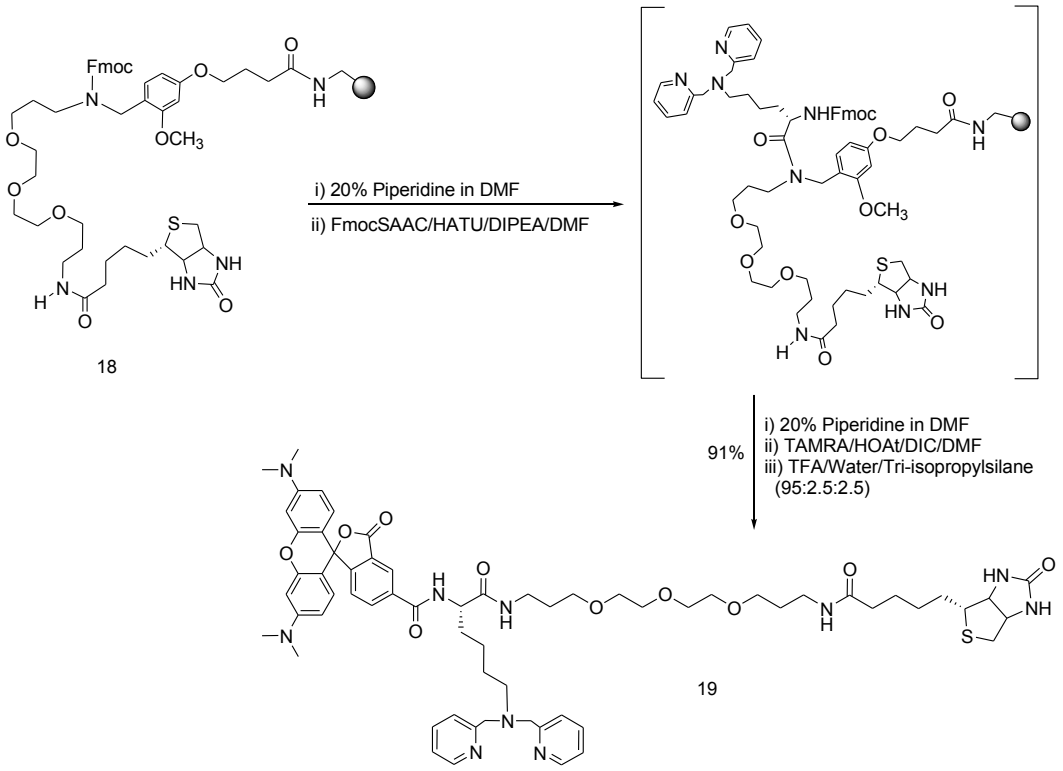

Scheme 2.4 Synthesis of D1 **19**

2.2.7 Synthesis of ^{99m}TcSAACBiotinTAMRA (21) (^{99m}Tc-D1)

^{99m}Tc-D1 was prepared at two different temperatures. The microwave-assisted reaction (76% yield) was significantly faster and had better yields compared to the one conducted at room temperature (63% yield) (Scheme 2.5). When the reaction was conducted in aqueous solution, the reaction yield was considerably lower (20%) but in the presence of 30% ethanol the reaction yields improved (76%). The identity of ^{99m}Tc-D1 was confirmed by HPLC via a co-

injection with the cold standard (Re-D1) where both compounds eluted at the same time (Figure 2.6).

The analytical HPLC gamma chromatogram for ^{99m}Tc-D1 showed a small peak that is likely associated with the oxidized form of biotin. To confirm this, an oxidizing agent (10 μL of peracetic acid) was added to the purified ^{99m}Tc-D1 (100 μL), and after 1 hr the mixture was analyzed by HPLC. The chromatogram showed a decrease of the peak associated with ^{99m}Tc-D1 (R_t = 12.4 min) and three new peaks that are likely D-biotinsulfoxide, L-biotinsulfoxide and biotinsulfone [18] derivatives of **21** (Figure 2.7).

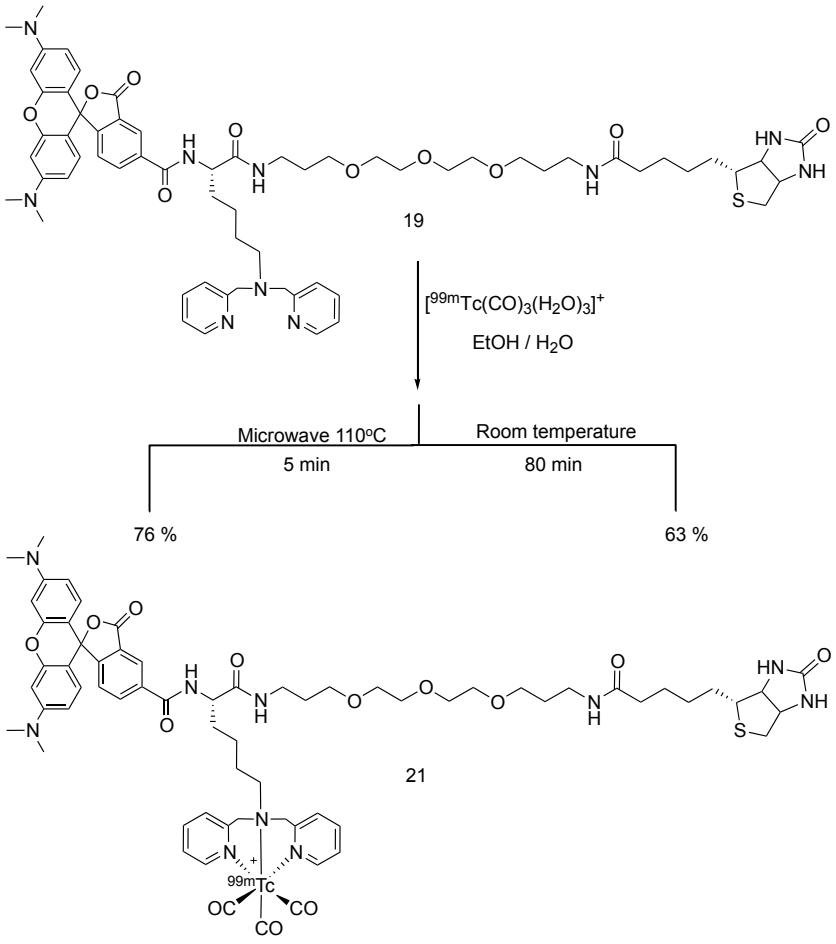

Scheme 2.5 Synthesis of ^{99m}Tc-D1 **21**

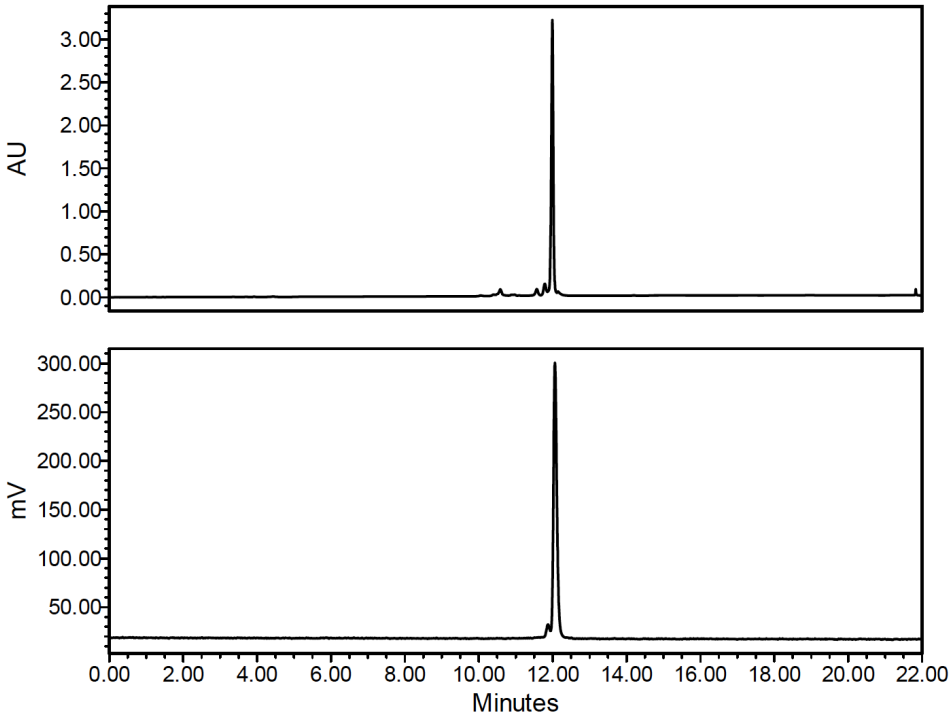

Figure 2.6 Top: HPLC-UV chromatogram of the co-injected Re-D1 and **bottom:** HPLC-γ chromatogram of purified ^{99m}Tc-D1.

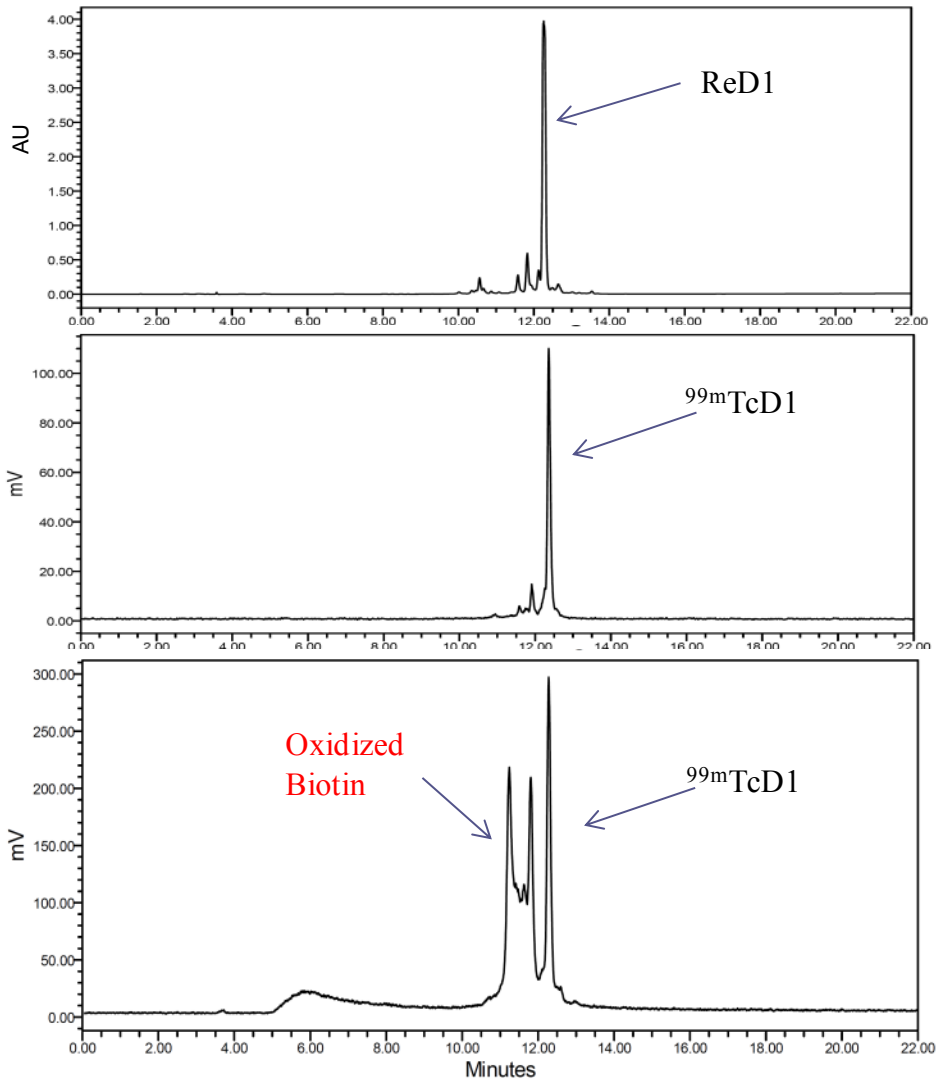

Figure 2.7 Top: HPLC-UV chromatogram of Re-D1, **middle:** HPLC-γ chromatogram of purified ^{99m}Tc-D1 and **bottom:** HPLC-γ chromatogram of ^{99m}Tc-D1 after 60 min incubation with peracetic acid.

2.2.8 Labeling MBs with ^{99m}Tc-D1

MBs were labeled with ^{99m}Tc-D1 and purified following the same procedure developed for ^{99m}Tc-L1-MBs preparation. The labeling of MBs with

^{99m}Tc-D1 resulted in a radiochemical yield of 30%. The crude reaction mixture was analyzed using a HiTrap size-exclusion cartridge attached to an HPLC, where the γ-trace showed two broad peaks; the first representing ^{99m}Tc-D1-MBs (R_t = 2.4 min) while the second is free ^{99m}Tc-D1 (R_t = 5.2 min) (Figure 2.8-top). After the magnetic bead purification and analyzing the sample in the HPLC, the γ-trace showed one peak associated with ^{99m}Tc-D1-MBs (Figure 2.8-bottom). It is worth noting that when MBs were incubated with ^{99m}Tc-D1 for 2.5 hr and analyzed in the HPLC, γ-trace of the reaction mixture showed no residual ^{99m}Tc-D1 indicating labeling was quantitative (Figure 2.9).

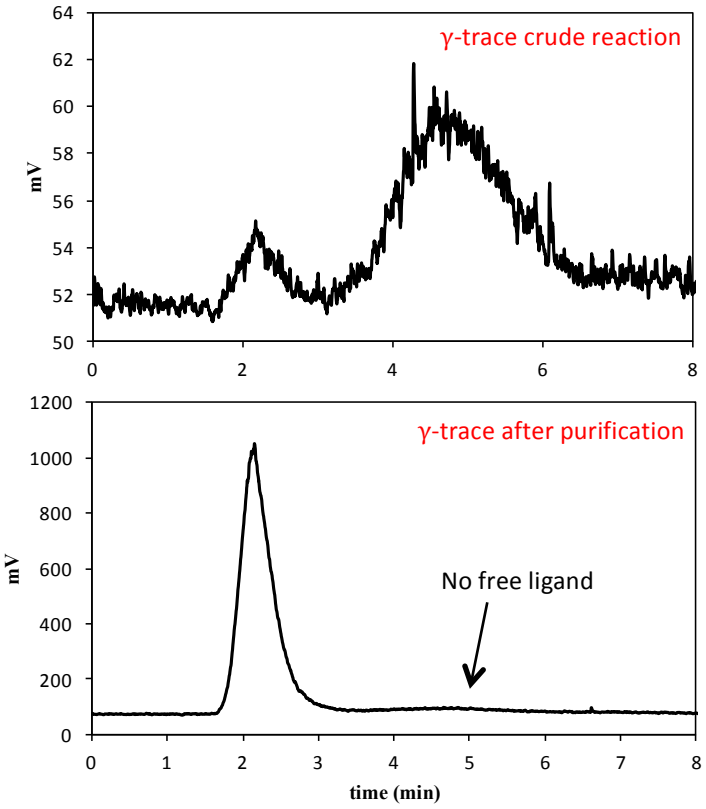

Figure 2.8 Analysis of MBs with a HiTrap size-exclusion cartridge attached to an HPLC. **Top:** HPLC-γ chromatogram of crude reaction mixture containing ^{99m}Tc-D1-MBs and free ^{99m}Tc-D1 and **bottom:** HPLC-γ chromatogram of ^{99m}Tc-D1-MBs after magnetic bead purification.

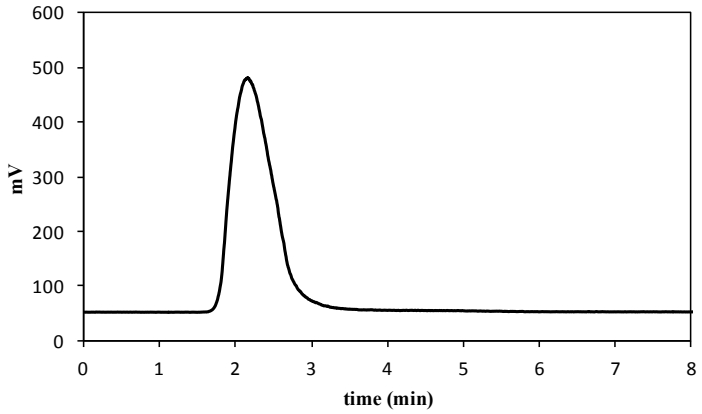

Figure 2.9 Analysis of MBs with a HiTrap size-exclusion cartridge attached to an HPLC. HPLC-γ chromatogram of crude reaction mixture after 150 min incubation time. The γ-trace only shows one peak representing ^{99m}Tc-D1-MBs.

2.2.9 Fluorescence microscopy of MBs labeled with Re-D1 (20)

Re-D1 was introduced to the reconstituted bubbles dropwise. The vial was allowed to sit at room temperature with periodic agitation for 45 min. The excess of Re-D1 was removed using the previously described magnetic bead purification method. A sample of Re-D1-MBs (10 μL) and unconjugated MBs (MB_C) was imaged using an Olympus BX-51 optical microscope fitted with a rhodamine filter.

When imaging MB_C under fluorescent microscopy, no fluorescence was observed (Figure 2.10-left). While after labeling MB_C with Re-D1 and imaging under the same settings, a fluorescence signal was clearly evident (Figure 2.10-right). Furthermore, when comparing the bright-field image of MB_C to the fluorescent image of Re-D1-MBs we find that qualitatively, Re-D1 did not have

an effect on the shape of the MBs (Figure 2.11).

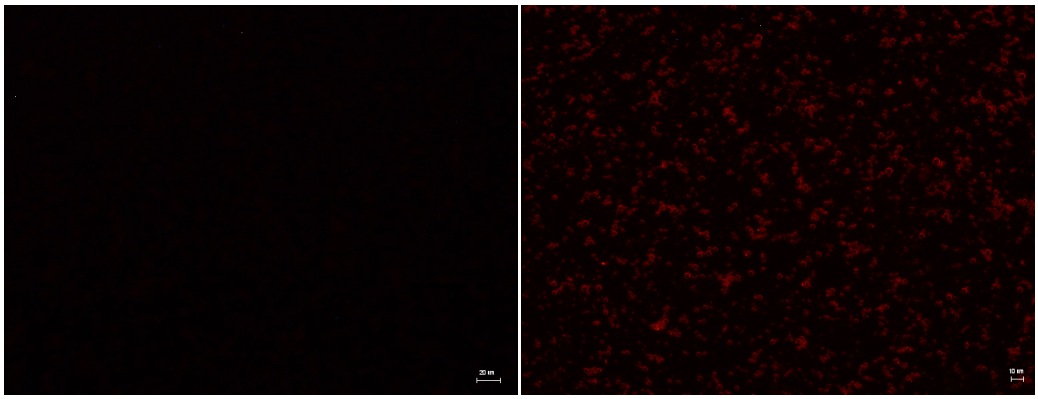

Figure 2.10 Left: fluorescent microscopy image of MB_C before labeling with ReD1 and **right:** fluorescent microscopy image of MB_C after labeling with Re-D1.

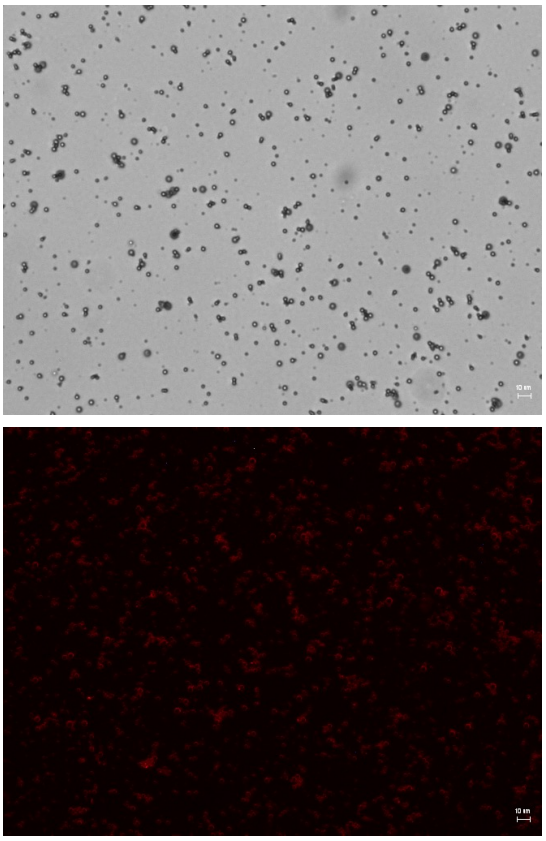

Figure 2.11 Top: Brightfield microscopy image of MB_C before labeling with ReD1 and **bottom:** fluorescent microscopy image of MB_C after labeling with Re-D1.

2.2.10 Coulter counter studies

To assess the effect of labeling and magnetic bead purification procedure on MBs stability in a more quantitative manner, a Coulter counter study was initiated. As a control, a mock labeling experiment was conducted where saline was added to the MBs instead of the ligand. A sample of the MBs solution was taken, diluted in isotonic saline solution and counted on Z2 coulter counter fitted with a 50 μm aperture using a modified literature procedure.[19] The time points

chosen represent each step within the labeling and purification of the MBs (Figure 2.12).

After 45 min incubation time, about 50% of the MBs were intact while after the magnetic bead purification 30% of the original MBs stock were intact. The purified MBs were left on the bench for 2 hr and counted on the Coulter counter which showed that 72% of the purified MBs were still intact. The mean diameter of MBs was shown to be 2.8 ± 0.8 µm. The number of intact MBs obtained after the labeling and magnetic bead purification was 10.5×10^7 MBs/100 µL which is comparable to the amounts previously reported for *in vitro* and *in vivo* studies (5×10^7 MBs/ 100 µL).[20] Based on those observations, our platform for labeling and purification of MBs generates enough construct for *in vitro* and *in vivo* studies.

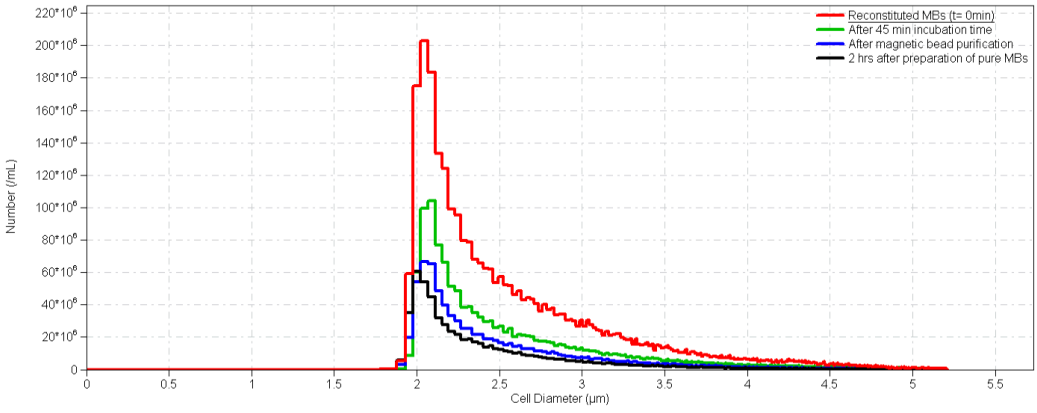

Figure 2.12 Representation of the size distribution and concentration (number/mL) of reconstituted MBs (**red**), MBs after 45 min incubation time (**green**), MBs after the magnetic bead purification (**blue**) and 2 hr after the

magnetic bead purification (**black**).

2.2.11 Testing the feasibility of attaching two different biotinylated-compounds to the surface of MBs

Before attaching a targeting vector to the surface of MBs in addition to the signaling agents prepared above, the feasibility and efficiency of attaching two different biotinylated ligands to the MBs was assessed. More specifically, there is a need to show the ability to attach the signaling agent with reasonable radiochemical yield after loading the MBs with a biotinylated compound. To this end Re-D1 **20** was loaded on the MBs to 50% capacity for 45 min and mixture was divided to 5 equal fractions. Each fraction of Re-D1-MBs was loaded with ^{99m}Tc-L1 **17** to a 25%, 50%, 75% and 100% loading capacity respectively. After 45 min incubation time with **17**, MBs were purified with the magnetic beads and radiochemical yield was found to be 20%, 14%, 13% and 10% respectively. The fifth fraction of Re-D1-MBs was loaded with a 60% loading capacity of ^{99m}Tc-L1 for 150 min and the radiochemical yield was 35% after one round of magnetic bead purification.

Looking at the HPLC analysis of all the MBs samples, one round of purification of the MBs incubated for 45 min with ^{99m}Tc-D1 was not sufficient to remove all of the free ^{99m}Tc-D1, so the purification process was repeated (Figure 2.13). While a single round of purification of the MBs that were incubated for 250

min with ^{99m}Tc-D1 was sufficient to get rid of excess ^{99m}Tc-D1(Figure 2.14).

The radiochemical yield achieved by Lazarova and coworkers was 30% after 45 min incubation time and quantitative after 2 hr.[12] Labeling of ^{99m}Tc-L1 after preloading the MBs with Re-D1 showed that even in the presence of a non-radioactive biotinylated standard (which can be replaced by a biotinylated targeting vector of interest) on the MBs, it is possible to attach two different biotinylated compounds to the MBs and still have sufficient sites for binding a radiolabeled ligand.

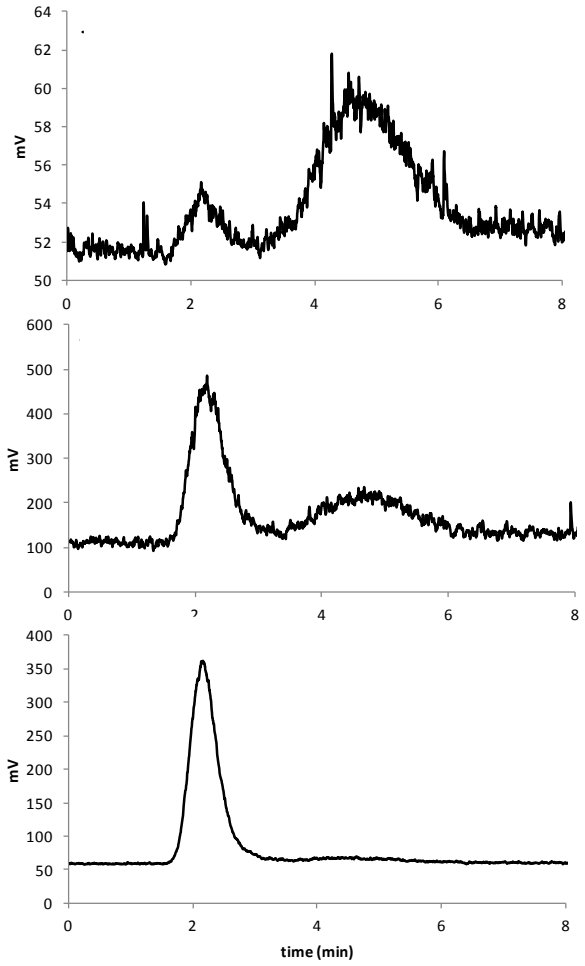

Figure 2.13 Analysis of MBs with a HiTrap size-exclusion cartridge attached to an HPLC. The mixture contained 50% Re-D1 and 50% ^{99m}Tc-L1 loaded on MBs for 45 min. **Top:** HPLC-γ chromatogram of crude reaction mixture containing Re-D1-^{99m}Tc-L1-MBs and free ^{99m}Tc-L1+ Re-D1, **middle:** HPLC-γ chromatogram of mixture after one purification step and **bottom:** HPLC-γ chromatogram of mixture after the second purification step showing only one peak representing Re-D1-^{99m}Tc-L1-MBs.

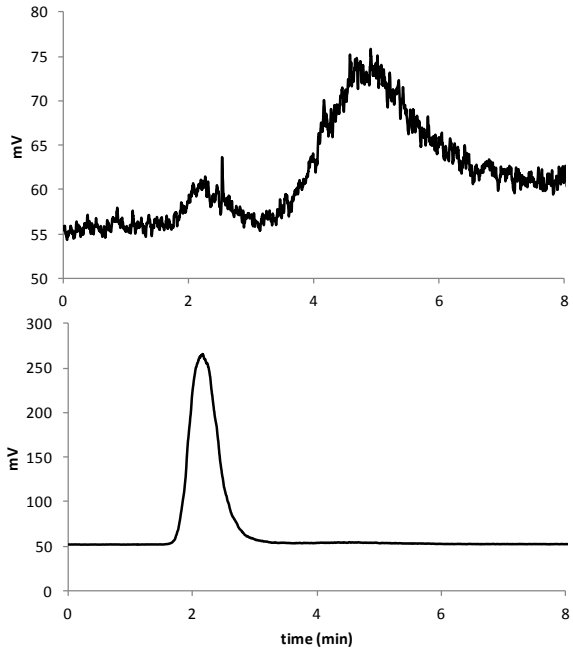

Figure 2.14 Analysis of MBs with a HiTrap size-exclusion cartridge attached to an HPLC. The mixture contained 50% Re-D1 and 60% ^{99m}Tc-L1 loaded on MBs for 150 min. **Top:** HPLC-γ chromatogram of crude reaction mixture containing Re-D1-^{99m}Tc-L1-MBs and free ^{99m}Tc-L1+ Re-D1, **bottom:** HPLC-γ chromatogram of mixture after one purification step showing one peak representing Re-D1-^{99m}Tc-L1-MBs.

2.3 Preparation of targeted multi-modal MBs using the Parallel Tagging Strategy (PTS)

2.3.1 Vascular Endothelial Growth Factor Receptor 2 (VEGFR2)

Vascular Endothelial Growth Factor Receptor2 (VEGFR2) is a tyrosine kinase, which upon activation triggers multiple signaling pathways that contribute

to angiogenesis.[21] VEGFR2 is overexpressed on tumour cells making it a good target for tumour angiogenesis imaging and therapeutic intervention.[21] Gambhir and coworkers reported the biodistribution of MBs that were targeted to VEGFR2 using an anti-VEGFR2 antibody. In this study, the antibody was radiofluorinated using N-succinimidyl-4-[^{18}F]fluorobenzoate (SFB)[22] where biodistribution showed 1.14% ID/g in the tumour at 4 min, 1.35% ID/g at 60 min and rapid clearance of the radiolabeled antibody from the blood which was 24.5% ID/g at 30 sec, 8.8% ID/g at 4 min and 0.5% ID/g at 60 min.[22] Typically, radiolabeled antibodies have long circulation times where blood levels remain elevated for more than 3 days (biological half-life > 72 hr).[23]

The MBs reported by Gambhir and coworkers had the radionuclide attached to the targeting vector and not the MBs. An alternative and more general approach involves labeling the MBs directly in concert with a targeting vector. To demonstrate the feasibility of this approach, VEGFR2-targeted and ^{99m}Tc-labeled MBs were prepared through the Parallel Tagging Strategy (PTS). This was done by attaching a biotinylated derivative of anti-VEGFR2 antibody to the surface of the streptavidin-coated MBs followed by the addition of a biotinylated signaling agent (optical and/or radioactive) (Figure 2.2).

2.3.1.1 Loading study of antiVEGFR2-Biotin on MBs

Before preparing the radiolabeled and VEGFR2-targeted MBs, the loading of the anti-VEGFR2-Biotin on MBs was evaluated. Streptavidin coated MBs were

reconstituted according to the manufacturers instructions and the solution containing MBs was divided into 5 equal fractions (100 μL each). To each fraction different amounts of anti-VEGFR2-biotin was added (0%, 25%, 50%, 75% and 100% MBs loading capacity) and the mixture incubated on a shaker for 30 min at room temperature. FITC-anti-biotin was then added to label any unbound anti-VEGFR2-biotin and excess FITC-anti-biotin was removed using biotin coated magnetic beads and a magnet. Fluorescence of the purified material was measured using a plate reader (excitation at 495 nm, emission at 520 nm) and the amount of anti-VEGFR2-Biotin not bound to the MBs was quantified using a calibration curve (Figure 2.15) and the amount of anti-VEGFR2-biotin loaded on the MBs determined (Figure 2.16).

Not surprisingly, loading of the biotinylated antibody increased with increasing amounts of antibody added to the MBs. Nevertheless, the loading did not reach the maximum after 30 min incubation time even when adding 100% loading capacity, which shows that there are still binding sites on MBs to attach the signaling agent after 30 min incubation (Figure 2.16).

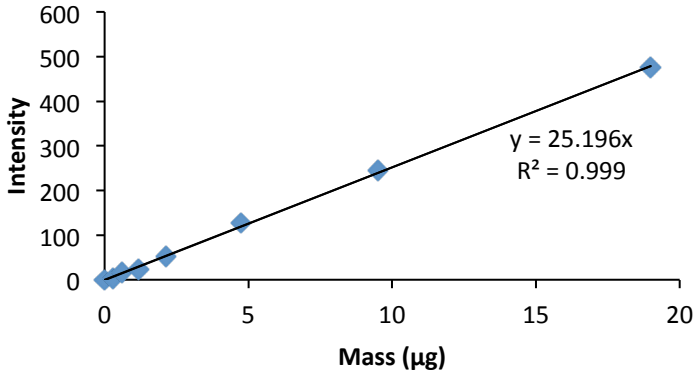

Figure 2.15 Plot representation of the relationship between µg of FITC-anti-biotin pre-incubated with anti-VEGFR2-biotin (1:1) and fluorescence intensity.

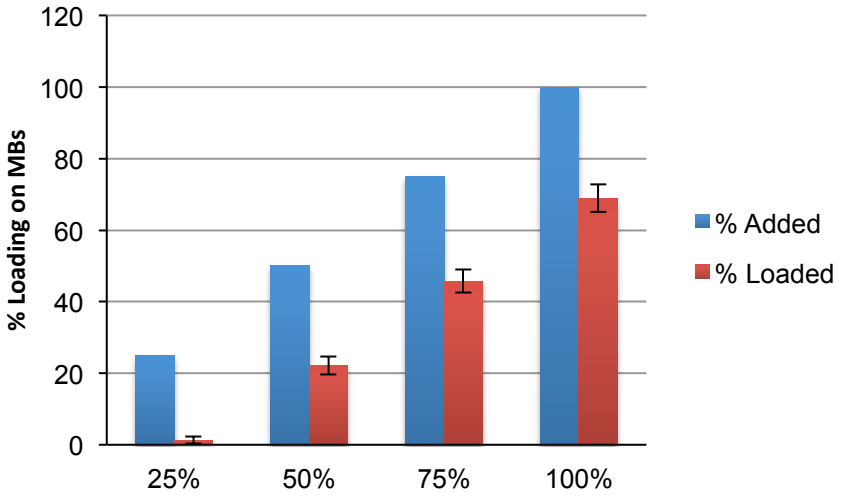

Figure 2.16 Comparison of the percent loading of anti-VEGFR2-biotin on MBs obtained between samples containing different amount of antiVEGFR2-biotin.

2.3.1.2 Determining VEGFR2-expressing cell lines through western blot analysis

Prior to evaluating targeted MBs, VEGFR2-expression in a series of tumour cell lysates was studied through immunoblotting. Briefly, 10 μg of protein from each cell lysate were loaded on a 10% Mini-PROTEAN TGX Precast gels. The protein extracts of the cell lysates were fractionated by SDS-PAGE and electro-transferred to polyvinylidenedifluoride (PVDF) membranes. The PVDF membrane was incubated with a rabbit anti-VEGFR2 primary antibody in a 1:250 dilution overnight at 4 °C. After washing the membrane with goat anti-rabbit secondary antibody a chemiluminescent reagent (ECF substrate) was then applied on the membrane for 5 min and an image collected.

PC3 (human prostate cancer cell line; lane 4), MHH (neuroblastoma cancer cells; lane 6) and H520 (squamous cell carcinoma; lane 10) had the highest VEGFR2 expression levels (Figure 2.17). Looking at the β-actin expression, there was relatively higher amounts of protein loaded in both MHH and PC3 compared to the other samples, for that reason H520 cells were chosen to evaluate the labeled MBs using a flow chamber assay.

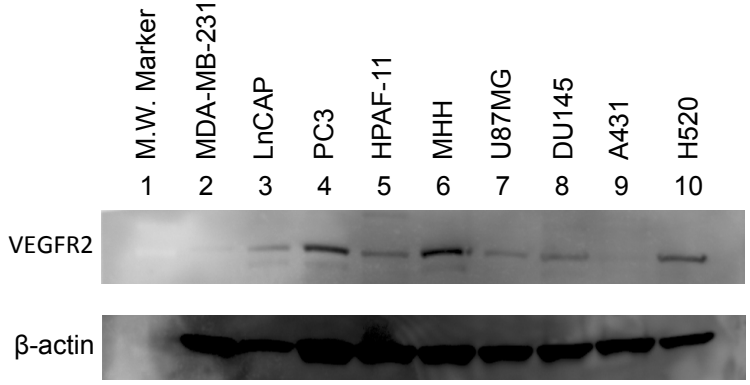

Figure 2.17 Western Blot analysis of VEGFR2 expression in cancer cell lysates. VEGFR2 expression in 9 different cancer cell lysates (10 µg of protein) using a rabbit anti-VEGFR2 primary antibody in a 1:250 dilution, a goat anti-rabbit secondary antibody in a 1:5000 dilution and a chemiluminescence detection system. ß-actin expression was used as loading control. VEGFR2 expression levels were the highest in PC3, MHH and H520 cell lysates.

2.3.1.3 Preparation of VEGFR2-targeted and ^{99m}Tc-labeled MBs

^{99m}Tc-L1 and commercially available biotinylated rat anti-mouse VEGFR2 monoclonal antibody were coupled to streptavidin coated MBs. This was accomplished by incubating MBs with ^{99m}Tc-L1 for 15 min then adding the antibody to the mixture and incubating for an additional 30 min at room temperature. Excess unbound ^{99m}Tc-L1 and antibody were removed by adding streptavidin coated magnetic beads to the bottom of the solution and incubating for 45 min followed by separating pure MBs from excess ligand using a magnet. Control MBs were labeled with ^{99m}Tc-L1 and a biotinylated isotype-matched

control mouse IgG antibody (MB_{IgG}). MBs conjugated to ^{99m}Tc-L1 (MB_{Tc}) alone were also prepared following the same procedure described above. Concentration of MBs used in *in vitro* experiments ranged from 3-6 × 10^6 MBs/mL.

2.3.1.4 Parallel plate flow chamber incubation assay

A flow chamber assay system was developed to assess the ability of MBs conjugates to bind targets of interest. H520 cells were plated in tissue culture dishes connected to a parallel-plate flow chamber (Figure 2.18). Cells were washed with PBS before exposure to labeled/targeted MBs (3-6 × 10^5 MBs). Due to the buoyancy of MBs, the chamber was inverted and incubation was done for 5 min followed by washing with PBS (1 mL). Cells were lysed in 1% Triton-X at 37 °C for 30 min. The amount of activity in MBs stock solution and in cell lysates was measured in a gamma counter. Protein content in each sample was determined using a BCA Pierce protein assay kit and the amount of activity was normalized to the amount of protein per sample. To further assess the specificity of the targeted ^{99m}Tc-labeled MB_V, blocking experiments were conducted (MB_V*), in which cells were incubated with anti-VEGFR2 (concentration= 30 μg/mL) for 30 min at room temperature prior to flow chamber assay. All experiments were done in triplicates and data is represented as counts per min (CPM) per μg of protein (Figure 2.19).

Targeted MBs (MB_V) showed significantly higher adherence to the VEGFR2-expressing cell line (14,640 CPM/μg of protein ± 1,319) compared to

isotype control (MB_{IgG}) (1,895 CPM/µg of protein ± 241) and non-targeted MBs (MB_{Tc}) (3,678 CPM/µg of protein ± 649). The assay indicated that the binding of MBs to H520 cells was due to the presence of anti-VEGFR2 and not non-specific binding. To further show the specificity of the targeted MBs (MB_V), H520 cells were incubated with anti-VEGFR2 for 30 min prior to incubation with MB_V showing low binding after blocking (2,225 CPM/µg of protein ± 139) (Figure 2.19).

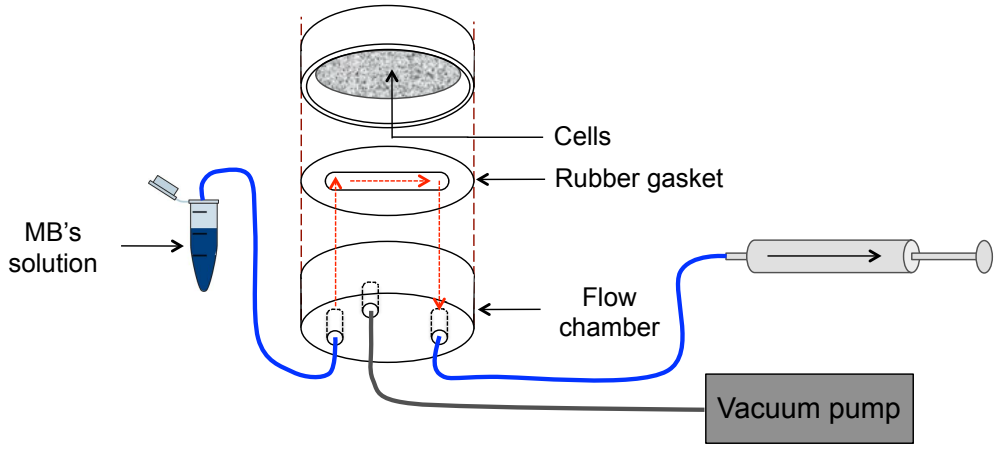

Figure 2.18 Schematic of the parallel plate flow chamber incubation assay setup.

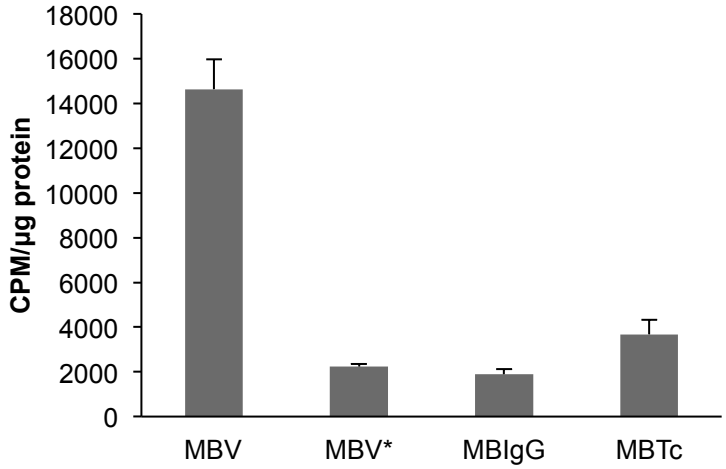

Figure 2.19 Bar graph representation of ^{99m}Tc-labeled VEGFR2 targeted MBs binding to H520 cells; data is represented as counts per min (CPM) normalized to µg of protein found in each sample. MB_V= VEGFR2-targeted and ^{99m}Tc-labeled MBs; MB_V*= VEGFR2-targeted and ^{99m}Tc-labeled MBs where cells were pre-treated with antiVEGFR2; MB_{IgG}= non-targeted ^{99m}Tc-labeled MBs loaded with IgG Isotype control; MB_{Tc}= non-targeted ^{99m}Tc-labeled MBs.

2.3.1.5 In vivo biodistribution studies of ^{99m}Tc-labeled MBs:

After demonstrating the specificity of the ^{99m}Tc-labeled MB_V to VEGFR2-expressing cell line *in vitro*, the next step was to evaluate the construct *in vivo*. Firstly, the biodistribution of ^{99m}Tc-labeled MB_V was assessed in CD1 nude female mice inoculated with H520 tumour xenografts. Each mouse was administered with about 370 kBq to 555 kBq of activity (100 µL in 0.09 % saline, 4×10^7 MBs) via tail vein injection. The animals were then euthanized at either 4 min (n= 3) or 60 min (n= 3) and organs were collected, weighed and activity

counted. A blocking study where an extra set of mice (n= 3) were injected with 125 μg of antiVEGFR2 24 hr before the study was also conducted at the 4 min time point. The data (Figure 2.20) showed no significant accumulation of ^{99m}Tc-labeled MB_V in H520 tumour at either the 4 min nor 60 min time point (0.23 %ID/g ± 0.02 and 0.14 %ID/g ± 0.06 respectively). In addition, no significant reduction of activity in the tumour was observed in the blocking study at 4 min (0.21 %ID/g ± 0.02). The general biodistribution of ^{99m}Tc-labeled MB_V looked similar between the studies and comparable to the general distribution of non-targeted ^{99m}Tc-labeled MBs (MB_{Tc}).[12] Fast blood clearance of ^{99m}Tc-labeled MB_V (5.28 %ID/g ± 1.01 at 4 min, 0.61% ID/g at 60 min) was observed which is comparable to the results observed by Gambhir and coworkers.[22] Otherwise at 4 min, high accumulation in the gall bladder (7.11 %ID/g ± 1.31), liver (42.62 %ID/g ± 3.59), lungs (8.82 %ID/g ± 1.61) and spleen (70.50 %ID/g ± 16.17) were observed which is likely due to uptake by the reticuloendothelial system (RES).[24,25]

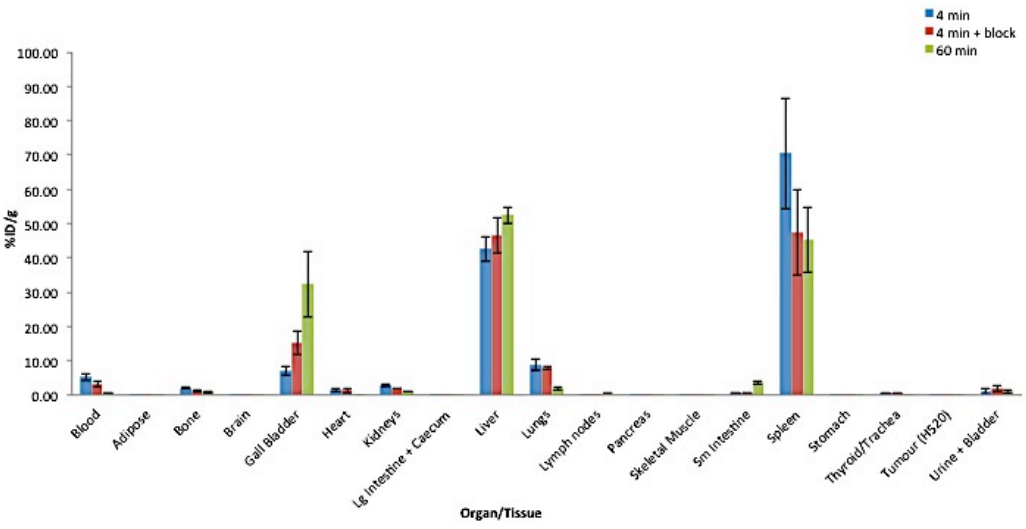

Figure 2.20 Biodistribution of ^{99m}Tc-labeled MB_V with and without blocking in CD1 nude H520 tumour-bearing female mice. Mice (n= 3 per study) were injected between 370 kBq and 555 kBq and sacrificed at either 4 min or 60 min post injection. Blocking study was conducted at the 4 min time point where the mice were injected with 125 µg of antiVEGFR2 24 hr before study. Data are expressed as percent injected dose per gram of tissue/fluid (%ID/g).

Further *in vivo* biodistribution studies were conducted to directly compare between the distribution of VEGFR2-targeted ^{99m}Tc-labeled MB_V and non-targeted ^{99m}Tc-labeled MBs (MB_{Tc}). Mice (n= 3 per study) were administered with the same amount of activity (between 370 - 555 kBq) and sacrificed at the 4 min time point. Tissues were collected, weighed, counted for activity and a bar graph representation of %ID/g was produced (Figure 2.21). No accumulation in the tumour of either construct was observed; 0.22 %ID/g ± 0.09 and 0.24 %ID/g ± 0.09 for the targeted and non-targeted MBs respectively. When looking at the biodistribution of ^{99m}Tc-labeled MBs, higher retention in the blood (19.88 %ID/g

± 3.28), and accumulation in the lungs (39.30 %ID/g ± 7.29) and spleen (72.49 %ID/g ± 17.33) were observed.

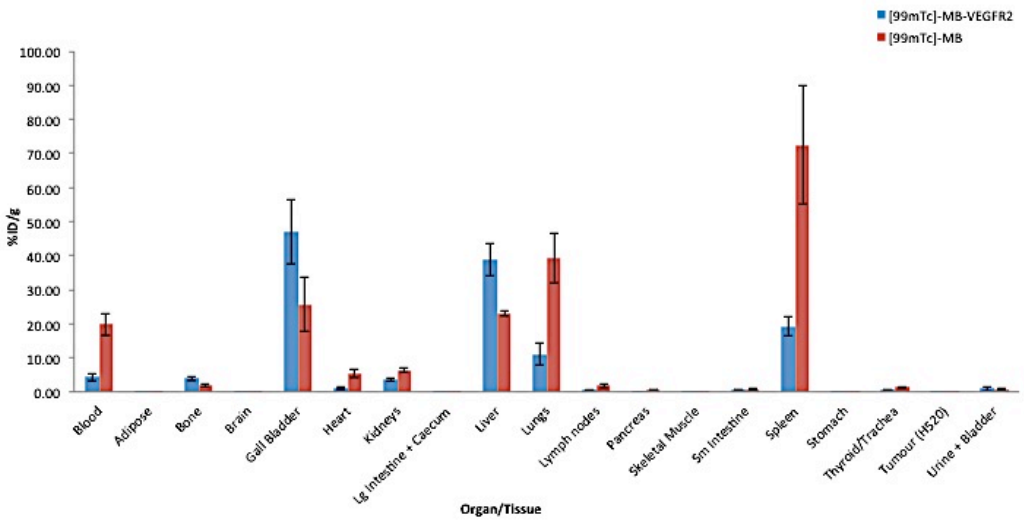

Figure 2.21 Biodistribution of VEGFR2-targeted ^{99m}Tc-labeled MB_V and non-targeted ^{99m}Tc-labeled MBs (MB_{Tc}) in CD1 nude H520 tumour-bearing female mice. Mice (n= 3 per study) were injected with between 370 kBq and 555 kBq and sacrificed at 4 min post injection. Data are expressed as percent injected dose per gram of tissue/fluid (%ID/g).

One additional study was conducted using a SKOV-3 xenograft mouse model which was previously used for targeted US imaging of VEGFR2.[20] VEGFR2-targeted ^{99m}Tc-labeled MB_V were injected in SKOV-3 mouse xenograft model (n= 3) and allowed to bind for 4 min before sacrificing the animals. The biodistribution data (Figure 2.22) again showed low accumulation of VEGFR2-targeted ^{99m}Tc-labeled MB_V in the SKOV-3 tumour (0.34 %ID/g ± 0.03) with similar distribution to that found in H520 mouse tumour xenograft.

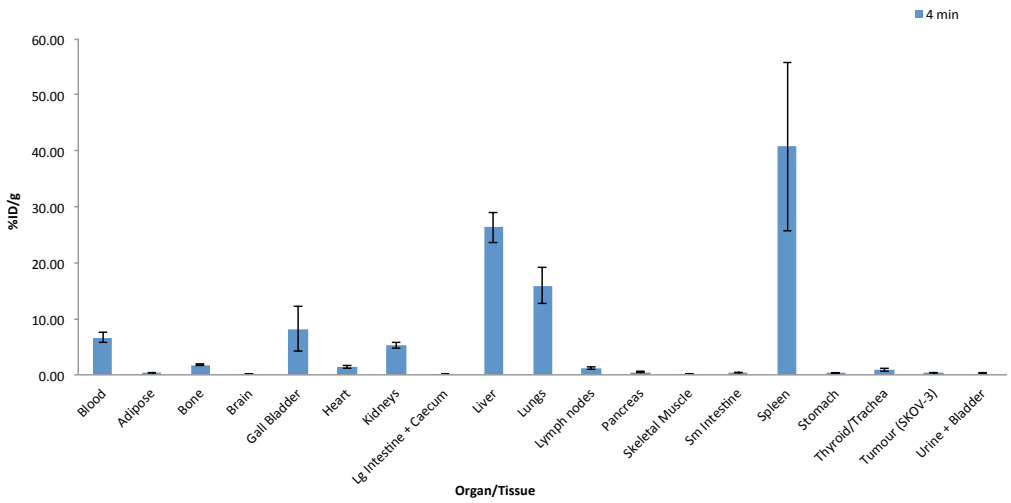

Figure 2.22 Biodistribution of VEGFR2-targeted ^{99m}Tc-labeled MB_V in CD1 nude SKOV-3 tumour-bearing female mice. Mice (n= 3 per study) were injected with activity between 370 kBq and 555 kBq and sacrificed at 4 min post injection. Data are expressed as percent injected dose per gram of tissue/fluid (%ID/g).

2.3.1.6 Immunostaining analysis of VEGFR2 expression on endothelial cells:

To determine if the low accumulation of VEGFR2-targeted ^{99m}Tc-labeled MB_V in the tumour was due to lack of VEGFR2 expression on endothelial cells, immunostaining studies were conducted. VEGFR2 was labeled by incubating the tissue slices with a rat anti-mouse VEGFR2 antibody and visualized using a fluorescein (FITC)-anti-rat IgG. In parallel the expression of endothelial cells was assessed by staining for CD31 cells using a rabbit anti-CD31 antibody and Cy5-conjugated donkey anti-rabbit IgG. To take into account signals coming from background or non-specific binding of either antibody, both primary antibodies were substituted with a control rat and rabbit IgG antibody respectively.

Fluorescent microscopy images (Figure 2.23) showed the expression of endothelial cells (CD31) and VEGFR2 on SKOV-3 tumour slices. Meanwhile, H520 tumour slices showed no evident expression of VEGFR2, suggesting that this model was not suitable for *in vivo* studies. Nevertheless, the pilot study in the SKOV-3 tumour model was not successful, concluding that these constructs are not able to target the site of interest *in vivo*.

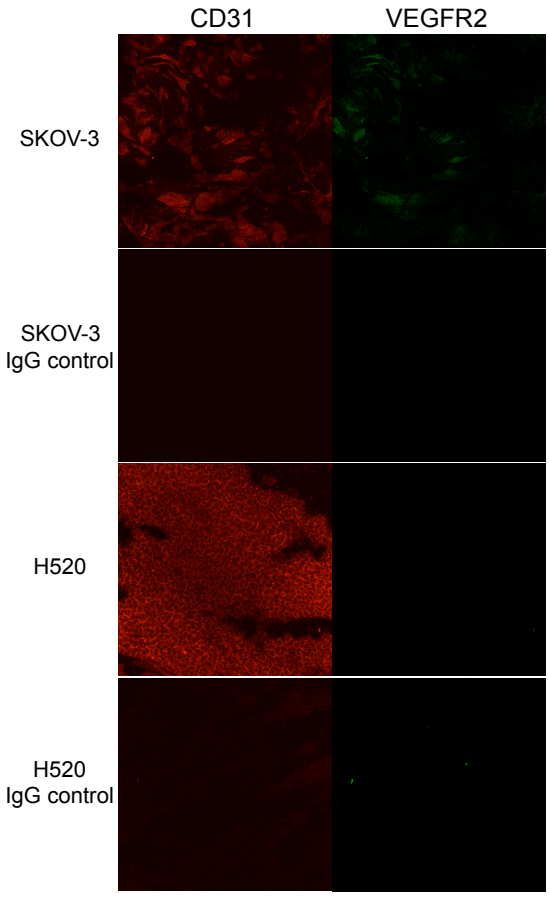

Figure 2.23 Immunofluorescence staining images of H520 and SKOV-3 tumour

tissue after staining for VEGFR2 and CD31. Left column are images visualized under a Cy5 filter (CD31) while the right column was visualized under a FITC filter (VEGFR2). All images were captured under the same settings and any observed fluorescence was qualitatively higher than background and non-specific binding control (IgG control).

Another attempt to use the parallel tagging strategy to target multi-modal MBs to the site of disease was conducted. This focused on targeting ^{99m}Tc-labeled MBs to prostate specific membrane antigen (PSMA), a well-studied marker of prostate cancer. More specifically, the use of a small-molecule targeting vector instead of a large antibody to target MBs was investigated. Small molecule based targeting vectors are less expensive and simpler to modify. Furthermore, the possibility of decreasing any steric hindrance effects by having small molecules on the surface of MBs instead of antibodies could potentially improve MBs target binding. This goal resulted in the need to develop a series of biotinylated PSMA-inhibitors.

2.3.2 Prostate Specific Membrane Antigen (PSMA)

Prostate specific membrane antigen (PSMA) is a 750 residue transmembrane glycoprotein normally expressed at low levels in prostate, liver, kidney and brain tissue.[26] PSMA is highly expressed in prostate carcinoma as well as neovasculature in other solid tumours and was shown to be an independent biomarker for the progression and recurrence of the disease.[27] While the specific function of PSMA in the prostate is not yet understood, it has been shown to offer

a growth advantage for prostate cancer cells grown in an environment with low levels of polyglutamated folates. As cells can only take up monoglutamated folate, the increased expression of PSMA in tumour tissues allows for the conversion of polyglutamated folates to a form that can be imported into the cell. PSMA has also been shown to bind monoglutamated folate suggesting a possible additional role in cell biology.[28] These findings along with the extracellular localization of PSMA make it an attractive target for the development of radiopharmaceuticals and other probes for both diagnosis and treatment.

A significant number of small molecule-based inhibitors of PSMA have been reported.[29-36] One prominent class of inhibitors are based on a dipeptide linked through a urea. More specifically, small molecules with the general formula Glu-urea-X (where X is a derivatized lysine) were reported and shown to selectively bind to PSMA with high affinity.[37-39] Several compounds in the series had good IC_{50} values in competitive cell binding assays run using LNCaP (PSMA+) cells. Using this construct, and in collaboration with Dr. Afaf Genady, a post doctoral fellow in the group, a series of biotin derivatives were conjugated to Glu-Urea-Lys with varying linkages and spacer lengths in good yields (65-74%) (Figure 2.24).

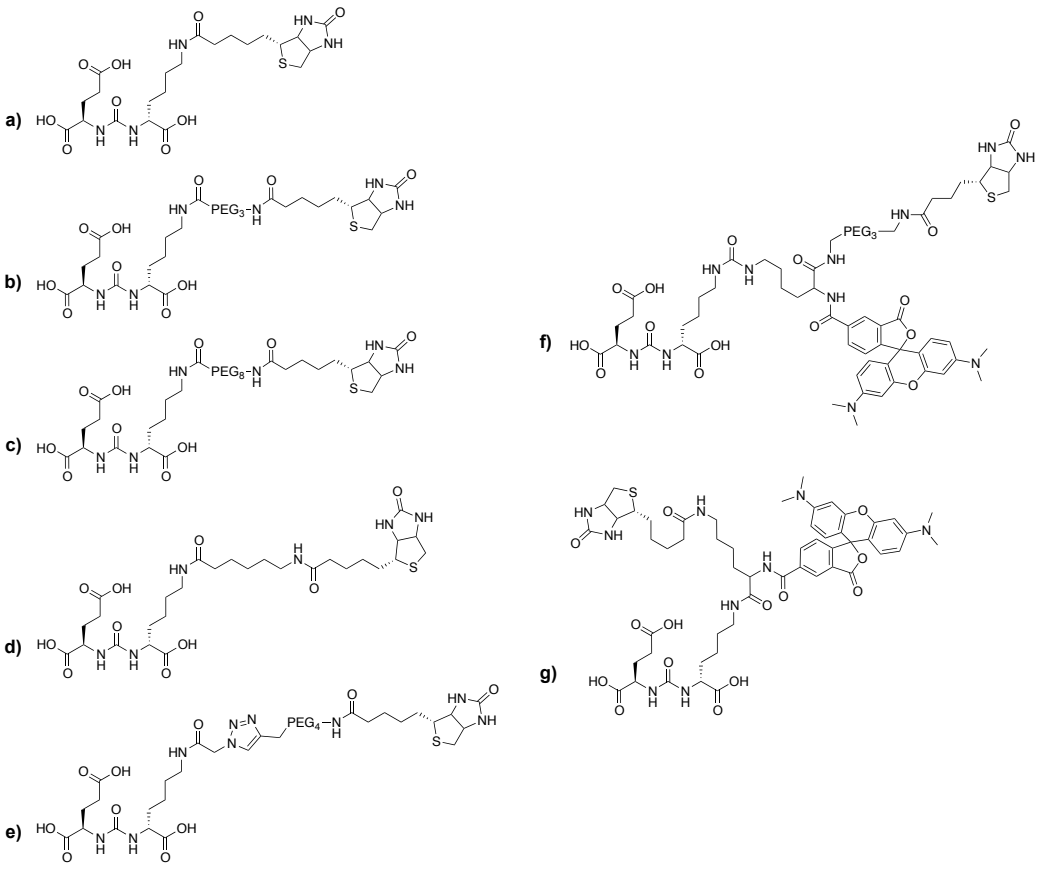

Figure 2.24 Summary of the synthesized biotinylated derivatives of the Glu-Urea-Lys PSMA inhibitors. Dr. Genady independently prepared compounds b, f, and g.

2.3.2.1 Synthesis of PSMA-Biotin (25)

Glu-Urea-Lys **23**[37] was synthesized by treating 3 equivalents of L-glutamic acid di-t-Bu ester with triphosgene generating the isocyanate derivative which was treated with Cbz-Lys-O(t-Bu) and the product isolated by column chromatography in 45% yield. The Cbz group was removed through hydrogenolysis generating **23** in quantitative yield (Scheme 2.6). Compound **23** was then treated with biotin-TFP-ester **7** and isolated in 35% yield before

deprotection using TFA. The final product was purified by HPLC and isolated in 74% yield (Scheme 2.7).

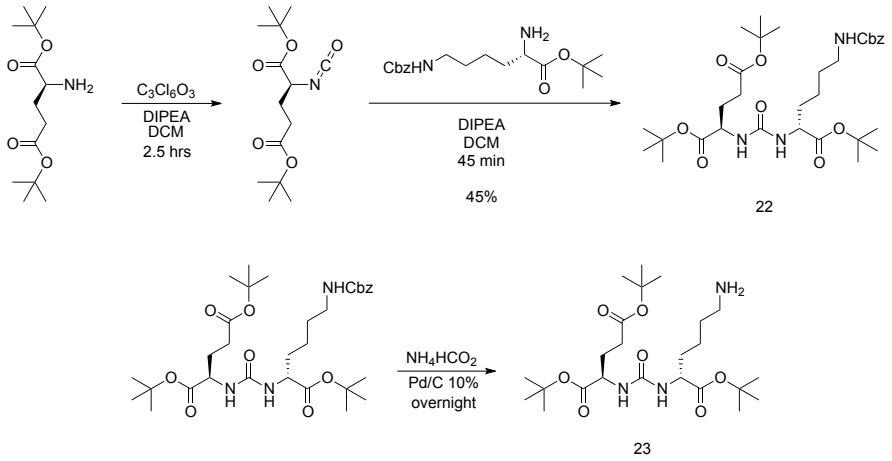

Scheme 2.6 Synthesis of Glu-Urea-Lys **23**

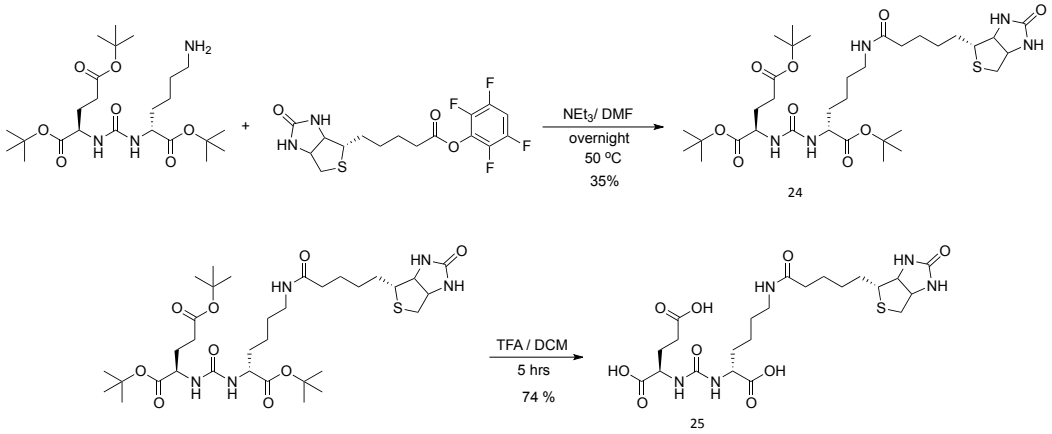

Scheme 2.7 Synthesis of PSMA-Biotin **25**

2.3.2.2 Synthesis of PSMA-PEG$_8$-Biotin (29)

NH_2-PEG_8-COOH was combined with biotin-TFP-ester **7** in DMF in the presence of TEA and heating to 50 °C for 24 hr. The mixture was then purified by

column chromatography and **26** was obtained in 77% yield. Biotinamido-PEG_8-COOH **26** was dissolved in DMF and heated to 80 °C under argon for 10 min. After cooling the mixture to room temperature, TEA then tetrafluorophenyl trifluoroacetate were added and stirred for 30 min. Solvents were removed under vacuum and the crude mixture was directly used in the next step. Biotinamido-PEG_8-ester **27** was combined with Glu-Urea-Lys **23** in the presence of TEA and heated at 50°C overnight. Product **28** was isolated in 80% yield and the t-butyl groups removed using a mixture of TFA and DCM to give **29** in 77% yield (Scheme 2.8).

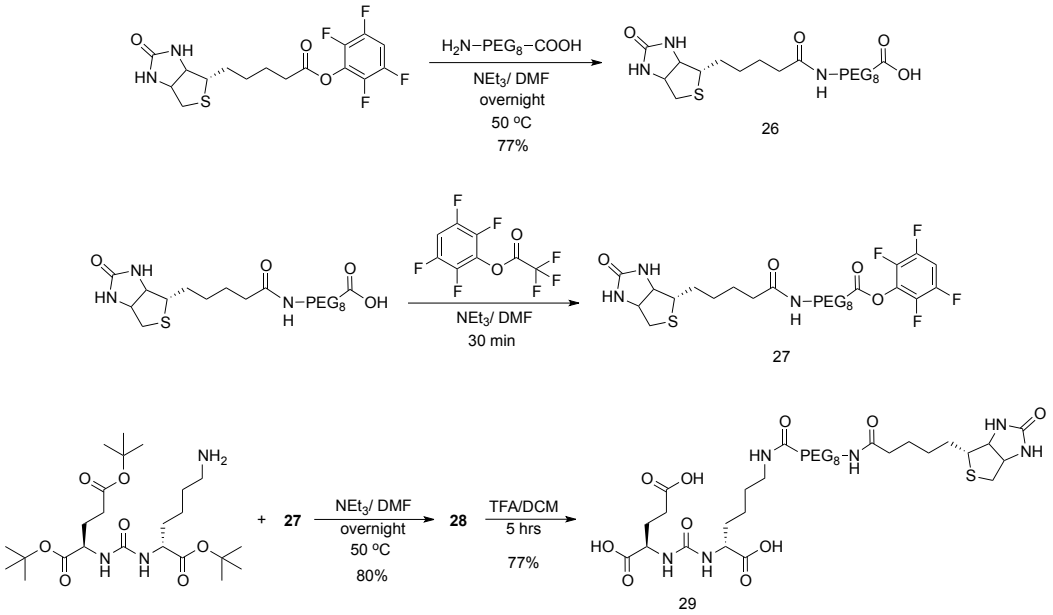

Scheme 2.8 Synthesis of PSMA-PEG_8-Biotin **29**

2.3.2.3 Synthesis of PSMA-Caproic-Biotin (33)

To introduce a different spacer group, biotin-TFP-ester **7** was coupled to

6-amino caproic acid in the presence of TEA in DMF at 75 °C under argon overnight. The mixture was concentrated under vacuum and a white solid formed which was dried under vacuum overnight prior to washing with THF. The resulting product **30** was isolated in 91% yield. Compound **30** was then combined with tetrafluorophenyl trifluoroacetate in the presence of TEA in DMF and DMSO at 80 °C under argon for 1 hr. Compound **31** was dried, left under vacuum, purified using a Biotage flash chromatography system and isolated in 96% yield. Finally, biotinamido-caproic-ester **31** was combined with Glu-Urea-Lys **23** in the presence of TEA at 50 °C overnight, purified using a Biotage flash system and isolated in 86% yield, whereupon the t-butyl protecting groups were removed using a mixture of TFA:DCM (1:1). Compound **33** was purified using semi-preparative HPLC and isolated in 61% yield (Scheme 2.9).

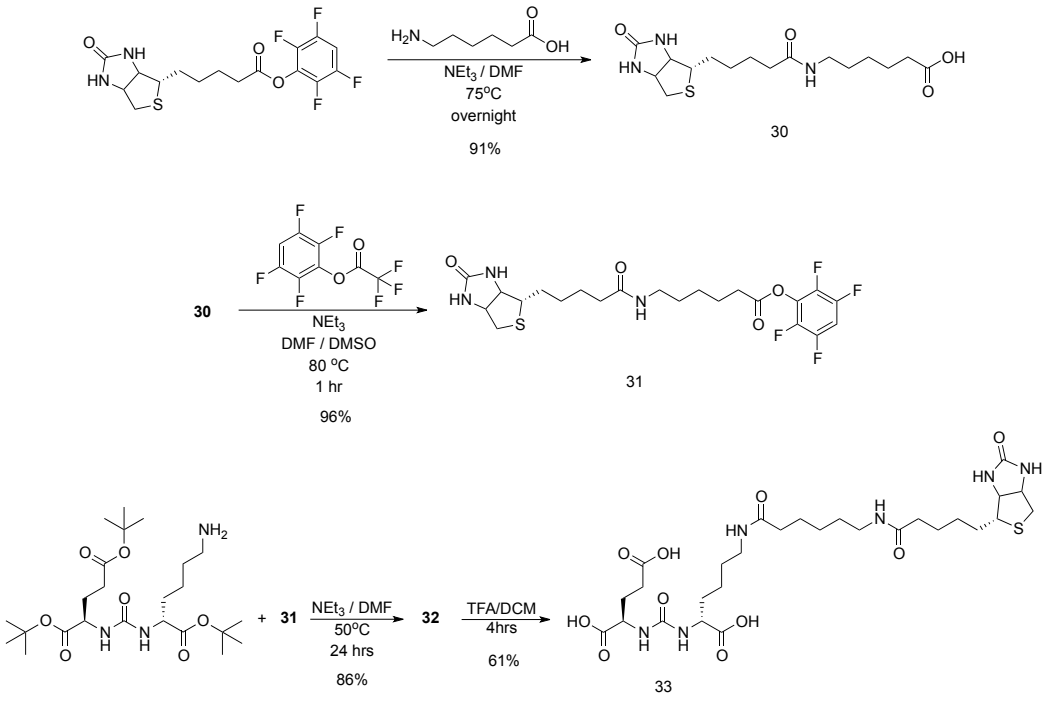

Scheme 2.9 Synthesis of PSMA-Caproic-Biotin **33**

2.3.2.4 Synthesis of PSMA-TAAG-PEG$_4$-Biotin (36)

A PSMA-inhibitor where a dinitrophenyl group was attached to Glu-Urea-Lys derivative through a triazole-PEG$_4$ linker was synthesized in our group previously (Figure 2.25).[43] High affinity of this compound to PSMA-expressing cells was observed (IC_{50}=15 nM). As a result, a similar compound was prepared where the dinitrophenyl group was replaced with biotin and TAAG was not iodinated. To this end, Glu-Urea-Lys **23** was dissolved in MeOH solution before adding methyl-2-azidoacetate and DIPEA dropwise. The reaction was left to stir at reflux for 48 hr before removal of solvent and purification using a flash system. Compound **34** was isolated in 65% yield as an oil. Dr. Genady synthesized a

derivative of biotin attached to an alkyne through a PEG_4 spacer, which was combined with **34** in a copper catalyzed click reaction. The optimal solvent was found to be a 1:1 tert-butanol:H_2O solution and the reaction was heated to 120 °C in a microwave in the presence of $CuSO_4$ and sodium ascorbate for 15 min. Solvent was removed and compound **35** was purified and isolated in 63% yield. The t-butyl protecting groups were then removed by mixing **35** in a 2:1 TFA:DCM solution and heating at 75 °C for 15 min in a microwave. Finally, compound **36** was purified using semi-preparative HPLC and isolated in 56% yield (Scheme 2.10).

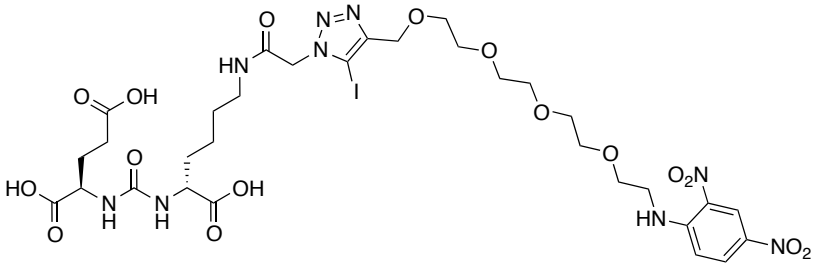

Figure 2.25 Structure of DNP-PEG_4-TAAG-PSMA

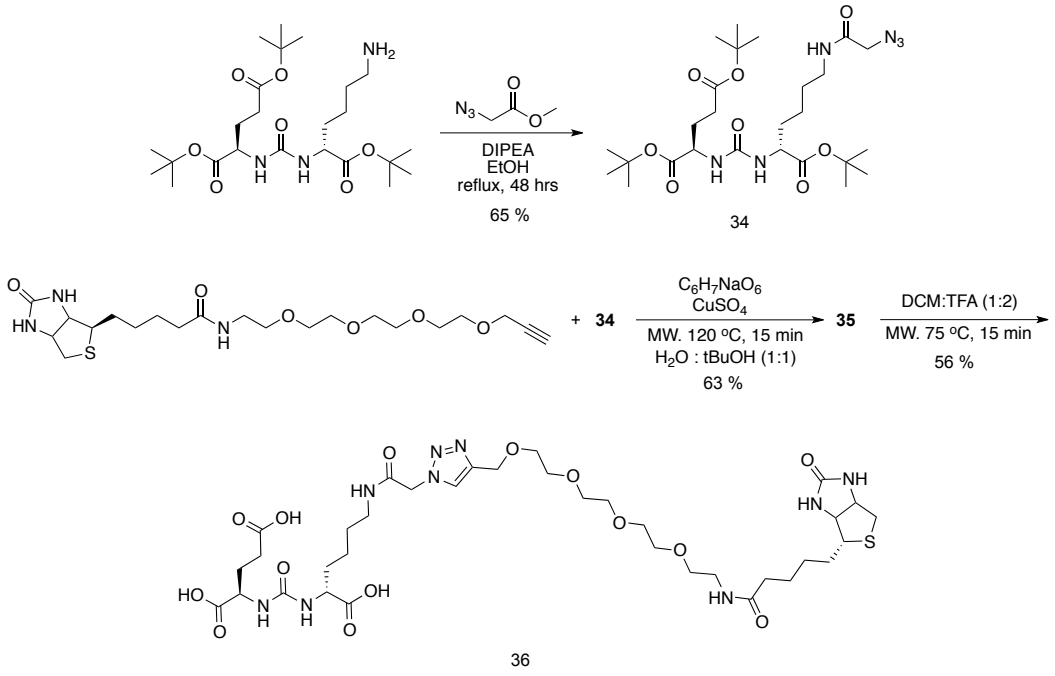

Scheme 2.10 Synthesis of PSMA-TAAG-PEG$_4$-Biotin **36**

2.3.2.5 LNCaP cell PSMA competition binding assay

This assay was performed with the assistance of Nancy Janzen. LNCaP cells were plated at 2.1×10^5 cells per well in 24-well plate 2 days before running the assay. Some wells were incubated with media only to assess the background binding to the assay plates and tubes. The assay was conducted in triplicate at each concentration with binding buffer (RPMI, 0.5%BSA). Cells were incubated for approximately 1 hr with a mixture of ^{125}I-TAAG-PSMA (a previously developed PSMA inhibitor in the group,[40] Figure 2.26a, 1 nM) and either 0, 0.1, 1, 10, 100, 1000 and 10000 nM of test compound (biotinylated-derivative of the PSMA inhibitor). As a positive control, the synthesized biotinylated derivatives were substituted with 2-(phosphonomethyl)pentanedioic acid (PMPA), which is a

known PSMA inhibitor[29] (Figure 2.26b). Wells without cells were incubated with 1 nM ^{125}I-TAAG-PSMA to measure any non-specific binding of the radiolabeled compound. Cells were then resuspended, washed with binding buffer and the resulting cell pellets after centrifugation lysed using RIPA buffer at 37 °C for 30 min. Activity in cell lysates were then counted in a gamma counter, dose-response curves generated and IC_{50} values calculated (Figure 2.27).

Figure 2.27 is a summary of the dose response curves generated and figure 2.28 contains the structures and calculated IC_{50} values of the tested biotinylated PSMA inhibitors. The IC_{50} values obtained for these compounds were relatively high compared to the best compounds developed by Maresca and coworkers (IC_{50} < 20 nM).[37] This was problematic because in order to be able to capture the relatively large MBs on the surface of PCa, the targeting vector needs to bind to PSMA quickly and with high affinity. Nevertheless, the compounds with the highest affinity to PSMA (Figure 2.28 b, d, e and f) were evaluated in the flow chamber incubation assay.

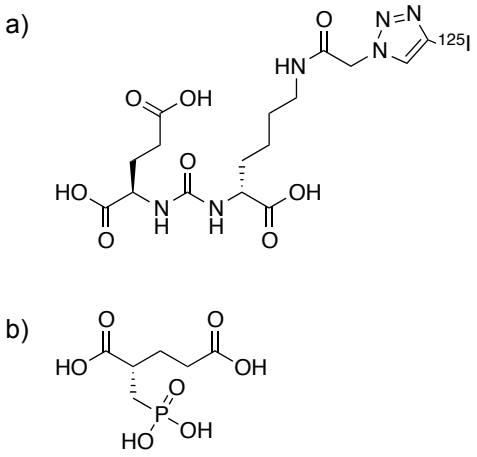

Figure 2.26 a) Structure of ^{125}I-TAAG-PSMA; **b)** Structure of PMPA

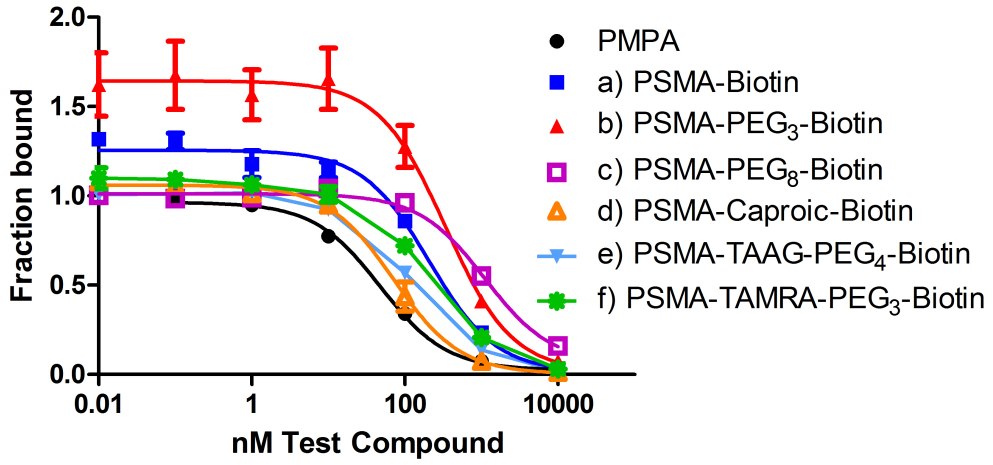

Figure 2.27 Competition binding curve showing the fraction bound as a function of concentration. The IC_{50} values of the tested compounds with respect to ^{125}I-TAAG-PSMA was found to be **a)** 206 nM; **b)** 337 nM; **c)** 948 nM; **d)** 114 nM; **e)** 126 nM and **f)** 198 nM.

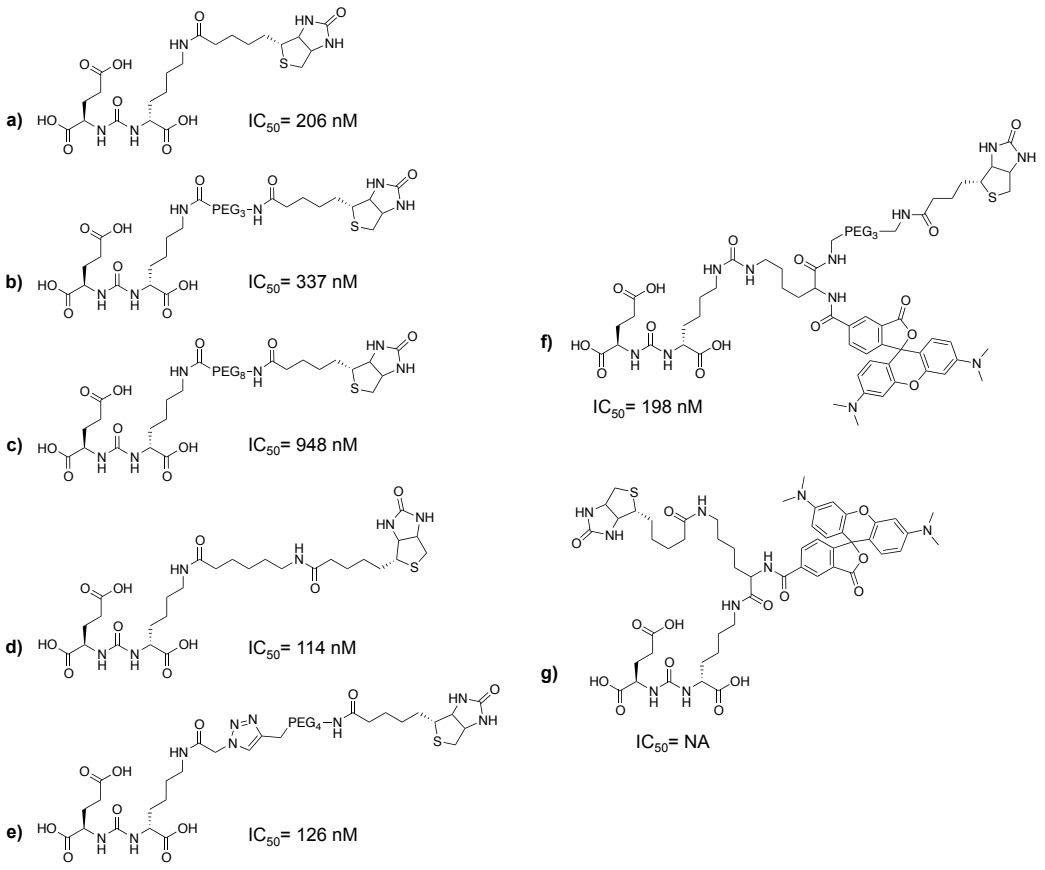

Figure 2.28 Summary of the synthesized biotinylated derivatives of the Glu-Urea-Lys PSMA inhibitor and their calculated IC_{50} values after testing in PSMA competition binding assay.

2.3.2.6 Parallel plate flow chamber incubation assay

The compounds with the highest affinity to PSMA were loaded on ^{99m}Tc-labeled MBs and binding of MBs to PSMA-expressing cells was conducted in a flow chamber incubation assay. The compound where biotin was directly attached to the PSMA inhibitor (PSMA-Biotin, Figure 2.28**a**) was not tested due to the known need to have a spacer for the inhibitor to reach the 20 Å deep active site of

PSMA.[41,42]

Transfected PC3 cells that express PSMA were used instead of the known LNCaP cells because of their better adhesion to the flow chamber system. Cells were plated on 35 mm Corning® tissue culture dishes 2 days prior to assay. The assay was set-up and conducted similarly to that described in section 2.3.1.4. Activity levels in cells lysates were measured in a gamma counter and protein content measured using a BCA Pierce protein assay kit. The extent of binding of MBs was evaluated by normalizing the amount of activity over protein levels within each sample and represented as counts per min over µg of protein (CPM/µg). As a control, non-targeted ^{99m}Tc-labeled MBs were loaded with a biotinylated IgG isotype antibody and evaluated.

The extent of binding of the targeted MBs during the flow assay was 10 fold higher for PSMA expressing PC3 cells compared to non-targeted ^{99m}Tc-labeled MBs (Figure 2.29**b**). When loading the ^{99m}Tc-labeled MBs with the biotinylated PSMA inhibitor with the highest affinity, binding of MBs was the highest. While MBs loaded with the lowest affinity ligand resulted in the lowest binding (Figure 2.29**b**). Unfortunately, when comparing the CPM/µg of protein found with the best PSMA-binding ^{99m}Tc-labeled MBs (10,551 ± 4,511 CPM/µg of protein), the amount of binding was still less than that of ^{99m}Tc-labeled MBs to VEGFR2-expressing cells (14,640 ± 1,319 CPM/µg of protein) (Figure 2.29-**b1**, Figure 2.19-MB_V respectively). Due to the unsuccessful *in vivo* studies on the

VEGFR2-targeted ^{99m}Tc-labeled MBs, which had higher *in vitro* binding, future work with the parallel tagging strategy was terminated and the focus shifted to other derivatization strategies.

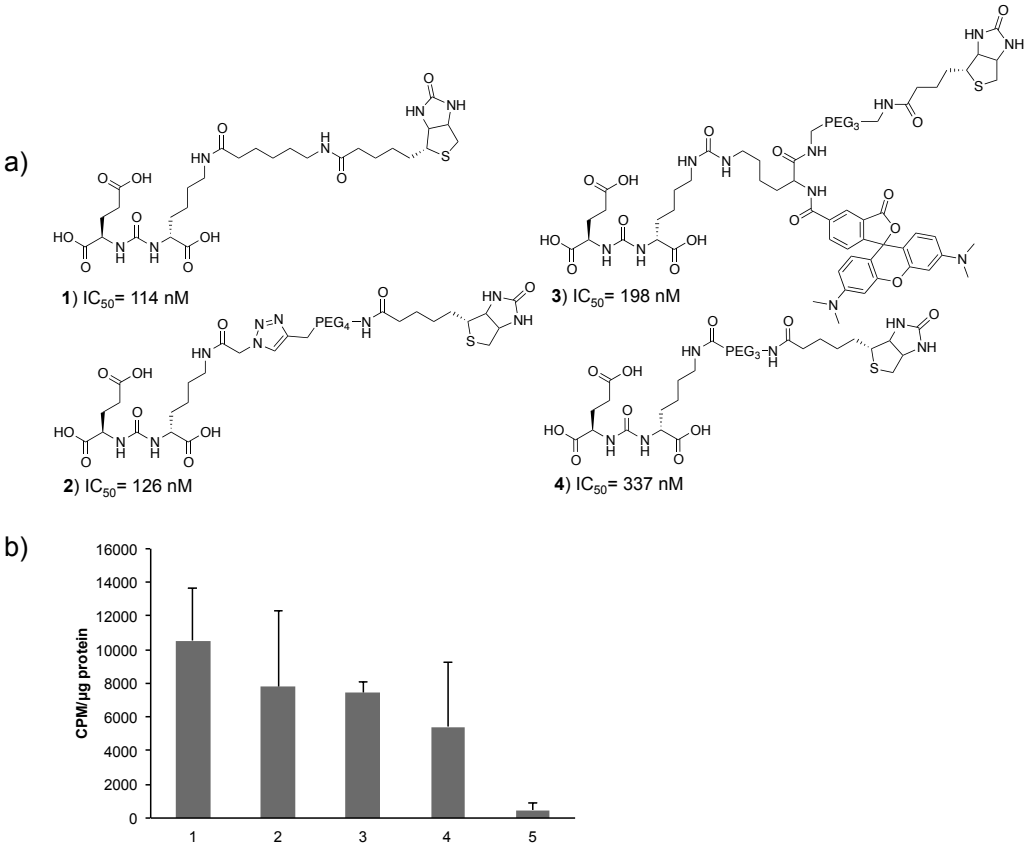

Figure 2.29 a) Structure of the PSMA inhibitors loaded on ^{99m}Tc-labeled MBs and their respective IC_{50} values. **b)** Bar graph representation of ^{99m}Tc-labeled MBs binding to PC3 (PSMA +ve) cells; data is represented as counts per min (CPM) normalized to the amount (µg) of protein found in each sample. (b1-b4) represents binding of PSMA-targeted ^{99m}Tc-labeled MBs loaded with one of the biotinylated PSMA inhibitors. While b5 represents the binding of non-targeted ^{99m}Tc-labeled MBs loaded with a biotinylated IgG isotype control antibody.

2.3.3 Assessment of the Parallel Tagging Strategy (PTS)

The PTS where two biotinylated derivatives are loaded on the MBs has limitations compared to the direct targeting strategy where one biotinylated derivative has both the signaling agent and targeting vector. One issue with PTS is the variety of MBs that can result after loading. PTS can result in a mixture of MBs loaded with just the targeting vector, unconjugated MBs, MBs loaded with both the targeting vector and signaling agent, and MBs loaded with just the signaling agent (Figure 2.30). Such outcome could result in reduced target binding and increased background. This may explain the similar biodistribution results observed of VEGFR2-targeted ^{99m}Tc-labeled MBs and non-targeted ^{99m}Tc-labeled MBs (Figure 2.21). Another major flaw in the PTS is that the amount of targeting vector per MBs is compromised by the amount of signaling agent present. This can drastically decrease the capability of the targeted ^{99m}Tc-labeled MBs to bind to the site of interest and overcome the strong shear rates occurring *in vivo*. While the PTS provides a simpler strategy for preparing multi-modal MBs, the drawbacks were not noted in the direct targeting strategy used by Gambhir and coworkers.[25] As a result a different derivatization strategy was explored going forward that involved the use of bioorthogonal chemistry to promote MBs functionalization and targeting.

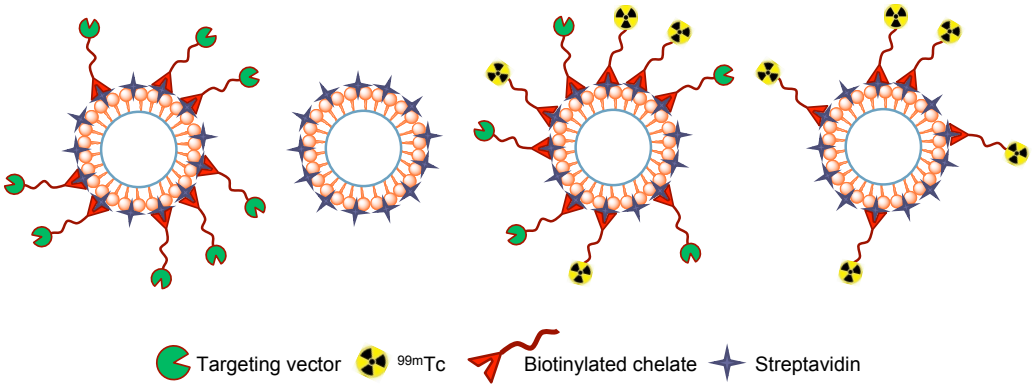

Figure 2.30 Representation of the possible mixture of MBs produced using the parallel tagging strategy (PTS).

2.4 References

[1] M. L. James, S. S. Gambhir, *Physiol. Rev.* **2012**, *92*, 897–965.

[2] Z. Liu, T. Lammers, J. Ehling, S. Fokong, J. Bornemann, F. Kiessling, J. Gätjens, *Biomaterials* **2011**, 32, 6155-6163.

[3] F. Yang, Y. Li, Z. Chen, Y. Zhang, J. Wu, N. Gu, *Biomaterials* **2009**, *30*, 3882–3890.

[4] P. Koczera, Z. Wu, S. Fokong, B. Theek, L. Appold, S. Jorge, D. Möckel, Z. Liu, A. Curaj, G. Storm, et al., *Drug Deliv. Transl. Res.* **2012**, *2*, 56–64.

[5] S. Fokong, B. Theek, Z. Wu, P. Koczera, L. Appold, S. Jorge, U. Resch-Genger, M. van Zandvoort, G. Storm, F. Kiessling, et al., *J. Control. Release* **2012**, *163*, 75–81.

[6] M. S. Tartis, D. E. Kruse, H. Zheng, H. Zhang, A. Kheirolomoom, J. Marik, K. W. Ferrara, *J. Control. Release* **2008**, *131*, 160–166.

[7] M. Palmowski, B. Morgenstern, P. Hauff, M. Reinhardt, J. Huppert, M. Maurer, E. C. Woenne, S. Doerk, G. Ladewig, J. W. Jenne, et al., *Invest. Radiol.* **2008**, *43*, 162–169.

[8] P. W. Causey, T. R. Besanger, P. Schaffer, J. F. Valliant, *Inorg. Chem.*

2008, *47*, 8213–8221.

[9] G. B. Saha, *Physics and Radiobiology of Nuclear Medicine*, 4th edition, T. A. Springer **2012**.

[10] S. Liu, *Adv. Drug Deliv. Rev.* **2008**, *60*, 1347–1370.

[11] M. Bartholomä, J. Valliant, K. P. Maresca, J. Babich, J. Zubieta, *Chem. Commun.* **2009**, 493–512.

[12] N. Lazarova, P. W. Causey, J. A. Lemon, S. K. Czorny, J. R. Forbes, A. Zlitni, A. Genady, F. S. Foster, J. F. Valliant, *Nucl. Med. Biol.* **2011**, *38*, 1111–1118.

[13] S. James, K. P. Maresca, D. G. Allis, J. F. Valliant, W. Eckelman, J. W. Babich, J. Zubieta, *Bioconjugate Chem.* **2006**, *17*, 579–589.

[14] D. S. Wilbur, D. K. Hamlin, R. L. Vessella, J. E. Stray, K. R. Buhler, P. S. Stayton, L. A. Klumb, P. M. Pathare, S. A. Weerawarna, *Bioconjugate Chem.* **1996**, *7*, 689–702.

[15] M. Pittelkow, R. Lewinsky, J. B. Christensen, *Synthesis* **2002**, 2195–2202.

[16] S. R. Banerjee, M. K. Levadala, N. Lazarova, L. Wei, J. F. Valliant, K. A. Stephenson, J. W. Babich, K. P. Maresca, J. Zubieta, *Inorg. Chem.* **2002**, *41*, 6417–6425.

[17] E. Kaiser, R. L. Colescott, C. D. Bossinger, P. I. Cook, *Anal. Biochem.* **1970**, *34*, 595–598.

[18] K. Upadhya, I. K. Khattak, B. Mullah, *Nucleosides Nucleotides Nucleic Acids* **2005**, *24*, 919–922.

[19] C. A. Sennoga, J. S. M. Yeh, J. Alter, E. Stride, P. Nihoyannopoulos, J. M. Seddon, D. O. Haskard, J. V. Hajnal, M.-X. Tang, R. J. Eckersley, *Ultrasound in Med. & Biol.* **2012**, *38*, 834–845.

[20] J. K. Willmann, A. M. Lutz, R. Paulmurugan, M. R. Patel, P. Chu, J. Rosenberg, S. S. Gambhir, *Radiology* **2008**, *248*, 936–944.

[21] D. J. Hicklin, L. M. Ellis, *J. Clin. Oncol.* **2005**, *23*, 1011–1027.

[22] J. K. Willmann, Z. Cheng, C. Davis, A. M. Lutz, M. L. Schipper, C. H. Nielsen, S. S. Gambhir, *Radiology* **2008**, *249*, 212–219.

[23] J. Hoppin, K. D. Orcutt, J. Y. Hesterman, M. D. Silva, D. Cheng, C. Lackas, M. Rusckowski, *J. Pharmacol. Exp. Ther.* **2011**, *337*, 350–358.

[24] L. Abou-Elkacem, S. V. Bachawal, J. K. Willmann, *Eur. J. Radiol.* **2015**, *84*, 1685–1693.

[25] J. K. Willmann, Z. Cheng, C. Davis, A. M. Lutz, M. L. Schipper, C. H. Nielsen, S. S. Gambhir, *Radiology* **2008**, *249*, 212–219.

[26] A. A. Elgamal, E. H. Holmes, S. L. Su, W. T. Tino, S. J. Simmons, M. Peterson, T. G. Greene, A. L. Boynton, G. P. Murphy, *Semin. Surg. Oncol.* **2000**, *18*, 10–16.

[27] A. Ghosh, W. D. W. Heston, *J. Cell. Biochem.* **2004**, *91*, 528–539.

[28] V. Yao, C. E. Berkman, J. K. Choi, D. S. O'Keefe, D. J. Bacich, *Prostate* **2010**, *70*, 305–316.

[29] P. F. Jackson, D. C. Cole, B. S. Slusher, S. L. Stetz, L. E. Ross, B. A. Donzanti, D. A. Trainor, *J. Med. Chem.* **1996**, *39*, 619–622.

[30] F. Nan, T. Bzdega, S. Pshenichkin, J. T. Wroblewski, B. Wroblewska, J. H. Neale, A. P. Kozikowski, *J. Med. Chem.* **2000**, *43*, 772–774.

[31] A. P. Kozikowski, F. Nan, P. Conti, J. Zhang, E. Ramadan, T. Bzdega, B. Wroblewska, J. H. Neale, S. Pshenichkin, J. T. Wroblewski, *J. Med. Chem.* **2001**, *44*, 298–301.

[32] Pingyu Ding, Marvin J Miller, Yi Chen, Paul Helquist, A. A Jayne Oliver, O. Wiest, *Org. Lett.* **2004**, *6*, 1805–1808.

[33] M. G. Pomper, J. L. Musachio, J. Zhang, U. Scheffel, Y. Zhou, J. Hilton, A. Maini, R. F. Dannals, D. F. Wong, A. P. Kozikowski, *Mol. Imaging* **2002**, *1*, 96–101.

[34] J. Zhou, J. H. Neale, M. G. Pomper, A. P. Kozikowski, *Nat. Rev. Drug*

Discov. **2005**, *4*, 1015–1026.

[35] S. A. Kularatne, Z. Zhou, J. Yang, C. B. Post, P. S. Low, *Mol. Pharm.* **2009**, *6*, 790–800.

[36] T. Liu, L. Y. Wu, M. Kazak, C. E. Berkman, *Prostate* **2008**, *68*, 955–964.

[37] K. P. Maresca, S. M. Hillier, F. J. Femia, D. Keith, C. Barone, J. L. Joyal, C. N. Zimmerman, A. P. Kozikowski, J. A. Barrett, W. C. Eckelman, et al., *J. Med. Chem.* **2009**, *52*, 347–357.

[38] Y. Chen, C. A. Foss, Y. Byun, S. Nimmagadda, M. Pullambhatla, J. J. Fox, M. Castanares, S. E. Lupold, J. W. Babich, R. C. Mease, et al., *J. Med. Chem.* **2008**, *51*, 7933–7943.

[39] C. Barinka, Y. Byun, C. L. Dusich, S. R. Banerjee, Y. Chen, M. Castanares, A. P. Kozikowski, R. C. Mease, M. G. Pomper, J. Lubkowski, *J. Med. Chem.* **2008**, *51*, 7737–7743.

[40] A. Darwish, M. Blacker, N. Janzen, S. M. Rathmann, S. Czorny, S. M. Hillier, J. L. Joyal, J. W. Babich, J. F. Valliant, *ACS Med. Chem. Lett.* **2012**, *3*, 313–316.

[41] J. R. Mesters, C. Barinka, W. Li, T. Tsukamoto, P. Majer, B. S. Slusher, J. Konvalinka, R. Hilgenfeld, *EMBO J.* **2006**, *25*, 1375–1384.

[42] V. Sanna, G. Pintus, P. Bandiera, R. Anedda, S. Punzoni, B. Sanna, V.

Migaleddu, S. Uzzau, M. Sechi, *Mol. Pharm.* **2011**, *8*, 748–757.

[43] A.R. Genady, N. Janzen, L. Banevicius, M. El-Gamal, M.E. El-Zaria, J.F. Valliant, *J. Med. Chem.* **2016**, *59*, 2660–2673.

3 Chapter 3 - Catching Bubbles: Targeting Ultrasound Microbubbles Using Bioorthogonal Inverse-Electron-Demand Diels–Alder Reactions

Aimen Zlitni, Nancy Janzen, F. Stuart Foster, and John F. Valliant

The following chapter was published in the journal of Angewandte Chemie International Edition, under the citation:

A. Zlitni, N. Janzen, F. S. Foster, J. F. Valliant, *Angew. Chem. Int. Ed. Engl.* **2014**, *53*, 6459–6463.

I was responsible for the development and execution of the majority of the work described in this paper including drafting the initial manuscript and experimental. Tumour inoculation and animal handling was done by Nancy Janzen. Ultrasound imaging acquisition was performed by Fred Roberts. Prof. Valliant was the PI of the lab and responsible for the overall manuscript and project.

3.1 Introduction

Ultrasound imaging remains one of the most extensively used medical imaging methods because of its high spatial and temporal sensitivity, low cost, portability and accessibility of equipment. Contrast-enhanced ultrasound using gas-filled microbubbles (MBs) has further enhanced the utility of ultrasound and created the opportunity to employ biomolecule-targeted derivatives for molecular imaging applications.[1] We describe here a new approach to ultrasound molecular imaging that employs the covalent and highly selective capture of functionalized MBs *in vitro* and *in vivo* through bioorthogonal inverse-electron-demand Diels–Alder reactions. While pretargeting methods for nanometer-sized materials, such as nanoparticles and liposomes, have been published recently,[2] the work reported herein is, to our knowledge, the first example of the bioorthogonal capture of micron-sized materials and the employment of pretargeting strategies for ultrasound molecular imaging.

Ultrasound contrast agents are generally comprised of an inert gas, such as a perfluorocarbon, surrounded by a lipid, synthetic polymer, or protein shell. The traditional approach to targeting MBs, which are typically 1–8 mm in diameter and therefore restricted to intravascular targets,[3] has been to link biomolecules with a high affinity for a specific protein to the outer shell through covalent bonds (e.g., amide bonds) or strong noncovalent interactions such as biotin–streptavidin binding.[4] These approaches, which have largely exploited antibody and peptide

vectors, have demonstrated the ability to selectively localize MBs to sites of angiogenesis, inflammation, and intravascular thrombus formation.[5]

Rather than using targeting vectors to localize conjugated prosthetic groups, new strategies for creating molecular imaging probes are being exploited that employ pretargeting and bioorthogonal coupling chemistry. Here, a targeting vector is administered first, allowing time for localization and clearance from nontarget organs, followed by a fluorescent or radiolabeled coupling partner that provides a readout for the molecular signal.[6] The inverse-electron-demand Diels–Alder reaction between tetrazines and trans-cyclooctene (TCO) is an example of a highly selective and rapid bioorthogonal coupling reaction that has been used successfully to prepare targeted nuclear and optical molecular imaging probes.[7] A comparable strategy for localizing MBs has not been reported. Such a method could offer a way to overcome obstacles to targeting ultrasound contrast agents whose large size and ability to bind only intravascular targets where blood flow rates and shear stress are high, make it particularly challenging to achieve and maintain good contrast in a time-frame that aligns with the limited *in vivo* stability of MBs.

To test the feasibility of capturing micron-sized bubbles, a novel tetrazine-tagged MB (MB_{Tz}) was developed, and its reactivity towards cells treated with a TCO-conjugated anti-vascular endothelial growth factor receptor 2 (VEGFR2) antibody evaluated (Figure 3.1). VEGFR2 is overexpressed on tumor cells and

upon activation triggers multiple signaling pathways that contribute to angiogenesis.[8] The choice of target also allows the use of anti-VEGFR2-tagged MBs (MB_V), which were developed by Rychak, Foster, and co-workers for evaluation in preclinical models,[9] to validate the tetrazine–TCO capture methodology.

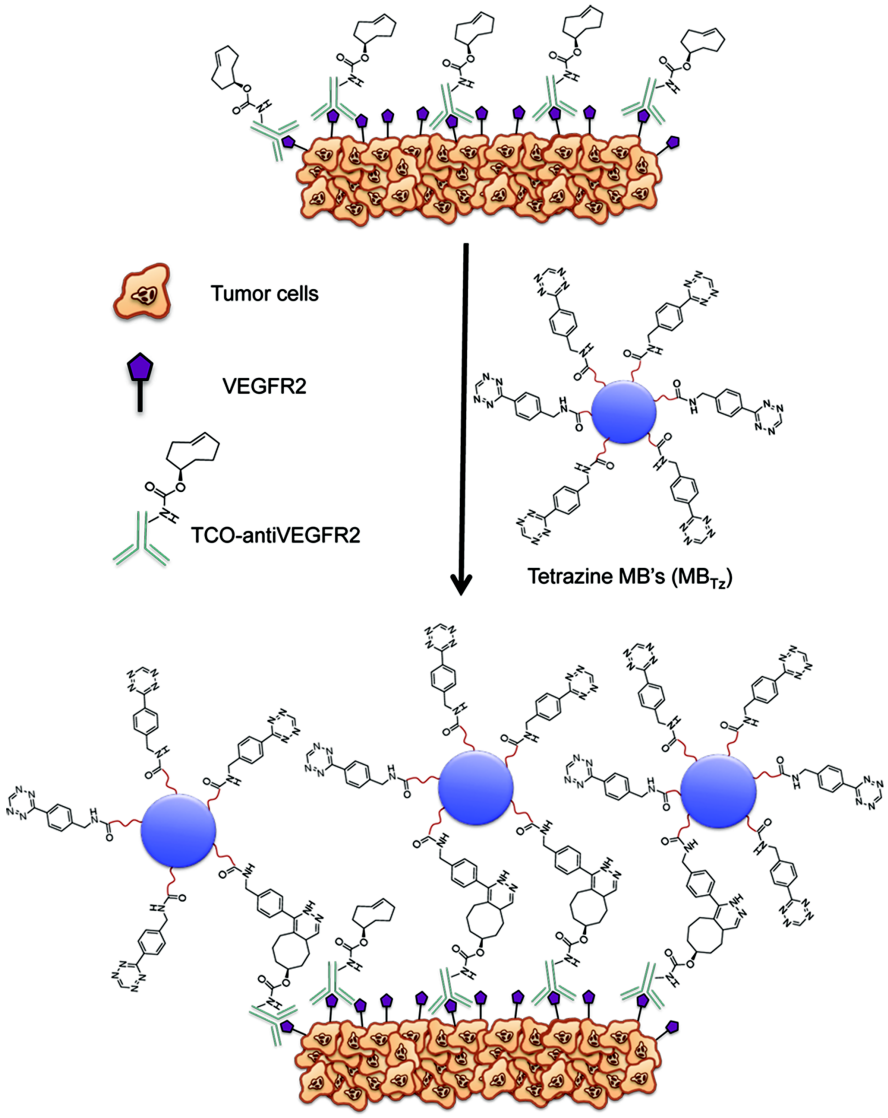

Figure 3.1 Localizing MBs to tumor cells through pretargeting and bioorthogonal chemistry between tetrazine-functionalized microbubbles (MB_{Tz}) and an intravascular target (VEGFR2) labeled with a TCO-modified antibody.

3.2 Results and discussion

Tetrazine-functionalized bubbles were prepared using commercially available streptavidin-coated MBs (MicroMarker™ target-ready contrast agents,

VisualSonics) and a biotinylated tetrazine. The biotin–tetrazine derivative **5** was synthesized from biotin in four high-yielding steps (Scheme 3.1). The desired product was ultimately obtained by coupling commercially available 4-(1,2,4,5-tetrazin-3-yl)phenyl)methanamine hydrochloride with 6-biotinamidohexanoic tetrafluorophenyl (TFP) ester (**4**) at room temperature. After semipreparative HPLC, compound **5** was isolated in 75% yield and the product was stable in the freezer for more than six months. The TCO-conjugated antibody (TCO–anti-VEGFR2) was prepared by combining an excess (20 equiv) of commercially available (E)-cyclooct-4-enyl-2,5-dioxopyr- rolidin-1-yl carbonate (TCO-NHS) with antiVEGFR2 (eBioscience) at 4 °C overnight at pH 9.0–9.5. After purification using a 30 kDa centrifugal filter (Amicon Ultra-0.5) MALDI-TOF MS showed an average of 2.8 TCO groups per antibody in the product.

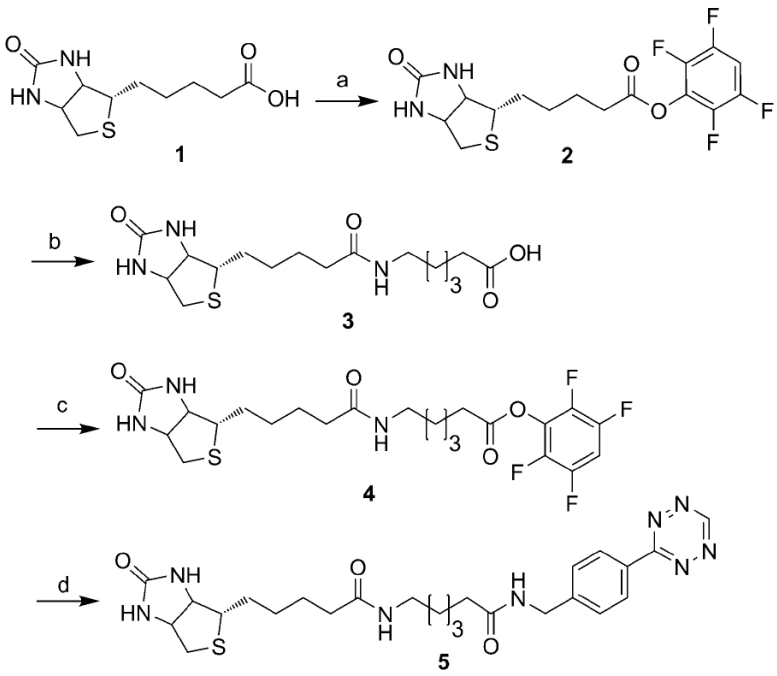

Scheme 3.1 Synthesis of biotin–tetrazine (**5**). Reagents and conditions: **a)** 2,3,5,6-tetrafluorophenyl trifluoroacetate, DMF, TEA, 30 min, 95%; **b)** 6-amino-hexanoic acid, DMF, TEA, 75 °C, 12 h, 91%; **c)** 2,3,5,6- tetrafluorophenyl trifluoroacetate, DMF, DMSO, 80 °C, 1 h, 96%; **d)** 4- (1,2,4,5-tetrazin-3-yl)phenyl)methanamine hydrochloride, DMF, TEA, 1 h, 75%. DMF = dimethylformamide, TEA = triethylamine, DMSO = di-methylsulfoxide.

The derivatized bubbles MB_{Tz} and MB_V were prepared by adding **5** or biotinylated antiVEGFR2, respectively, to freshly reconstituted streptavidin-coated MBs. Isolation of the bubbles from the biotin-containing reagents was accomplished by treating the solution with streptavidin-coated magnetic beads (New England Biolabs), which bound residual tetrazine and antibody, followed by simple magnetic separation.[10] We found this approach more convenient than centrifugation and washing, as it minimizes the amount of direct handling of the

MBs. The bubbles have 7600 molecules of streptavidin μm^{-2}, giving approximately 6000 molecules μm^{-2} of surface area.[9] Prior to working with MB_{Tz}, the ability of **5** to bind to VEGFR2-positive H520 cells tagged with TCO–antiVEGFR2 was evaluated *in vitro* in direct comparison to a commercially available biotinylated antiVEGFR2 antibody (biotin–antiVEGFR2). Compound **5** was added to H520 cells that had been incubated with TCO–antiVEGFR2, and the extent of tetrazine–TCO conjugation was determined by adding a FITC-labeled anti-biotin antibody (FITC–antiBiotin) and measuring the arising fluorescence in cell lysates. As a control, FITC–antiBiotin was added to H520 cells that had been incubated with a comparable amount of biotin–antiVEGFR2. The tetrazine–TCO construct (Figure 3.2a) showed effectively identical intensity to direct tagging with the biotinylated antibody (Figure 3.2b). The binding of **5** and FITC–antiBiotin to H520 cells in the absence of any VEGFR2 antibodies was measured and showed significantly lower intensity (Figure 3.2c), indicating minimal nonspecific binding.

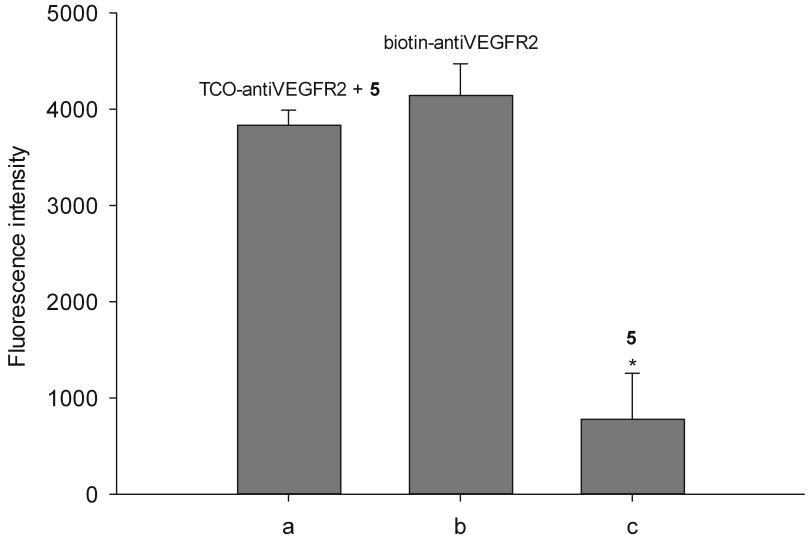

Figure 3.2 Fluorescence intensity of VEGFR2(+) H520 cell lysates obtained following treatment of cells with **a)** TCO–antiVEGFR2, 5, then FITC–antiBiotin; **b)** commercially available biotin–antiVEGFR2 and FITC–antiBiotin; and **c)** 5 followed by FITC–antiBiotin. The fluorescence intensity in (a) and (b) were comparable and statistically different (one-way ANOVA) than the control (c). *p = 0.001.

To evaluate the effectiveness of the tetrazine-TCO capture strategy, MBs were evaluated initially *in vitro* under flow conditions (as opposed to simply in culture) similar to those found in tumor capillaries [11] by using a parallel-plate flow chamber system (Glycotech, Rockville, Md.). VEGFR2-expressing cells (H520) and cells lacking VEGFR2 (A431) were incubated with TCO–antiVEGFR2 30 minutes prior to the assay. Using a syringe pump, cells were washed with PBS for 2 minutes to remove any unbound antibody, followed by either functionalized or unmodified MBs for 4 minutes at a 100 s^{-1} shear rate to

mimic flow conditions *in vivo*. To differentiate MBs bound through nonspecific binding interactions from those retained through the TCO–tetrazine reaction, cells were subsequently washed with PBS for 2 minutes at a 10-fold increased (1000 s^{-1}) shear rate. Optical microscopy was used to visualize the plates and videos were taken during the flow assay and static images for analysis acquired after the final washing step was completed (see the Supporting Information).

Qualitatively, the tetrazine-modified MBs concentrated to a significant extent on H520 cells (VEGFR2(+)) that had been pre-incubated with TCO–antiVEGFR2. The video of the process shows substantially higher retention of MBs over time compared to cells that had not been treated with the antibody (see the Supporting Information). A relatively small amount of MBs bound nonspecifically to the flow chamber during the dynamic component of all assays, which were removed after the final washing step. Images taken subsequently exhibited significant retention of MB_{Tz} (Figure 3.3a) on TCO-antiVEGFR2-tagged H520 cells compared to experiments run with untreated cells (Figure 3.3b). Repeating the study using VEGFR2-negative A431 cells similarly showed little MB_{Tz} retention (Figure 3.3c). To compare with more traditional targeting strategies, the VEGFR2-targeted MBs were evaluated under identical conditions and showed com- parable binding to the capture strategy (Figure 3.3d). It was conceivable that TCO-antiVEGFR2 promote nonspecific binding of the MBs to the cells. To test this hypothesis, unmodified MBs as a control (MB_C) were

exposed to H520 cells tagged with TCO-antiVEGFR2 and negligible MB retention was observed (Figure 3.3e).

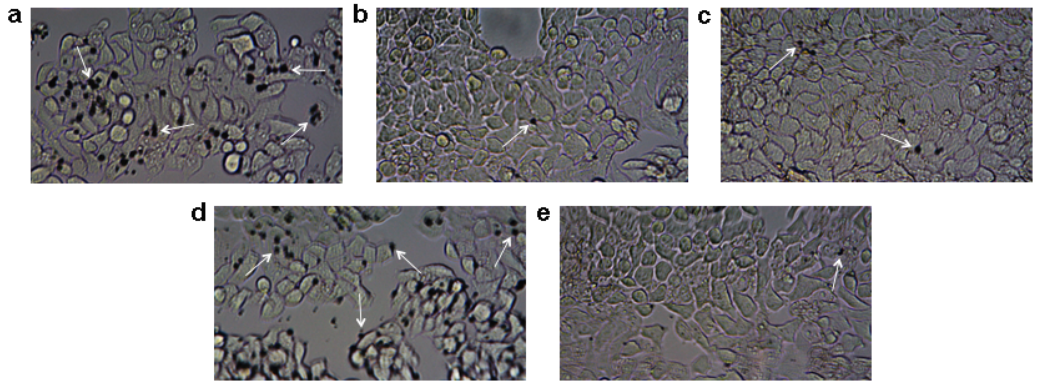

Figure 3.3 Bright-field microscopy images (20 ×) showing binding of: **a)** MB_{Tz} to TCO–antiVEGFR2-tagged H520 cells (VEGFR2(+)); **b)** MB_{Tz} to H520 cells with no antibody; **c)** MB_{Tz} to TCO–antiVEGFR2-tagged A431 cells (VEGFR2(−)); **d)** MB_V to H520 cells; and **e)** MB_C to TCO-antiVEGFR2-tagged H520 cells. The MBs appear as black spheres with select examples highlighted by the white arrows. MB_{Tz}= tetrazine- functionalized MBs; MB_V= MBs functionalized with biotinylated antiVEGFR2;[9] MB_C= unmodified MBs (MicroMarker™ target-ready contrast agents, VisualSonics).

A semiquantitative analysis was performed by comparing the area covered by the MBs (black spheres) in each image to the area covered by the cells determined using an open-source image processing package.[12] Prior to the analysis, the concentration of the solutions and the sizes of the MBs were determined using a Coulter counter to ensure comparable test conditions. The MB_C, MB_{Tz}, and MB_V concentrations were similar at 5.7×10^6, 6.9×10^6, and 9.4

$\times 10^6$ MBs mL^{-1}, respectively, as were the average sizes, at 2.62 ± 0.73, 3.11 ± 0.85, and 2.68 ± 0.73 μm, respectively. MB_{Tz} binding to TCO–antiVEGFR2-tagged H520 cells (Figure 3.4a) was more than one order of magnitude higher than its binding to unlabeled cells (Figure 3.4c). Minimal binding of MB_C to TCO–antiVEGFR2-tagged H520 cells (Figure 3.4e) and MB_{Tz} to VEGFR2-negative TCO–antiVEGFR2-tagged A431 cells (Figure 3.4d) was observed, which is consistent with the images shown in Figure 3.3. The tetrazine system exhibited similar binding to the previously reported antiVEGFR2-targeted MBs (MB_V; Figure 3.4b), thus indicating that the pretargeting strategy has at least the equivalent ability to localize contrast agent to the VEGFR2 target.

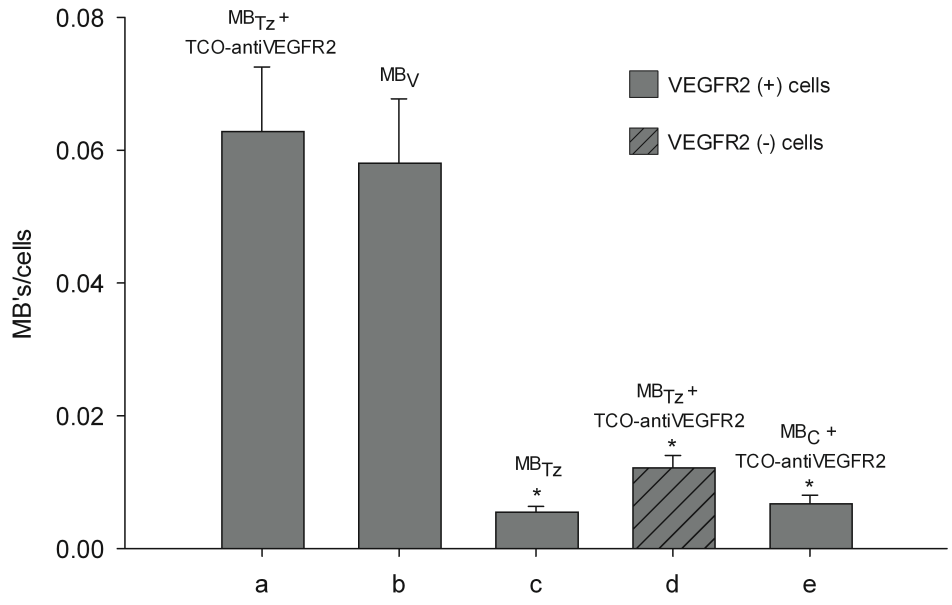

Figure 3.4 Analysis of the number of MBs bound per cell based on relative area from the flow chamber adhesion assay following washing. For H520

(VEGFR2(+)) cells, near-equivalent binding was seen for a) the MB_{Tz}-TCO-antiVEGFR2 system, and b) antiVEGFR2-targeted MBs (MB_V). Binding of MB_{Tz} to TCO-antiVEGFR2-tagged H520 cells was significantly higher than with c) unlabeled cells and d) TCO-antiVEGFR2-tagged A431 (VEGFR2(−)) cells ($p = 0.001$). e) Unmodified MBs (MB_C) showed minimal binding to TCO-antiVEGFR2-tagged H520 cells. MB_{Tz}= tetrazine-functionalized MBs; MB_V= MBs functionalized with biotinylated antiVEGFR2;[9] MB_C= unmodified MBs (MicroMarker™ target-ready contrast agents, VisualSonics). Area measurements were determined using FIJI software.[12] *statistically significant difference ($p= 0.001$) relative to (a) (analyzed using one-way ANOVA).

Having demonstrated successful capture on cells under flow conditions similar to those found in tumor capillaries, a preliminary study in animal models was undertaken. Ultrasound imaging was performed using CD1 nu/nu mice bearing SKOV-3 (VEGFR2(+)) human adenocarcinoma tumors. TCO-antiVEGFR2 was administered 24 hours prior to injecting the MBs to allow adequate time for accumulation in the tumor. For consistency with how antiVEGFR2-targeted MBs (MB_V) were previously assessed, a destruction replenishment sequence[9] was employed four minutes after injection and the differential enhancement of the signal was measured using VevoCQ quantification software (VisualSonics). Regions of interest were based on the vascularity of the tumors determined from the initial distribution of the MBs following injection. All animal experiments were performed following procedures approved by the Animal Research Ethics Board (AREB) at McMaster University.

The images showed high retention of MB_{Tz} in vascularized

regions of the SKOV-3 tumors. Even in cases in which the tumors were poorly vascularized (Figure 3.5a), providing less surface area for capture, contrast enhancement was significant. Contrast was greater than for images obtained in animals that were not administered the antibody (Figure 3.5b) and in A431 (VEGFR2(−)) tumor models despite administration of the antibody (Figure 3.5c). Localization of the known biotinylated antiVEGFR2-modified MBs was also apparent (Figure 3.5d). Interestingly, signals obtained using MB_C on prelabeled SKOV-3 tumors (Figure 3.5e) was higher than expected but three times lower than with MB_{Tz}, suggesting some amount of nonspecific binding.

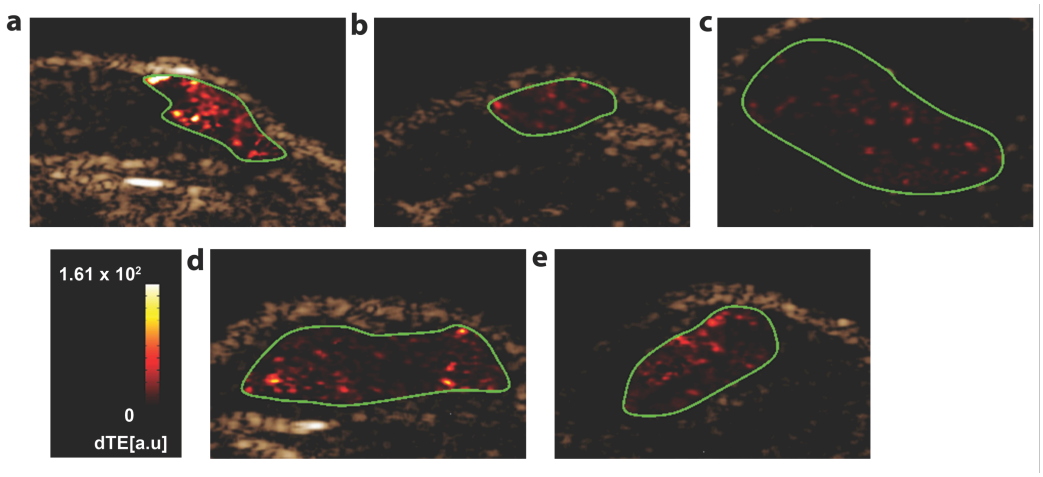

Figure 3.5 Transverse color-coded parametric nonlinear contrast mode ultrasound images acquired 4 min after intravenous administration of MB_{Tz} to: **a)** SKOV-3 human adenocarcinoma murine tumor model (VEGFR2(+)) pre-administered with TCO-antiVEGFR2; and **b)** the same model without antibody; **c)** A431 human epidermoid carcinoma tumor (VEGFR2(−)) pre-administered with TCO-antiVEGFR2. Images of SKOV-3 murine tumor models following administration of **d)** MB_V; and **e)** MB_C with pre-administered TCO-antiVEGFR2. Regions of

interest were based on the vascularity of the tumors determined from the initial distribution of the MBs following injection. dTE= differential targeted enhancement.

It is important to note that biotin–streptavidin-based linker systems are not suitable for clinical use because of the immunogenic response caused by multiple injections of streptavidin.[3] However, for clinical applications one can envision preparing a new generation of ultrasound contrast agents that contain tetrazines covalently bound to the shells of MBs in a more biocompatible manner. As ultrasound has emerged as an important preclinical imaging tool, we believe the approach reported here is a general and convenient means of noninvasively evaluating binding of new antibodies to intravascular targets in preclinical models. Bioconjugation of TCO to antibodies or other comparable vectors is simple and reproducible and the associated reagents are commercially available. The corresponding ultrasound images can be obtained using a single type of tetrazine-labeled MB, such as the one reported, eliminating the complexities and variability (i.e., changes in bubble size and extent of functionalization) associated with preparing different antibody-MB derivatives. The approach should therefore expedite the evaluation of different MB-targeting strategies and help accelerate the development of novel ultrasound molecular imaging probes. It also reduces barriers to use ultrasound imaging in order to evaluate new antibody-based therapeutics because targeted MB development and optimization is greatly simplified.

3.3 Conclusion

In conclusion, we provided the first evidence that capturing MBs *in vitro* and *in vivo* is feasible using bioorthogonal coupling reactions. Taken together, the flow chamber assays and imaging data demonstrate that the localization of MBs is related to the presence of the target (VEGFR2) and the tetrazine-TCO reaction, and not simply the formation of antibody-labeled bubbles in situ. The comparable binding observed for the bubble-capture strategy and the known VEGFR2-targeted MBs (MB_V) further validates that the reported approach can be used to effectively visualize a specific target in both cells under a flow format and animal models. Further use and study of MB-capture strategies appears warranted, with current efforts focusing on evaluating different pretargeting constructs, linker lengths, dosing levels, and timing to further enhance image contrast and create new classes of molecularly targeted ultrasound contrast agents.

3.4 Acknowledgements

Financial support for this research was provided by the Natural Sciences and Engineering Research Council (NSERC) of Canada, The Ontario Ministry of Research and Innovation, the Ontario Research Fund (grant no. RE03-051), and the Canadian Cancer Society (grant no. 2011-700896). The authors also acknowledge Frederick R. Roberts and VisualSonics for their technical support.

3.5 References

[1] O. F. Kaneko, J. K. Willmann, *Quant. Imaging Med. Surg.* **2012**, 2, 87–97.

[2] a) S. B. Lee, H. L. Kim, H.-J. Jeong, S. T. Lim, M.-H. Sohn, D. W. Kim, *Angew. Chem.* **2013**, 125, 10743–10746; *Angew. Chem. Int. Ed.* **2013**, 52, 10549–10552; b) F. Emmetiere, C. Irwin, N.T. Viola-Villegas, V. Longo S. M. Cheal, P. Zanzonico, N. Pillar- setty, W. A. Weber, J. S. Lewis, T. Reiner, *Bioconjugate Chem.* **2013**, 24, 1784–1789 ; c) J. Rho, J. Chung, H. Im, M. Liong, H. Shao, C. M. Castro, R. Weissleder, H. Lee, *ACS Nano* **2013**, 7, 11227–11233; d) S.S. Agasti, R.H. Kohler, M. Liong, V.M. Peterson, H. Lee, R. Weissleder, *Small* **2013**, 9, 222–227; e) G. Budin, H. J. Chung, H. Lee, R. Weissleder, *Angew. Chem.* **2012**, 124, 7872–7875; *Angew. Chem. Int. Ed.* **2012**, 51, 7752–7755; f) C. Tassa, M. Liong, S. Hilderbrand, J. E. Sandler, T. Reiner, E. J. Keliher, R. Weissleder, S. Y. Shaw, *Lab Chip* **2012**, 12, 3103–3110; g) V. M. Peterson, C. M. Castro, H. Lee, R. Weissleder, *ACS Nano* **2012**, 6, 3506–3513; h) M. Liong, M. Fernandez-Suarez, D. Issadore, C. Min, C. Tassa, T. Reiner, S. M. Fortune, M. Toner, H. Lee, R. Weissleder, *Bioconjugate Chem.* **2011**, 22, 2390–2394; i) J. B. Haun, N. K. Devaraj, B. S. Marinelli, H. Lee, R. Weissleder, *ACS Nano* **2011**, 5, 3204–3213; j) J. B. Haun, N. K. Devaraj, S. A. Hilderbrand, H. Lee, R. Weissleder, *Nat. Nanotechnol.* **2010**, 5, 660–665.

[3] S. Hernot, A. L. Klibanov, *Adv. Drug Delivery Rev.* **2008**, 60, 1153–1166.

[4] A. L. Klibanov, *Med. Biol. Eng. Comput.* **2009**, 47, 875–882.

[5] N. Deshpande, A. Needles, J. K. Willmann, *Clin. Radiol.* **2010**, 65, 567–581.

[6] a) I. Nikic´, T. Plass, O. Schraidt, J. Szyman´ski, J. A. G. Briggs, C. Schultz, E. A. Lemke, *Angew. Chem.* **2014**, 126, 2278–2282; *Angew. Chem. Int. Ed.* **2014**, 53, 2245–2249; b) J.C.T. Carlson, L. G. Meimetis, S. A. Hilderbrand, R. Weissleder, *Angew. Chem.* **2013**, 125, 7055–7058; *Angew. Chem. Int. Ed.* **2013**, 52, 6917–6920; c) S.M. vandenBosch, R. Rossin, P. Renart Verkerk, W. ten Hoeve, H. M. Janssen, J. Lub, M. S. Robillard, *Nucl. Med. Biol.* **2013**, 40, 415–423; d) D. S. Liu, A. Tangpeerachaikul, R. Selvaraj, M. T. Taylor, J. M. Fox, A. Y. Ting, *J. Am. Chem. Soc.* **2012**, 134, 792–795; e) N. K. Devaraj, R. Weissleder, *Acc. Chem. Res.* **2011**, 44, 816–827; f) B. M. Zeglis, P. Mohindra, G. I. Weissmann, V. Divilov, S. A. Hilderbrand, R. Weissleder, J.S. Lewis, *Bioconjugate Chem.* **2011**, 22, 2048– 2059; g) N. K. Devaraj, S. S. Hilderbrand, R. R. Upadhyay, R. R. Mazitschek, R. R. Weissleder, *Angew. Chem.* **2010**, 122, 2931–2934; *Angew. Chem. Int. Ed.* **2010**, 49, 2869–2872; h) J. C. Jewett, C. R. Bertozzi, *Chem. Soc. Rev.* **2010**, 39, 1272–1279; i) N. K. Devaraj, R. Upadhyay, J. B. Haun, S. A. Hilderbrand, R. Weissleder, *Angew. Chem.* **2009**, 121, 714–7150; *Angew. Chem. Int. Ed.* **2009**, 48, 7013–7016; j) E. M. Sletten, C. R. Bertozzi, *Angew. Chem.* **2009**, 121, 7108–7133; *Angew. Chem. Int. Ed.* **2009**, 48, 6974–6998.

[7] a) R. Rossin, T. Läppchen, S. M. van den Bosch, R. Laforest, M. S. Robillard,

J. *Nucl. Med.* **2013**, 54, 1989–1995; b) B. M. Zeglis, K. K. Sevak, T. Reiner, P. Mohindra, S. D. Carlin, P. Zanzonico, R. Weissleder, J. S. Lewis, *J. Nucl. Med.* **2013**, 54, 1389–1396; c) R. Rossin, S. M. van den Bosch, W. Ten Hoeve, M. Carvelli, R. M. Versteegen, J. Lub, M. S. Robillard, *Bioconjugate Chem.* **2013**, 24, 1210–1217; d) Z. Wu, S. Liu, M. Hassink, I. Nair, R. Park, L. Li, I. Todorov, J. M. Fox, Z. Li, J. E. Shively, P. S. Conti, F. Kandeel, *J. Nucl. Med.* **2013**, 54, 244–251; e) E. J. Keliher, T. Reiner, G. M. Thurber, R. Upadhyay, R. Weissleder, *ChemistryOpen* **2012**, 1, 177–183 ; f) N. K. Devaraj, G. M. Thurber, E. J. Keliher, B. Marinelli, R. Weissleder, *Proc. Natl. Acad. Sci. USA* **2012**, 109, 4762–4767; g) R. Selvaraj, S. Liu, M. Hassink, C. Huang, L. Yap, R. Park, J. M. Fox, Z. Li, P. S. Conti, *Bioorg. Med. Chem. Lett.* **2011**, 21, 5011–5014; h) R. Rossin, P. R. Verkerk, S. M. van den Bosch, R. C. M. Vulders, I. Verel, J. Lub, M. S. Robillard, *Angew. Chem.* **2010**, 122, 3447–3450; *Angew. Chem. Int. Ed.* **2010**, 49, 3375–3378.

[8] D. J. Hicklin, L. M. Ellis, *J. Clin. Oncol.* **2005**, 23, 1011–1027.

[9] a) J. J. Rychak, J. Graba, C. White, A. M. Y. Cheung, B. Mistry, J. R. Linder, R. S. Kerbel, F. S. Foster, *Mol. Imaging* **2007**, 6, 289–296; b) J. K. Willmann, R. Paulmurugan, K. Chen, O. Gheysens, M. Rodriguez-Pocel, A. M. Lutz, I. Y. Chen, X. Chen, S. S. Gambhir, *Radiology* **2008**, 246, 508–518.

[10] N. Lazarova, P. W. Causey, J. A. Lemon, S. K. Czorny, J. R. Forbes, A. Zlitni, A. Genady, F. S. Foster, J. F. Valliant, *Nucl. Med. Biol.* **2011**, 38, 1111–

1118.

[11] R. K. Jain, *Cancer Res.* **1988**, 48, 2641–2658.

[12] J.Schindelin et *al.*, *Nat. Methods* **2012**, 9, 676–682.

3.6 Supporting information

Further supporting information can be found online at http://dx.doi.org/10.1002/anie.201402473. For this thesis, the experimental and supporting information can be found in Appendix I.

4 Chapter 4: The Development and Evaluation of Prostate Specific Membrane Antigen Targeted Ultrasound Microbubbles using Bioorthogonal Chemistry

The following chapter is formatted in a manuscript that is ready for submission to the journal of Cancer Research. I was responsible for the development and execution of the majority of the experimental work and drafting the manuscript and experimental. Tumour inoculation was done by Nancy Janzen. Ultrasound imaging acquisition was performed by Melissa Yin. Prof. Valliant was the PI of the lab and responsible for the overall manuscript and project.

4.1 Abstract

A non-invasive, sensitive imaging tool that detects aggressive prostate cancer would greatly aid diagnosis and reduce the frequency of unnecessary surgical procedures. Ultrasound imaging using microbubbles (MBs) targeted to established biomarkers that are overexpressed on prostate tumors, such as prostate specific membrane antigen (PSMA), have the potential to address this issue. To this end, the development and evaluation of PSMA-targeted MBs constructed using a bioorthogonal chemical ligation strategy between tetrazine (Tz) and trans-cyclooctene (TCO) functionalized targeting molecules is reported. Specifically streptavidin-labeled MBs were coated with a biotinylated tetrazine (MB_{Tz}) and targeted to PSMA-expressing cells using a PSMA-specific antibody functionalized with TCO (TCO-anti-PSMA). Biomarker targeting was achieved *in vitro* by either a pre-targeting approach, wherein PSMA expressing cells were first incubated with TCO-anti-PSMA followed by MB_{Tz}, or by a direct targeting strategy, wherein the TCO-anti-PSMA was first linked to MB_{Tz} before exposure to PSMA expressing cells. An *in vitro* flow chamber binding assay showed 2.8 and 5 fold increased binding of MB_{Tz} to PSMA expressing cells by the pre-targeting and direct targeting strategies respectively, compared to binding of MB_{Tz} alone. The direct targeting strategy was evaluated *in vivo* in human xenograft tumor model in mice. Using a TCO-anti-PSMA specific to human PSMA only, a 1.6 fold increased ultrasound signal compared to non-targeted MBs was observed, whereas using a TCO-anti-PSMA that binds both mouse and

human PSMA resulted in 5.9 fold increase signal. These results identify an effective and convenient approach to prepare PSMA-targeted MBs, demonstrating the feasibility of creating a molecularly targeted ultrasound contrast agent for detecting prostate cancer.

4.2 Introduction

Prostate cancer (PCa) is the second leading cause of cancer-related deaths in men (1). It is estimated that in 2015 more than 220,000 men in the USA and 24,000 in Canada were diagnosed with PCa, which would account for 26% of all new cancer cases in men (1,2). When detected early, the 5-year survival rate is around 99%, but survival drops dramatically once the cancer has spread beyond the prostate (3). The gold standard for PCa diagnosis is trans-rectal ultrasound (TRUS)-guided biopsies in patients with elevated serum levels of prostate specific antigen (PSA) and/or an abnormal finding upon digital rectal exam. Unfortunately, TRUS biopsies have a high rate of false-negative results thereby missing the presence of PCa in many patients, and there are frequent requirements for repeat biopsy procedures (4-7). Therefore, there is a need develop a more sensitive, accurate, and non-invasive imaging technique to help localize PCa biomarkers within the prostate and to assess the size and aggressiveness of prostate tumors, both during diagnosis and following the initiation of therapy (8). Such a technique could help support active surveillance strategies and reduce the need for repeat biopsies, while significantly enhancing the survival and quality of life of PCa patients (8).

One approach to enhancing PCa detection is to use imaging agents targeted against prostate specific membrane antigen (PSMA). PSMA is a transmembrane glycoprotein that is expressed at low levels in normal prostate,

liver, kidney and brain tissue, but is expressed in much higher levels in PCa tumors (9-15). Furthermore, high PSMA expression in PCa correlates with pathological stage and tumor grade, and was demonstrated as an independent predictor of biochemical recurrence (16,17). PSMA has been an attractive target for optical, magnetic resonance and nuclear imaging methods, indicating the high potential of PSMA imaging in PCa (18-24).

A microbubble based contrast agent that targets PSMA would provide the opportunity to use ultrasound (US) to visualize specific molecular markers found on PCa tumors (25,26). PSMA is highly expressed on the endothelial cells in the microvasculature of PCa tumors, making it a suitable target for US imaging using targeted microbubbles (MBs) that are generally restricted to targets within the vasculature due to their size (27). A PSMA-targeted US method could be used for detecting PCa lesions and for biopsy guidance, providing an alternative to more costly MRI-based biopsy guidance (28).

Sanna and coworkers prepared polymer-based MBs covalently attached to a small-molecule inhibitor of PSMA (29). The MBs showed specific binding to PSMA-expressing ($PSMA^+$) cells in *vitro*, however no evaluation of this agent under dynamic flow conditions or in preclinical animal models has been reported. Wang and coworkers prepared nano-scale US contrast bubbles (NBs) coated with streptavidin and loaded with a biotinylated derivative of an anti-PSMA antibody (30). *In vitro* and *in vivo* studies showed a modest but statistically significant

difference in the binding of the PSMA targeted NBs, where the ratio of the US signal obtained from targeted compared to non-targeted NBs was less than 1.20. These researchers also targeted the same NBs using a biotinylated derivative of an anti-PSMA nanobody, which showed similar binding compared to the anti-PSMA antibody (31).

Here we utilize the highly efficient bioorthogonal chemical reaction between tetrazine (Tz) and trans-cyclooctene (TCO) to target MBs to PSMA. This methodology has been used successfully *in vivo* to target MBs to the angiogenesis marker vascular endothelial growth factor receptor 2 (32), and provides two options to target the MBs to the tissue site of interest. The first is a direct targeting strategy, which involves reacting a target-specific, TCO-labeled antibody (TCO-anti-PSMA) with Tz-functionalized MBs (MB_{Tz}) creating the antibody-linked MBs (Fig. 4.1a), prior to *in vivo* administration and US imaging (Fig. 4.1b). The second option is a pre-targeting strategy, in which the TCO-anti-PSMA is injected first, to allow binding to sites of target antigen overexpression and to clear from non-target organs. This is followed by injection of MB_{Tz} that will selectively react with target-bound TCO-anti-PSMA *in vivo* (Fig. 4.1b). We report here the successful development and evaluation of both approaches and demonstrate US imaging of PSMA expressing tumors in a mouse model.

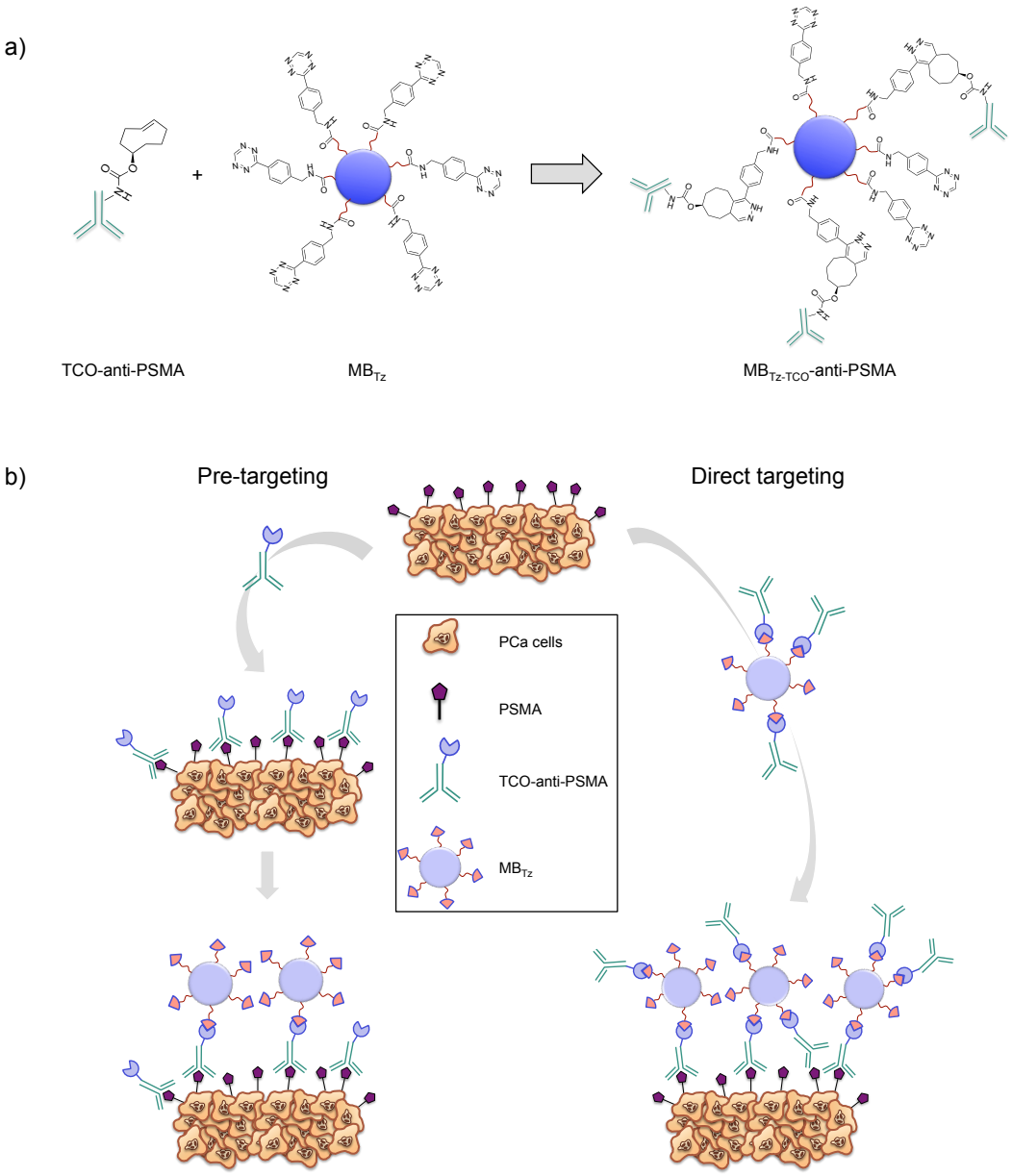

Figure 4.1 a) Schematic illustrating the cyclo-addition product obtained when reacting MB_{Tz} with TCO-conjugated PSMA antibody (TCO-anti-PSMA) producing anti-PSMA-loaded MBs ($MB_{Tz\text{-}TCO}$-anti-PSMA). **b)** Schematic representation of the two strategies used to target MB_{Tz} to PSMA-expressing prostate cancer cells (PCa cells). **Right:** MB_{Tz} is loaded with TCO-anti-PSMA ($MB_{Tz\text{-}TCO}$-anti-PSMA) first before injection and binding to PSMA-expressing

PCa cells (direct targeting). **Left:** TCO-anti-PSMA is injected first and allowed to bind to PSMA-expressing PCa cells and clear non-targeted tissue before injecting MB_{Tz} (pre-targeting).

4.3 Materials and Methods

4.3.1 General materials and instruments

Microbubbles (MBs) were obtained (8.4×10^8 MBs/vial) from a MicroMarker™, Target-Ready Contrast Agent Kit (VisualSonics Inc., Toronto, ON). Streptavidin coated magnetic beads (New England BioLabs, Whitby, ON) and MACSiMAG™ separator magnet (Miltenyi Biotec, Auburn, CA) were used during the purification of MBs. Conjugated-antibodies were analyzed by mass spectrometry on a MALDI Bruker Ultraflextreme Spectrometer. MBs size and concentration were determined using Z2 Coulter counter (Beckman Coulter, Fullerton CA). Syringe pump used in the flow chamber assay was a PhD 2000 syringe pump (Harvard Apparatus, Holliston, MA). Western blot images were generated using a STORM 840 imaging system (GMI Ltd., Ramsey, MN).

4.3.2 Preparation of TCO-modified antibodies.

J591 is an anti-PSMA monoclonal antibody that binds the extracellular domain of human PSMA (33) and was provided by Dr. Neil Bander (Department of Urology, Cornell University). The TCO-modified J591 was prepared as previously described (32). Briefly, the pH of a solution of J591 antibody (500 µL, 250 µg, 1.67 nmol, in PBS) was adjusted to 9 by adding 3 µL of 1 M Na_2CO_3 (aq).

(E)-cyclooct-4-enyl-2,5-dioxopyrrolidin-1-yl carbonate (TCO-NHS) was then added (17.8 µg, 66.8 nmol, 40 eq) in 9 µL DMSO. The solution was left on a shaker overnight at 4 °C. The desired product (TCO-J591) was isolated from excess TCO using an Amicon Ultra-0.5 Centrifugal filter (30 kDa) and washed with PBS three times. MALDI-TOF MS analysis of the antibody before and after conjugation to TCO showed an average of 1.2 TCO groups per antibody, using a MALDI Bruker Ultraflextreme Spectrometer (Supplementary Data, Fig. S 4.1). A polyclonal rabbit IgG antibody (ARP44691_p050; Aviva Systems Biology, San Diego, CA) that reacts with both mouse PSMA and human PSMA was labeled with TCO by the same method, and is referred to herein as TCO-anti-hu/muAb.

4.3.3 Synthesis of Biotin-Tz

N-(4-(1,2,4,5-tetrazin-3-yl)benzyl)-6-(5-((4*S*)-2-oxohexahydro-1*H*-thieno[3,4-*d*]imidazol-4-yl)pentanamido)hexanamide (biotin-Tz) was synthesized as described previously (32). The structure of biotin-Tz is shown in Supplementary Data (Fig. S 4.2).

4.3.4 Preparation of tetrazine-functionalized microbubbles (MB_{Tz})

Streptavidin-coated MBs (MicroMarker™; VisualSonics Inc.) were reconstituted in 500 µL sterile saline (0.9% NaCl), according to the manufacturer's instructions. To prepare MB_{Tz}, biotin-Tz (70 µg, 1.35×10^{-4} mmol) in 50 µL of saline:MeOH (1:1 v/v) was added dropwise to the reconstituted MBs. After 45 min, 200 µL from the bottom of the vial was removed

carefully with minimal agitation and was discarded. Then, a 200 µL suspension of streptavidin-coated magnetic beads (New England BioLabs) were added and the solution set aside for 20 min. Thereafter, 200 µL of the solution was removed carefully and discarded, and the remaining mixture was placed beside a MACSiMAG™ magnet (Miltenyi Biotec) to remove any residual magnetic bead-bound biotin-Tz, that sediment in the vial. Saline (200 µL) was then added to MBs and the solution transferred to another vial. MBs size and concentration were determined using Z2 Coulter counter (Beckman Coulter).

4.3.5 Preparation of anti-PSMA antibody coated MBs

Anti-PSMA coated MBs were prepared by combining MB_{Tz} with either TCO-J591 antibody or TCO-anti-hu/muPSMA. Briefly MB_{Tz} solution (50 µL (3×10^7 MBs) for *in vitro*, 120 µL (7×10^7 MBs) for *in vivo* studies) was mixed with either TCO-labeled antibody (20 µL, 10 µg for *in vitro*, 50 µL, 25µg for *in vivo* studies). The Tz-TCO reaction was allowed to proceed for 20 min at room temperature. The resulting $MB_{Tz\text{-}TCO}$-J591 and $MB_{Tz\text{-}TCO}$-anti-hu/muPSMA constructs were used immediately for *in vitro* binding studies or *in vivo* imaging studies.

4.3.6 Cells and culture methods

PC-3 cells transfected with human PSMA were provided by (Molecular Insight Pharmaceuticals, Inc., Cambridge, MA). PC-3 cells were cultured in F12-K media supplemented with 10% FBS, 1% penicillin-streptomycin and 0.1%

geneticin. LNCaP cells were purchased from ATCC (CRL-1740), and cultured in RPMI-1640 Medium supplemented with 10% FBS and 1% penicillin-streptomycin. The cell lines were maintained at 37 °C under 5% CO_2.

4.3.7 Flow Chamber Cell Adhesion Assay.

The flow assay was performed as previously described (32). Briefly, 8×10^5 of PC-3 cells were plated separately, in 30 mm Corning tissue culture dishes, 2 days prior to running the assay. In the pre-targeting strategy and associated controls, cells were incubated first with TCO-J591 (30 μg/mL) for 30 min. The setup of the parallel-plate flow chamber (Glycotech, Rockville, MD) is shown in the Supplementary data (Fig. S 4.3). Using the PhD 2000 syringe pump, cells were first rinsed with 1 mL of PBS, and then 1 mL of MBs solution at a shear rate of 100 sec^{-1} (flow rate = 0.164 mL/min) was applied. Thereafter, the plate was rinsed with 2 mL of PBS at a shear rate of 1000 sec^{-1}. Binding of MBs was visualized using a Celestron PentaView LCD Digital Brightfield S4 Microscope with 20× objective. Images were recorded and the extent of binding assessed by comparing the area covered by MBs to the total area covered by cells in each image, using image analysis (FIJI) software (32,34).

4.3.8 Animal models and procedures

All animal studies were approved by the Animal Research Ethics Board at McMaster University. Mice were maintained with 12 h light/dark cycles and given food and water *ad libitum*. LNCaP cells derived from lymph node

metastases of human prostate carcinoma were purchased from ATCC (CRL-1740). NCr nude male mice (4 to 5 week old) were purchased (Taconic Labs, Germantown, NY) and were injected with 2.0×10^6 LNCaP cells in 100 μL Matrigel/DPBS (1:1; VWR-Canlab, Mississauga, ON and Invitrogen, Burlington, ON) subcutaneously in the right flank. For tumor extraction, mice were sacrificed by cervical dislocation directly after imaging, and then the tumors were excised, rinsed with PBS and frozen in liquid N_2. Frozen tumors were stored at -80 °C until processed for cell lysate preparation.

4.3.9 Tumor lysate preparation

Each frozen tumor was thawed and put into lysis buffer containing 1% IGEPAL CA-630 (I3021; Sigma-Aldrich, Oakville, ON), 20mM Tris pH 8.0 (154563; Sigma-Aldrich), 137mM NaCl (S6191; Sigma-Aldrich), 10% glycerol (5350-1; Caledon Laboratories), 2mM EDTA (E5134; Sigma-Aldrich) and Protease Inhibitor cocktail (PIC003; Bioshop Canada, Burlington, ON). Each tumor was subsequently homogenized using VWR PowerMax AHS 200 homogenizer (5 × 75 mL troemner) and lysate collected after centrifugation (2000 × g, 5 min) and washing three times with PBS. Protein concentration was determined using a Pierce® BCA Protein Assay Kit (ThermoFisher Scientific, Ottawa, ON).

4.3.10 Western blot analysis of cell lysates

Using immunoblotting, PSMA protein expression by transfected $PSMA^+$

PC-3 and $PSMA^+$ LNCaP cells was assessed and compared to and $PSMA^-$ PC-3 cells. 10 μg of protein from each cell lysate were loaded on 10% Mini-PROTEAN TGX Precast gels and fractionated by SDS-PAGE. After electro-transferring the protein extracts to polyvinylidene difluoride (PVDF) membrane, the membrane was incubated with PSM antibody (E-18), a goat polyclonal antibody (sc-10269; Santa Cruz Biotechnology, Dallas, TX), specific for mouse and human PSMA, in a 1:250 dilution overnight at 4 °C. Following washing, the membrane was incubated with AP-Bovine anti-goat IgG antibody (sc-2351; Santa Cruz Biotechnology) in a 1:2000 dilution for 1 h at room temperature. The membrane was finally washed and incubated with a chemiluminescent reagent (ECF substrate, GE RPN5785) for 5 min and imaged using a STORM 840 imaging system (GMI Ltd., Charlotte, NC).

4.3.11 Western Blot analysis of tumor lysates

PSMA expression by LNCaP tumors used in imaging studies was assessed by immunoblotting. Tumor lysates were loaded on 10% Mini-PROTEAN TGX precast gels and fractionated by SDS-PAGE. Protein extracts were electro-transferred to PVDF membrane. The PVDF membrane was incubated with PSM (E-18) goat anti-PSMA antibody (sc-10269; Santa Cruz Biotechnology) in a 1:250 dilution, and anti-β-Actin (13E5) rabbit monoclonal antibody (4970; Cell Signaling Technology, Beverly, MA) in a 1:2000 dilution overnight at 4 °C. The membrane was then washed and incubated with AP-Bovine anti-goat IgG (sc-

2351; Santa Cruz Biotechnology) plus AP-Goat anti-rabbit IgG (H+L) (111055045, Jackson ImmunoResearch) in a 1:2000 dilution for 1 h at room temperature. Finally, the membrane was washed and incubated with a chemiluminescent reagent (ECF substrate, GE RPN5785) for 5 min and imaged using a STORM 840 imaging system (GMI Ltd.). Image bands for PSMA and ß-actin were quantified using ImageQuant TL software (GE Healthcare Life Sciences).

4.3.12 Ultrasound (US) Imaging and Analysis

Using a Vevo 2100 imaging system (VisualSonics) and a 20 MHz high-frequency solid-state transducer (MS-250; VisualSonics), LNCaP tumor-bearing mice were imaged using the non-linear contrast mode. Animals were kept under anesthesia using isoflurane (4% initiation, 2% maintenance) in medical air, during the imaging session. MBs injections (approximately 5-6 × 10^7 MBs in 70 µL) were performed via the tail vein, using a syringe pump at a 600 µL/min injection rate. First, each mouse was injected with MB_{Tz} and imaged. Following a time to allow the MBs to clear, MB_{Tz} complexed with anti-PSMA antibody was injected. After each injection, MBs were allowed to circulate for 4 min before initiating a disruption replenishment sequence (35). Typically 200 frames were acquired before a continuous high power disruption pulse (100% transmit power) was applied within the imaging window. Freely circulating MBs were allowed to refill the tumor for 5 sec before acquiring another set of frames. A 15 min break and a

3D disruption sequence took place after each imaging session, to allow complete clearance of previously injected MBs.

The differential targeted enhancement (dTE) signal was measured using the advanced contrast quantification software analysis tool (VevoCQ™, VisualSonics). Regions of interest were determined based on the distribution of the MBs in the tumor (the vascular region) and was kept constant when evaluating the different MBs in the same animal. The average intensity over 200 frames acquired 5 sec after disruption was subtracted from the average intensity over 200 frames acquired before disruption. Representative images are parametric images overlaid on the nonlinear contrast mode US images.

4.4 Results and Discussion

4.4.1 Preparation of PSMA-targeted MBs

MB_{Tz} were prepared by adding *N*-(4-(1,2,4,5-tetrazin-3-yl)benzyl)-6-(5-((4*S*)-2-oxohexahydro-1*H*-thieno[3,4-*d*]imidazol-4-yl)-pentanamido)hexanamide (biotin-Tz , Supplementary Data, Fig. S 4.2) to commercially available streptavidin coated MBs, as described previously (32). The first TCO-labeled anti-PSMA antibody (TCO-J591) was prepared by combining the anti-human PSMA monoclonal J591 with (E)-cyclooct-4-enyl-2,5-dioxopyrrolidin-1-yl carbonate (TCO-NHS), at pH 9-9.5 and 4 °C overnight. The number of TCO moieties per antibody was 1.2, as determined by MALDI-TOF MS (Supplementary Data, Fig. S 4.1). J591 binds to the extracellular domain of

human PSMA (33) and was shown to be a highly effective tool for targeting various radio isotopes and nanomaterials to PSMA (12,36-41). A polyclonal rabbit IgG anti-PSMA antibody that reacts with both human and mouse PSMA was also labeled successfully with TCO (TCO-anti-hu/muPSMA), using the same method.

4.4.2 *In vitro* evaluation of direct and pre-targeting of MBs to $PSMA^+$ cells

The ability to target MBs to $PSMA^+$ cells *in vitro* was assessed in a flow chamber adhesion assay (Supplementary Data, Fig. S 4.3). The flow chamber system is designed to provide a more realistic test environment for evaluating the ability of targeted MBs to bind receptors in the dynamic fluid environment of tumor microvasculature, rather than the typical static culture conditions (42). Although the $PSMA^+$ LNCaP cells were chosen for *in vivo* targeting studies, they have low adhesive properties in culture, and therefore were not suitable for use in the flow chamber system. Instead, the more adherent PC-3 cells that were $PSMA^+$ (human PSMA gene-transfected) or $PSMA^-$ (non-transfected) were used. Western blot analysis of the two PC-3 cell lines showed PSMA protein expression in the $PSMA^+$ PC-3 cells at levels comparable to LNCaP cells, and no expression by $PSMA^-$ PC-3 cells (Supplementary data, Fig. S 4.4).

Both the pre-targeting and direct targeting approaches were evaluated using the *in vitro* flow chamber assay. For pre-targeting, TCO-J591 was incubated with the cells for 30 min, before introducing the MB_{Tz}. For direct targeting, TCO-

J591 was incubated with MB_{Tz} for 20 min, creating the targeted MBs ($MB_{Tz\text{-}TCO}$-J591) that were subsequently used in the flow assay. For all experiments, test cells were rinsed with PBS before the start of the flow chamber assay. With pre-targeting, cells were washed with PBS after incubation with TCO-J591. Both MB_{Tz} and the $MB_{Tz\text{-}TCO}$-J591 conjugates were added at the same flow rate (0.164 mL/min). After each experiment, bright-field microscopy images were collected and analyzed using FIJI software, as previously reported (32).

Both qualitative inspection of microscopy images (Fig. 4.2) and semi-quantitative analysis indicated significantly lower binding of MB_{Tz} to $PSMA^+$ PC-3 cells (Fig. 4.3) using the pre-targeting approach compared to the direct targeting approach. However, binding of MB_{Tz} by pre-targeting was still 2.8 times higher than controls, in which non-conjugated MBs (no Tz) or $PSMA^-$ PC-3 cells were used (Fig. 4.3). For the direct targeting approach, the results showed greater than 5-fold higher binding of $MB_{Tz\text{-}TCO}$-J591 to $PSMA^+$ PC-3 cells, compared to controls. The reduced MB_{Tz} binding with pre-targeting is likely due to the internalization of J591, which has been previously reported (43). Because of the difference observed in *in vitro* experiments only the direct targeting strategy was further evaluated *in vivo*, using a mouse xenograft tumor model.

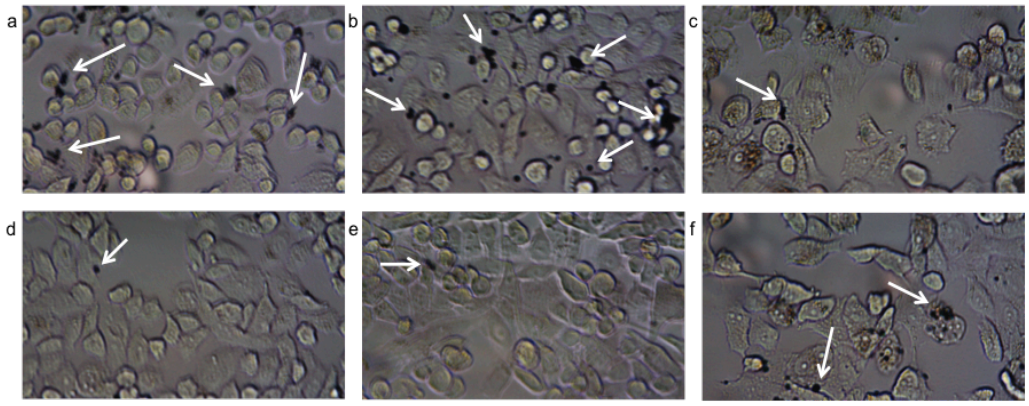

Figure 4.2 Bright-field microscopy images (20×) showing binding of: **a)** MB_{Tz} to TCO-J591 to $PSMA^+$ PC-3 cells pre-treated with TCO-J591; **b)** MB_{Tz} complexed with TCO-J591 ($MB_{Tz\text{-}TCO}$-J591) to $PSMA^+$ PC-3 cells; **c)** MB_{Tz} to $PSMA^+$ PC-3 cells with no antibody; **d)** MB_{Tz} to $PSMA^-$ PC-3 cells pre-treated with TCO-J591; **e)** $MB_{Tz\text{-}TCO}$-J591 to $PSMA^-$ PC-3 cells and **f)** Control MBs (MB_C) with no Tz to $PSMA^+$ PC-3 cells pre-treated with TCO-J591. The MBs appear as black spheres (select examples shown with white arrows).

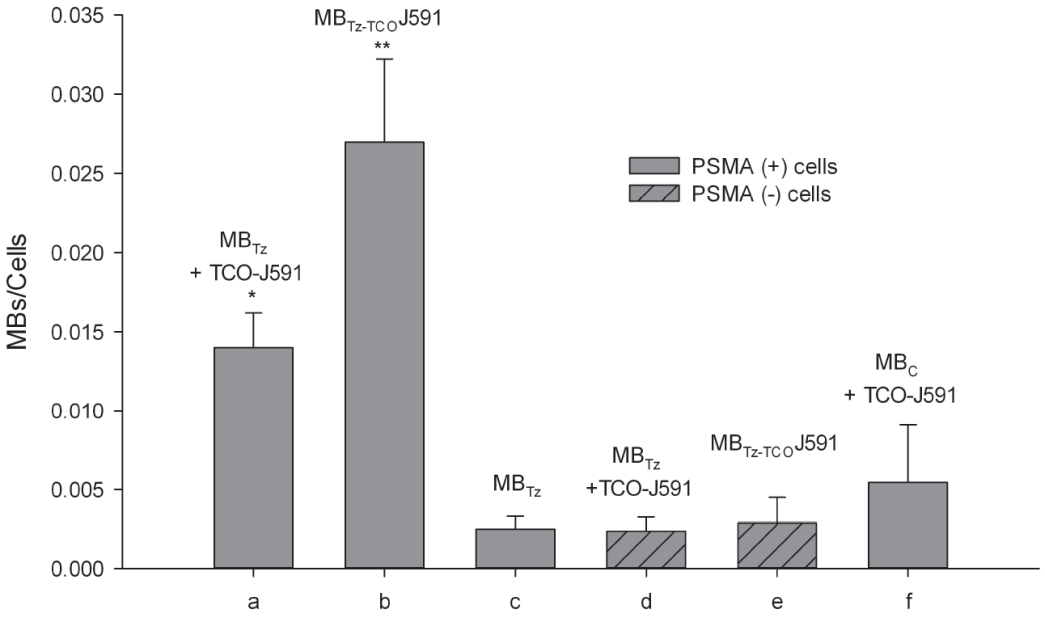

Figure 4.3 Semi-quantitative analysis of the number of MBs bound per cell (n= 3 replicates) from the flow chamber adhesion assay. Binding of the direct targeting $MB_{Tz\text{-}TCO}$-J591 construct was greater than 8-fold higher to $PSMA^+$ PC-3 cells (b) compared to binding of MB_{Tz} alone (c) or $MB_{Tz\text{-}TCO}$-J591 binding to $PSMA^-$ cells (e); ** statistically significant ($p < 0.001$). There was lower binding of MB_{Tz} to PSMA+ cells when TCO-J591 was pre-targeted (a) compared to direct targeting (b). However, the amount of MB_{Tz} bound with pre-targeting (a) was significantly higher than controls using $PSMA^-$ cells with pre-targeting (d) or control MB_C (no Tz) with pre-targeting (f); * statistically significant ($p < 0.001$). The MB_C control (f) was not significantly different ($p > 0.05$) from other controls (c,d,e). Statistical analysis was performed using one-way ANOVA.

4.4.3 *In vivo* targeting of MBs to PSMA-expressing LNCaP xenografts tumors

LNCaP cells were used in a well-established PSMA tumor xenograft model (44) using NCr nu/nu mice (45). Following each US imaging study, PSMA

expression in the isolated tumor was verified by western blotting of tumor lysates (Supplementary Data, Fig. S 4.5). The amounts of PSMA expressed by all tumors used for US imaging showed little variability, when normalized to β-actin expression (Supplementary Data, Fig. S 4.6). As a background control in all studies, non-targeted MB_{Tz} were allowed to accumulate in the tumors for 4 min, before a disruption replenishment sequence was conducted (32). After 15 min, a 3D disruption sequence was applied to insure there were no residual MBs prior to injecting the PSMA targeting contrast agent.

Targeting studies were performed using either the $MB_{Tz\text{-}TCO}$-J591 construct (anti-human PSMA) or the $MB_{Tz\text{-}TCO}$-anti-hu/muPSMA construct (anti-human and mouse PSMA). The latter was chosen to assess the extent of contribution of mouse PSMA, because mouse endothelial cells are present within the xenograft microvasculature (46). For the targeted MBs, imaging was performed using the same plane of view as that for control non-targeted MB_{Tz}. The parametric US images showed qualitatively higher signal enhancement when either the $MB_{Tz\text{-}TCO}$-J591 or $MB_{Tz\text{-}TCO}$-anti-hu/muPSMA direct targeting constructs were used, as compared to non-targeted MB_{Tz} (Fig. 4.4). When the signal enhancement was quantified, the mean of the ratio of signals for targeted to non-targeted MB_{Tz} was 1.6 for the $MB_{Tz\text{-}TCO}$-J591 construct and 5.9 for the $MB_{Tz\text{-}TCO}$-anti-hu/muPSMA construct (Fig. 4.5). Thus, both direct targeting constructs demonstrated enhanced accumulation of PSMA-targeted MBs in the tumor, with

the dual-specificity antibody construct ($MB_{Tz\text{-}TCO}$-anti-hu/muPSMA) producing approximately 3.6 fold more signal. The difference could be due to the variation in affinity for human PSMA between the two antibodies or the presence of mouse PSMA expressed on the endothelial cells of the tumor microvasculature (46). It is worth noting that our result using the differential target enhancement method indicates a much larger signal enhancement for targeted MBs compared to the previous reports using PSMA-targeted bubbles, where a statistically significant increase in signal was observed when measuring only the US peak enhancement (30,31) which would include both target bound and circulating MBs.

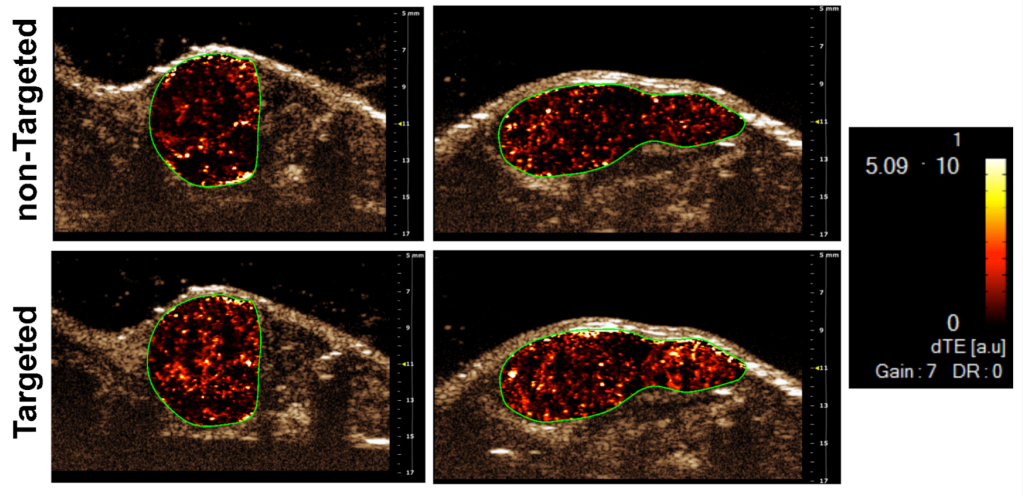

Figure 4.4 Representative US images showing targeted tumor localization of the anti-human PSMA ($MB_{Tz\text{-}TCO}$-J591) construct (left bottom) and the anti-human and mouse PSMA ($MB_{Tz\text{-}TCO}$-anti-hu/muPSMA) construct (right bottom). Images were first acquired 4 min after intravenous administration of non-targeted MB_{Tz} (top left and right), and then after the targeted constructs (bottom left and right). The images using the targeted constructs show qualitatively higher US signal, compared to the signal from non-targeted MB_{Tz}. Each pair of images (top/bottom)

are from the same mouse and same field of view. Images are transverse color-coded parametric images overlaid on a nonlinear contrast mode ultrasound image, with whole LNCaP xenograft tumor (green outline) in the field of view. dTE= differential targeted enhancement. Complete image data for tumors from n= 3 mice targeted with either construct are found in Supplementary Data (Figs. S 4.7, S 4.8).

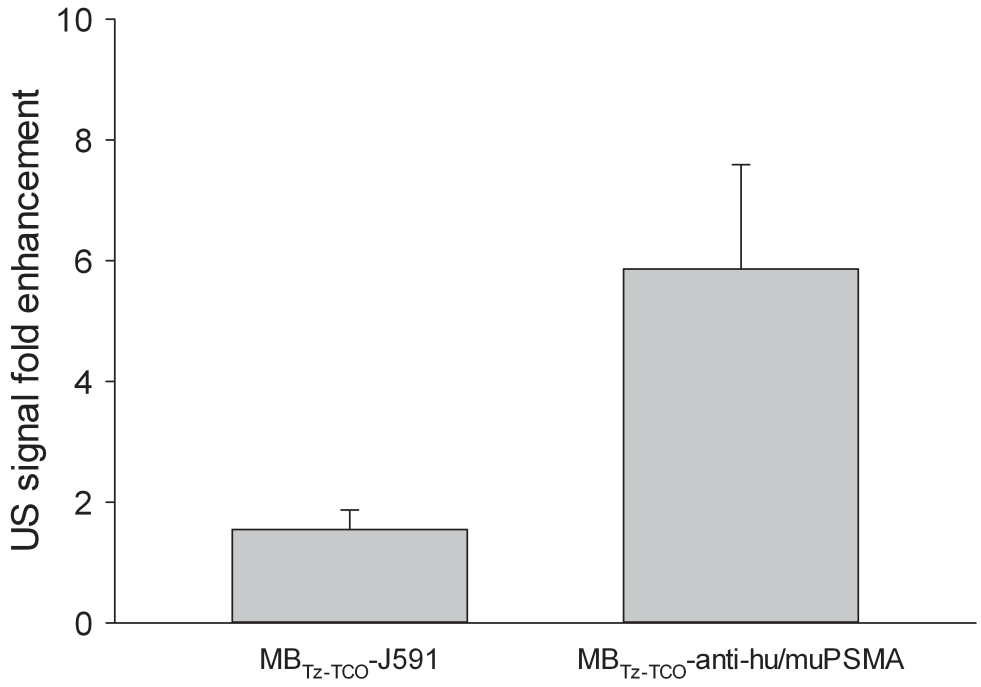

Figure 4.5 Comparison of the US signal enhancement obtained by direct targeting of PSMA$^+$ LNCaP tumors, using either the anti-human PSMA antibody construct (MB$_{Tz-TCO}$-J591) or the anti-human and mouse PSMA antibody construct (MB$_{Tz-TCO}$-anti-hu/muPSMA). Data are average ratio of US signals (n= 3, with SEM), for the targeting construct:control (MB$_{Tz}$ alone).

4.5 Conclusion

The presented work shows the effectiveness of the TCO-Tz bioorthogonal

chemistry for constructing targeted MBs using antibodies. This strategy provided an easy to use, standard MB platform (MB_{Tz}) that is amenable for translation of any antibody-based targeting to any endothelial cell surface biomarker. More important to the imaging of PCa, the TCO-Tz chemistry provided a high yielding, reproducible and readily adapted production of PSMA-targeted MBs. Studies are ongoing to create a human compatible MB_{Tz} that when combined with a humanized anti-human PSMA antibody (e.g. J591) will provide PSMA-targeted MBs suitable for clinical trials.

4.6 Acknowledgments:

The authors acknowledge the contributions of Dr. Denis Snider who provided scientific proofreading and editing in preparation of this manuscript as well as Molecular Insight Pharmaceuticals for providing the transfected PC-3 cells and Dr. Neil Bander (Department of Urology, Cornell University) for providing the humanized J591 anti-PSMA antibody.

4.7 References

1. Siegel RL, Miller KD, Jemal A. Cancer statistics, 2015. CA Cancer J Clin. 2015;65:5–29.

2. Canadian Cancer Statistics. Canadian Cancer Society's Advisory Committee on Cancer Statistics. 2015. Available from: http://www.cancer.ca/en/cancer-information/cancer-101/canadian-cancer-statistics-publication/?region=on

3. Sheets S. National Cancer Institute, SEER Facts Sheets: Prostate Cancer 2015. Available from: http://seer.cancer.gov/statfacts/html/prost.html

4. Heidenreich A, Bellmunt J, Bolla M, Joniau S, Mason M, Matveev V, et al. EAU Guidelines on Prostate Cancer. Part 1: Screening, Diagnosis, and Treatment of Clinically Localised Disease. Eur Urol 2011;59:61–71.

5. Norberg M, Egevad L, Holmberg L, Sparén P, Norlén BJ, Busch C. The sextant protocol for ultrasound-guided core biopsies of the prostate underestimates the presence of cancer. Urology 1997;50:562–6.

6. Roethke M, Anastasiadis AG, Lichy M, Werner M, Wagner P, Kruck S, et al. MRI-guided prostate biopsy detects clinically significant cancer: analysis of a cohort of 100 patients after previous negative TRUS biopsy. World J Urol 2012;30:213–8.

7. Pallwein L, Mitterberger M, Pelzer A, Bartsch G, Strasser H, Pinggera GM, et al. Ultrasound of prostate cancer: recent advances. Eur Radiol 2008;18:707–15.

8. Eder M, Eisenhut M, Babich J, Haberkorn U. PSMA as a target for radiolabelled small molecules. Eur J Nucl Med Mol Imaging 2013;40:819–23.

9. Ghosh A, Heston WDW. Tumor target prostate specific membrane antigen (PSMA) and its regulation in prostate cancer. J Cell Biochem 2004;91:528–39.

10. Su SL, Huang IP, Fair WR, Powell CT, Heston WD. Alternatively spliced variants of prostate-specific membrane antigen RNA: ratio of expression as a potential measurement of progression. Clin Cancer Res 1995;55:1441–3.

11. Sweat SD, Pacelli A, Murphy GP, Bostwick DG. Prostate-specific membrane antigen expression is greatest in prostate adenocarcinoma and lymph node metastases. Urology 1998;52:637–40.

12. Holland JP, Divilov V, Bander NH, Smith-Jones PM, Larson SM, Lewis JS. 89Zr-DFO-J591 for immunoPET of prostate-specific membrane antigen expression in vivo. J Nucl Med 2010;51:1293–300.

13. Kinoshita Y, Kuratsukuri K, Landas S, Imaida K, Rovito PM, Wang CY,

et al. Expression of prostate-specific membrane antigen in normal and malignant human tissues. World J Surg 2006;30:628–36.

14. Israeli RS, Powell CT, Corr JG, Fair WR, Heston WD. Expression of the prostate-specific membrane antigen. Clin Cancer Res 1994;54:1807–11.

15. Sokoloff RL, Norton KC, Gasior CL, Marker KM, Grauer LS. A dual-monoclonal sandwich assay for prostate-specific membrane antigen: Levels in tissues, seminal fluid and urine. Prostate 2000;43:150–7.

16. Ross JS, Sheehan CE, Fisher HAG, Kaufman RP, Kaur P, Gray K, et al. Correlation of primary tumor prostate-specific membrane antigen expression with disease recurrence in prostate cancer. Clin Cancer Res 2003;9:6357–62.

17. Perner S, Hofer MD, Kim R, Shah RB, Li H, Möller P, et al. Prostate-specific membrane antigen expression as a predictor of prostate cancer progression. Hum Pathol 2007;38:696–701.

18. Castanares MA, Mukherjee A, Chowdhury WH, Liu M, Chen Y, Mease RC, et al. Evaluation of prostate-specific membrane antigen as an imaging reporter. J Nucl Med 2014;55:805–11.

19. Banerjee RS, Pullambhatla M, Foss CA, Nimmagadda S, Ferdani R, Anderson CJ, et al. 64Cu-Labeled Inhibitors of Prostate-Specific

Membrane Antigen for PET Imaging of Prostate Cancer. J Med Chem 2014;57:2657–69.

20. Osborne JR, Akhtar NH, Vallabhajosula S, Anand A, Deh K, Tagawa ST. Prostate-specific membrane antigen-based imaging. Urol Oncol: Semin Orig Invest 2013;31:144–54.

21. Foss CA, Mease RC, Fan H, Wang Y, Ravert HT, Dannals RF, et al. Radiolabeled small-molecule ligands for prostate-specific membrane antigen: in vivo imaging in experimental models of prostate cancer. Clin Cancer Res 2005;11:4022–8.

22. Hillier SM, Maresca KP, Femia FJ, Marquis JC, Foss CA, Nguyen N, et al. Preclinical evaluation of novel glutamate-urea-lysine analogues that target prostate-specific membrane antigen as molecular imaging pharmaceuticals for prostate cancer. Clin Cancer Res 2009;69:6932–40.

23. Zhou J, Neale JH, Pomper MG, Kozikowski AP. NAAG peptidase inhibitors and their potential for diagnosis and therapy. Nat Rev Drug Discov 2005;4:1015–26.

24. Genady AR, Janzen N, Banevicius L, El-Gamal M, El-Zaria ME, Valliant JF. Preparation and Evaluation of Radiolabeled Antibody Recruiting Small Molecules that Target Prostate Specific Membrane Antigen (PSMA) for Combined Radiotherapy and Immunotherapy. J Med Chem

2016;59:2660–73.

25. Abou-Elkacem L, Bachawal SV, Willmann JK. Ultrasound molecular imaging: Moving toward clinical translation. Eur J Radiol 2015;84:1685–93.

26. Moestue SA, Gribbestad IS, Hansen R. Intravascular targets for molecular contrast-enhanced ultrasound imaging. Int J Mol Sci 2012;13:6679–97.

27. Chang SS, O'Keefe DS, Bacich DJ, Reuter VE, Heston WDW, Gaudin PB. Prostate-specific Membrane Antigen Is Produced in Tumor-associated Neovasculature. Clin Cancer Res 1999;5:2674–81.

28. Turkbey B, Pinto PA, Choyke PL. Imaging techniques for prostate cancer: implications for focal therapy. Nat Rev Urol 2009;6:191–203.

29. Sanna V, Pintus G, Bandiera P, Anedda R, Punzoni S, Sanna B, et al. Development of polymeric microbubbles targeted to prostate-specific membrane antigen as prototype of novel ultrasound contrast agents. Mol Pharm 2011;8:748–57.

30. Wang L, Li L, Guo Y, Tong H, Fan X, Ding J, et al. Construction and In Vitro/In Vivo Targeting of PSMA-Targeted Nanoscale Microbubbles in Prostate Cancer. Prostate 2013;73:1147–58.

31. Fan X, Wang L, Guo Y, Tu Z, Li L, Tong H, et al. Ultrasonic

Nanobubbles Carrying Anti-PSMA Nanobody: Construction and Application in Prostate Cancer-Targeted Imaging. PLoS ONE 2015;10:e0127419.

32. Zlitni A, Janzen N, Foster FS, Valliant JF. Catching Bubbles: Targeting Ultrasound Microbubbles Using Bioorthogonal Inverse-Electron-Demand Diels-Alder Reactions. Angew Chem Int Ed Engl 2014;53:6459–63.

33. Liu H, Moy P, Kim S, Xia Y, Rajasekaran A, Navarro V, et al. Monoclonal Antibodies to the Extracellular Domain of Prostate-specific Membrane Antigen Also React with Tumor Vascular Endothelium. Clin Cancer Res 1997;57:3629–34.

34. Schindelin J, Arganda-Carreras I, Frise E, Kaynig V, Longair M, Pietzsch T, et al. Fiji: an open-source platform for biological-image analysis. Nat Methods 2012;9:676–82.

35. Willmann JK, Paulmurugan R, Chen K, Gheysens O, Rodriguez-Porcel M, Lutz AM, et al. US Imaging of Tumor Angiogenesis with Microbubbles Targeted to Vascular Endothelial Growth Factor Receptor Type 2 in Mice1. Radiology 2008;246:508–18.

36. Patri AK, Myc A, Beals J, Thomas TP, Bander NH, Baker JR. Synthesis and in Vitro Testing of J591 Antibody−Dendrimer Conjugates for Targeted Prostate Cancer Therapy. Bioconjugate Chem. 2004;15:1174–81.

37. Nakajima T, Mitsunaga M, Bander NH, Heston WD, Choyke PL, Kobayashi H. Targeted, Activatable, In Vivo Fluorescence Imaging of Prostate-Specific Membrane Antigen (PSMA) Positive Tumors Using the Quenched Humanized J591 Antibody–Indocyanine Green (ICG) Conjugate. Bioconjugate Chem 2011;22:1700–5.

38. Li Y, Tian Z, Rizvi SMA, Bander NH, Allen BJ. In vitro and preclinical targeted alpha therapy of human prostate cancer with Bi-213 labeled J591 antibody against the prostate specific membrane antigen. Prostate Cancer Prostatic Dis 2002;5:36–46.

39. Vallabhajosula S, Kuji I, Hamacher KA, Konishi S, Kostakoglu L, Kothari PA, et al. Pharmacokinetics and Biodistribution of 111In- and 177Lu-Labeled J591 Antibody Specific for Prostate-Specific Membrane Antigen: Prediction of 90Y-J591 Radiation Dosimetry Based on 111In or 177Lu? J Nucl Med 2005;46:634–41.

40. Haberkorn U, Eder M, Kopka K, Babich JW, Eisenhut M. New Strategies in Prostate Cancer: Prostate-Specific Membrane Antigen (PSMA) Ligands for Diagnosis and Therapy. Clin Cancer Res 2016;22:9–15.

41. Yang X, Mease RC, Pullambhatla M, Lisok A, Chen Y, Foss CA, et al. [(18)F]Fluorobenzoyllysinepentanedioic Acid Carbamates: New Scaffolds for Positron Emission Tomography (PET) Imaging of Prostate-Specific

Membrane Antigen (PSMA). J Med Chem 2015;59:206–18.

42. Jain RK. Determinants of tumor blood flow: a review. Clin Cancer Res 1988;48:2641–58.

43. Liu H, Rajasekaran AK, Moy P, Xia Y, Kim S, Navarro V, et al. Constitutive and antibody-induced internalization of prostate-specific membrane antigen. Clin Cancer Res 1998;58:4055–60.

44. Horoszewicz JS, Leong SS, Kawinski E, Karr JP, Rosenthal H, Chu TM, et al. LNCaP Model of Human Prostatic Carcinoma. Clin Cancer Res 1983;43:1809–18.

45. El-Zaria ME, Genady AR, Janzen N, Petlura CI, Vera DRB, Valliant JF. Preparation and evaluation of carborane-derived inhibitors of prostate specific membrane antigen (PSMA). Dalton Trans 2014;43:4950–61.

46. Lehr HA, Skelly M, Buhler K, Anderson B, Delisser HM, Gown AM. Microvascular endothelium of human tumor xenografts expresses mouse (= host) CD31. Int J Microcirc Clin Exp 1997;17:138–42.

4.8 Supplementary Data

Supporting information can be found in Appendix II.

5 Chapter 5 – The Development and Evaluation of uPAR-targeted MBs using Bioorthogonal Chemistry

5.1 Introduction

Urokinase plasminogen activator receptor (uPAR) is a glycoprotein that consists of three disulfide-bond linked domains which are attached to the cell membrane through a glycosyl-phosphatidylinositol (GPI) anchor (Figure 5.1).[1,2] It has been shown that uPAR has a central role in the plasminogen activation axis. This axis is directly linked to promoting cell migration, tumour growth and metastasis.[3] The expression of uPAR in healthy tissue is significantly lower compared to diseased tissue making it a good target to achieve high contrast images.[1,4,5]

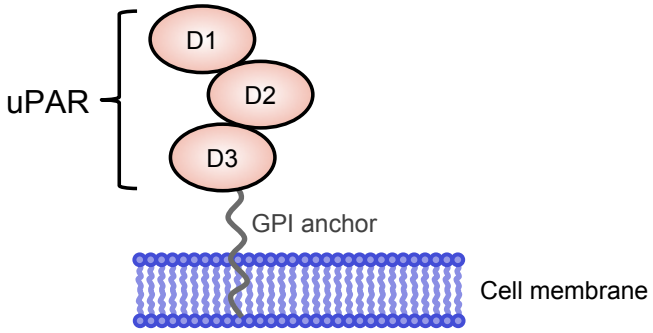

Figure 5.1 Schematic representation of uPA receptor (uPAR) and its linkage to the cell membrane.

Contrast enhanced US imaging using targeted MBs allowed the use of US for molecular imaging of various diseases such as inflammatory bowel disease and atherosclerosis as well as different types of cancers such as breast, prostate and ovarian cancer.[6-11] Because of the reported expression of uPAR on tumour endothelial cells and tumour-associated microphages,[12-14] it should be feasible to target US MBs to uPAR. It will be useful to assess uPAR expression because it is related to drug resistance, cancer aggressiveness and metastatic potential.[15-17] An US method could also be used to assess changes in the expression of uPAR during and after treatment. This will allow physicians to quickly evaluate treatment efficacy and adjust therapy accordingly. Although there are examples of uPAR-targeted agents for magnetic resonance,[18,19] fluorescent,[20-22] nuclear[20] [21] [23-25] and photoacoustic imaging,[22] to our knowledge, there are no reports of ultrasound contrast agents targeted to uPAR.[26-28]

We report here the development and evaluation of MBs targeted to uPAR. The uPAR-targeted MBs were prepared using the bioorthogonal reaction between tetrazine (Tz) and trans-cyclooctene (TCO).[29] In addition to preparing the MBs, the constructs were evaluated *in vitro* and *in vivo*.

5.2 Results and discussion

To develop uPAR-targeted MBs, MB_{Tz} was prepared by adding *N*-(4-(1,2,4,5-tetrazin-3-yl)benzyl)-6-(5-((4*S*)-2-oxohexahydro-1*H*-thieno[3,4-*d*]imidazol-4-yl)pentanamido)hexanamide (biotin-Tz, Figure 5.2) to commercially

available streptavidin coated MBs (MicroMarker™ Target-Ready contrast agents, VisualSonics) following our reported literature procedure.[29] TCO was linked to the targeting antibody by combining (E)-cyclooct-4-enyl-2,5-dioxopyrrolidin-1-yl carbonate (TCO-NHS) and anti-human-uPAR antibody at pH 9-9.5 at 4 °C overnight. The number of TCO moieties per antibody was 2.5 as determined by MALDI-TOF MS (Figure 5.3). Following the same procedure, an anti-uPAR antibody that binds to both human and mouse uPAR was conjugated with TCO for comparison.

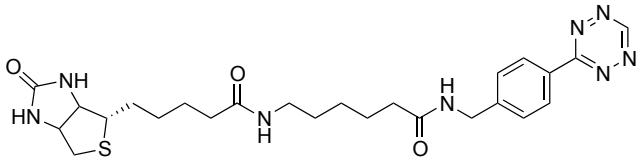

Figure 5.2 Structure of Biotin-Tz

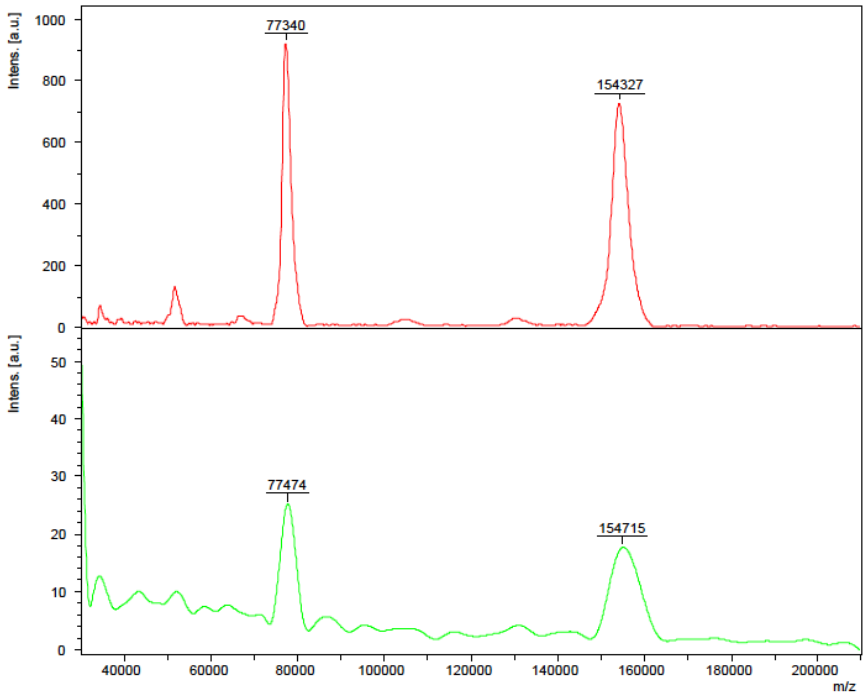

Figure 5.3 MALDI-TOF MS analysis of antibody samples. **Top:** anti-uPAR and **bottom:** TCO-anti-uPAR.

Using a flow chamber adhesion assay, the ability to target MB_{Tz} to uPAR expressing cells using TCO-anti-uPAR was evaluated. uPAR-expressing A431 cancer cells (uPAR +) and uPAR-deficient MCF7 cancer cells (uPAR −) were used in the study. Two general approaches were evaluated: For pre-targeting, the cells were first incubated with TCO-anti-uPAR for 30 min at room temperature before MB_{Tz} introduction. For the direct targeting strategy, MB_{Tz} was incubated with TCO-anti-uPAR for 20 min first to produce targeted MBs ($MB_{Tz\text{-}TCO\text{-}anti\text{-}uPAR}$), followed by exposure to cells. During the flow assay, the cells were rinsed with PBS followed by the MBs (~ 3 $\times 10^7$ MBs/mL) at 0.164 mL/min flow rate

and then washed with PBS at 1.64 mL/min. Finally, images at different fields of view were collected using a bright-field microscope and analyzed using FIJI software as previously reported.[29]

Microscopy images (Figure 5.4) and semi-quantitative analysis (Figure 5.5) show similar binding to uPAR + cells for both the pre-targeting and direct targeting strategies. This binding was significantly higher than control experiments which included MB_{Tz} on untreated uPAR + cells and unconjugated MBs (MB_C) to uPAR + cells pre-treated with TCO-anti-uPAR (Figure 5.5).

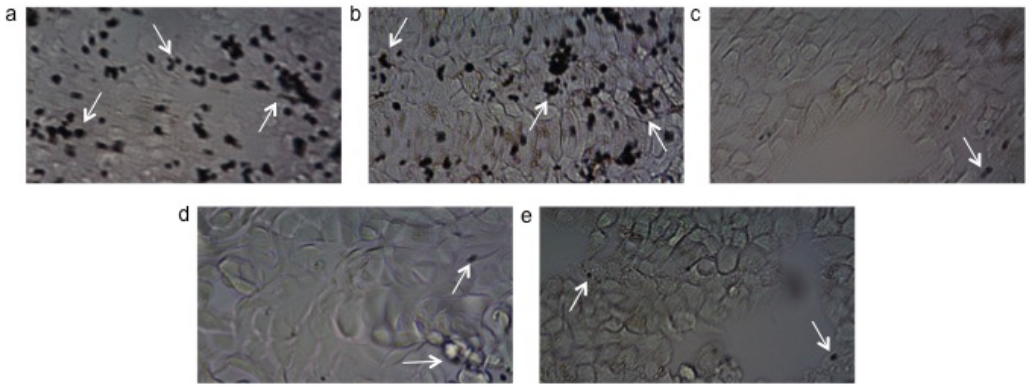

Figure 5.4 Bright-field microscopy images (20×) showing binding of: **a)** MB_{Tz} to TCO-anti-uPAR-tagged A431 cells (uPAR +); **b)** MB_{Tz} loaded with TCO-anti-uPAR ($MB_{Tz\text{-}TCO\text{-}anti\text{-}uPAR}$) to A431 cells; **c)** MB_{Tz} to A431 cells with no antibody; **d)** MB_{Tz} to TCO-anti-uPAR-tagged MCF7 cells (uPAR −); and **e)** MB_C to TCO-anti-uPAR-tagged A431 cells. The MBs appear as black spheres with select examples highlighted by the white arrows. MB_{Tz}= tetrazine-functionalized MBs; $MB_{Tz\text{-}TCO\text{-}anti\text{-}uPAR}$= MB_{Tz} incubated with TCO-anti-uPAR for 20 min; MB_C= unmodified MBs (MicroMarker™ target-ready contrast agents, VisualSonics).

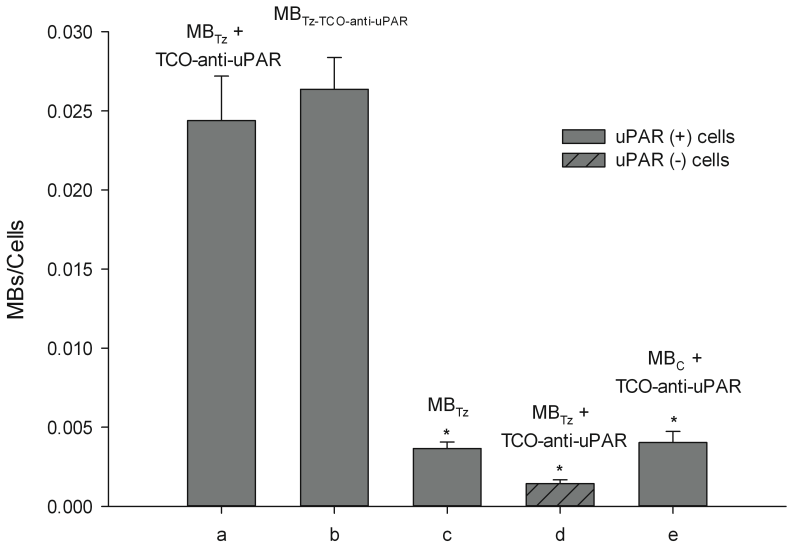

Figure 5.5 Semi-quantitative analysis of the number of MBs bound per cell based on relative area from the flow chamber adhesion assay following washing. For A431 (uPAR +) cells, near-equivalent binding was seen when (a) MB_{Tz} was exposed to cells pre-incubated with TCO-anti-uPAR for 30min and (b) where MB_{Tz} was first incubated with TCO-anti-uPAR for 20 min ($MB_{Tz\text{-}TCO\text{-}anti\text{-}uPAR}$) before exposure to A431 cells. Binding of MB_{Tz} in both (a) and (b) was significantly higher than for (c) experiments that lacked any TCO-anti-uPAR and (d) when using MCF7 (uPAR −) cells. Unmodified MBs (MB_C) (e) showed minimal binding to TCO-anti-uPAR-tagged A431 cells. MB_{Tz}= tetrazine-functionalized MBs; $MB_{Tz\text{-}TCO\text{-}anti\text{-}uPAR}$= MB_{Tz} incubated with TCO-anti-uPAR for 20 min; MB_C= unmodified MBs (MicroMarker™ target-ready contrast agents, VisualSonics). Area measurements were determined using FIJI software. *Statistically significant difference ($p < 0.001$) relative to both (a) and (b) (analyzed using one-way ANOVA).

The direct targeting strategy was further evaluated *in vivo* in a uPAR expressing 231/LM2-4 tumour model which is a highly metastatic variant of the

human breast cancer cell line MDA-MB-231.[30] In the *in vivo* study, MBs (70 µL) were injected and allowed to accumulate at the site of interest for 4 minutes before a destruction replenishment sequence was conducted.[29] Each mouse was imaged with MB_{Tz} first then imaged with $MB_{Tz\text{-}TCO\text{-}anti\text{-}uPAR}$ in the same plane of view. A 15 minutes break and 3D destruction sequence was applied between the two imaging sessions to ensure clearance of previously injected MBs. After the imaging study, the animals were euthanized and the tumours extracted and frozen in liquid N_2 for further evaluation by western blot analysis and immunohistochemistry. To quantify the amount of MBs binding to the target, the US images were analyzed using VevoCQ™ software (VisualSonics). The average intensity over 200 frames acquired 5 seconds after destruction was subtracted from the average intensity over 200 frames acquired before destruction and images were produced as parametric images overlaid on the non-linear contrast mode image. The same *in vivo* study was also repeated using an anti-uPAR antibody that binds to both human and mouse uPAR.

In contrast to the *in vitro* studies, with either antibody, the parametric US images did not show qualitatively difference in signal enhancement when using the non-targeted MB_{Tz} versus the targeted $MB_{Tz\text{-}TCO\text{-}anti\text{-}uPAR}$ (Figure 5.6 and 5.7). When the signal enhancement was quantified using the VevoCQ software it was shown that there was no significant difference between the signal enhancement when using the non-targeted MBs (MB_{Tz}) versus the targeted MBs ($MB_{Tz\text{-}TCO\text{-}anti\text{-}}$

$_{uPAR}$) (Figure 5.8 and 5.9).

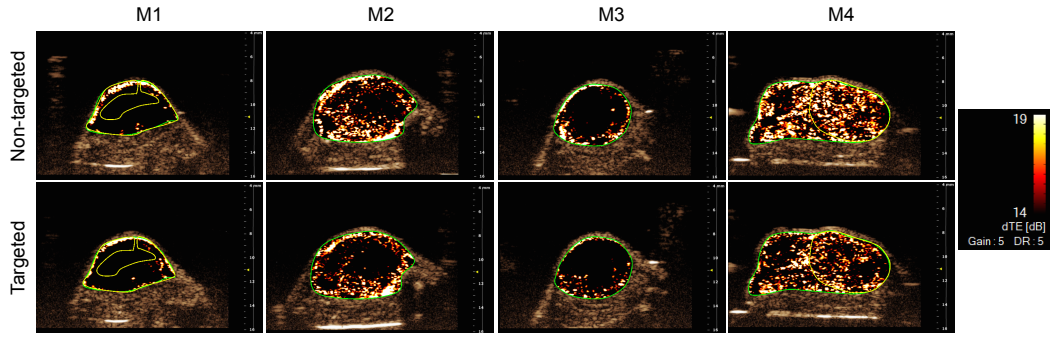

Figure 5.6 Transverse color-coded parametric images overlaid on a nonlinear contrast mode ultrasound image acquired 4 min after intravenous administration of either MB_{Tz} to 231/LM2-4 xenograft tumour mouse model (**top**) or $MB_{Tz\text{-}TCO\text{-}anti\text{-}uPAR}$ to the same mouse after clearance of MB_{Tz} (**bottom**). Qualitatively, the signal enhanced when using the human uPAR-targeted MBs ($MB_{Tz\text{-}TCO\text{-}anti\text{-}uPAR}$, bottom) showed no difference in signal enhancement compared to non-targeted MBs (MB_{Tz}, top). dTE= differential targeted enhancement.

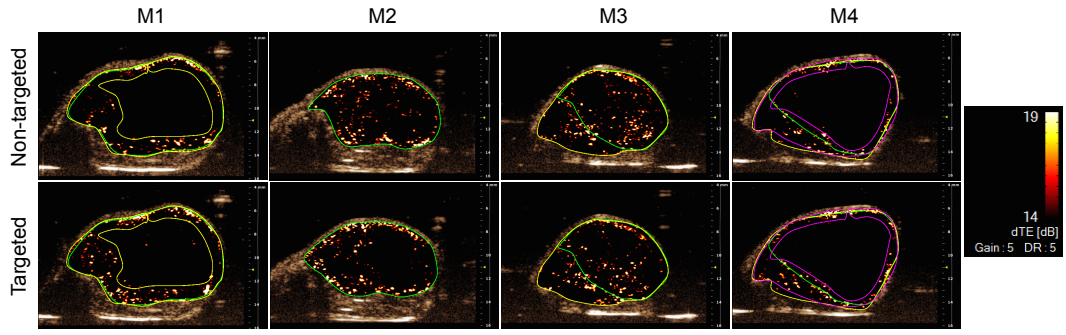

Figure 5.7 Transverse colour-coded parametric images overlaid on a nonlinear contrast mode ultrasound image acquired 4 min after intravenous administration of either MB_{Tz} to 231/LM2-4 xenograft tumour mouse model (**top**) or $MB_{Tz\text{-}TCO\text{-}anti\text{-}uPAR}$ to the same mouse after clearance of MB_{Tz} (**bottom**). Qualitatively, the signal enhanced when using the human and mouse uPAR-targeted MBs ($MB_{Tz\text{-}}$

$_{TCO\text{-}anti\text{-}uPAR}$, bottom) showed no difference in signal enhancement compared to non-targeted MBs (MB_{Tz}, top). dTE= differential targeted enhancement.

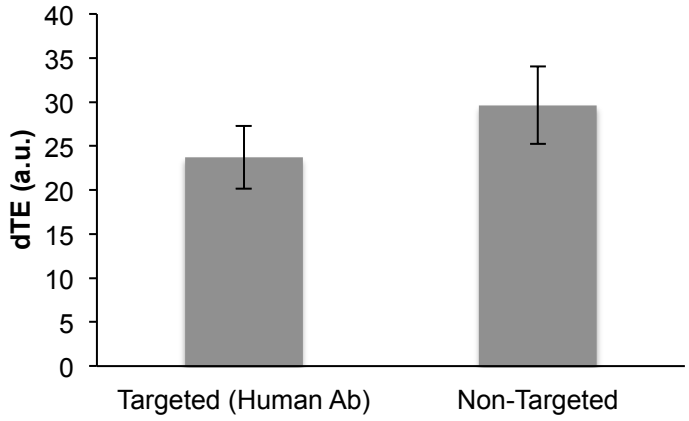

Figure 5.8 A bar graph representation of the quantified signal enhancement obtained when using MBs targeted to human uPAR ($MB_{Tz\text{-}TCO\text{-}anti\text{-}uPAR}$) versus non-targeted MBs (MB_{Tz}). There was no significant difference between the signal enhancements (analyzed using one-way ANOVA).

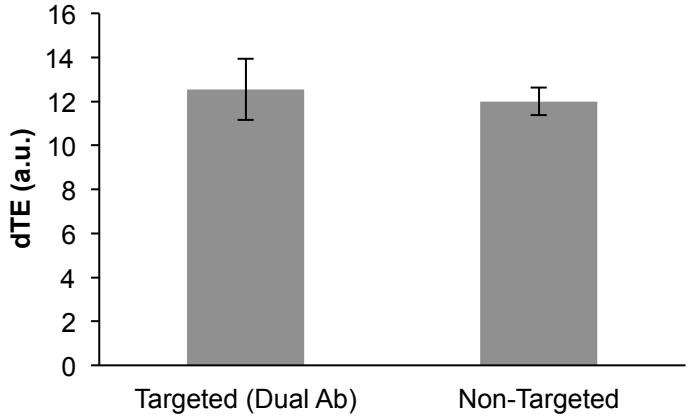

Figure 5.9 A bar graph representation of the quantified signal enhancement obtained when using MBs targeted to human and mouse uPAR ($MB_{Tz\text{-}TCO\text{-}anti\text{-}uPAR}$) versus non-targeted MBs (MB_{Tz}). There was no significant difference between the

signal enhancements (analyzed using one-way ANOVA).

A western blot and immunostaining analysis was conducted to confirm the expression of uPAR (human and mouse) in tumours used for imaging. For western blot analysis, lysates prepared from extracted tumours were fractionated on SDS-PAGE and electro-transferred to PVDF membrane. uPAR expression was assessed by incubating with a rabbit anti-uPA receptor antibody followed by AP-Goat anti-rabbit IgG (H+L) and visualized after incubating with a chemiluminescent reagent (ECF substrate). Figure 5.10 shows the expression of uPAR in the tumour lysates which qualitatively looks similar between tumours.

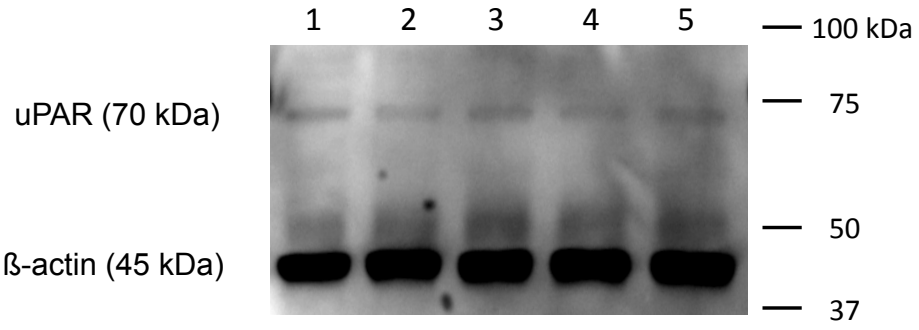

Figure 5.10 Western Blot analysis of uPAR expression in 231/LM2-4 tumour lysates. uPAR expression in 231/LM2-4 tumour lysates (10 µg of protein) using a rabbit anti-uPA receptor primary antibody in a 1:100 dilution, an AP-Goat anti-rabbit IgG (H+L) secondary antibody in a 1:5000 dilution and a chemiluminescence detection system. ß-actin expression was used as loading control. Top band represents uPAR (70 kDa) while the bottom band represents ß-actin (45 kDa).

Immunostaining was used to assess the expression of uPAR (human and

mouse) on endothelial cells. uPAR on endothelial cells were detected by incubating the tumour tissue slices with a mixture of a rabbit anti-uPA receptor antibody and a hamster anti-CD31 antibody [2H8]. The expression was then visualized with a Cy5-conjugated donkey anti-rabbit IgG and a fluorescein (FITC)-labeled goat anti-armenian hamster IgG (H+L) respectively. To take into account signals coming from background or non-specific binding of secondary antibodies, tissue slices were imaged without incubation of primary antibody or both primary and secondary antibodies. Images obtained from immunostaining slides showcased the expression of both endothelial cells and uPAR on the tumour tissue (Figure 5.11). When looking at the overlaid images we find that the uPAR expression on endothelial cells was also evident (Figure 5.12).

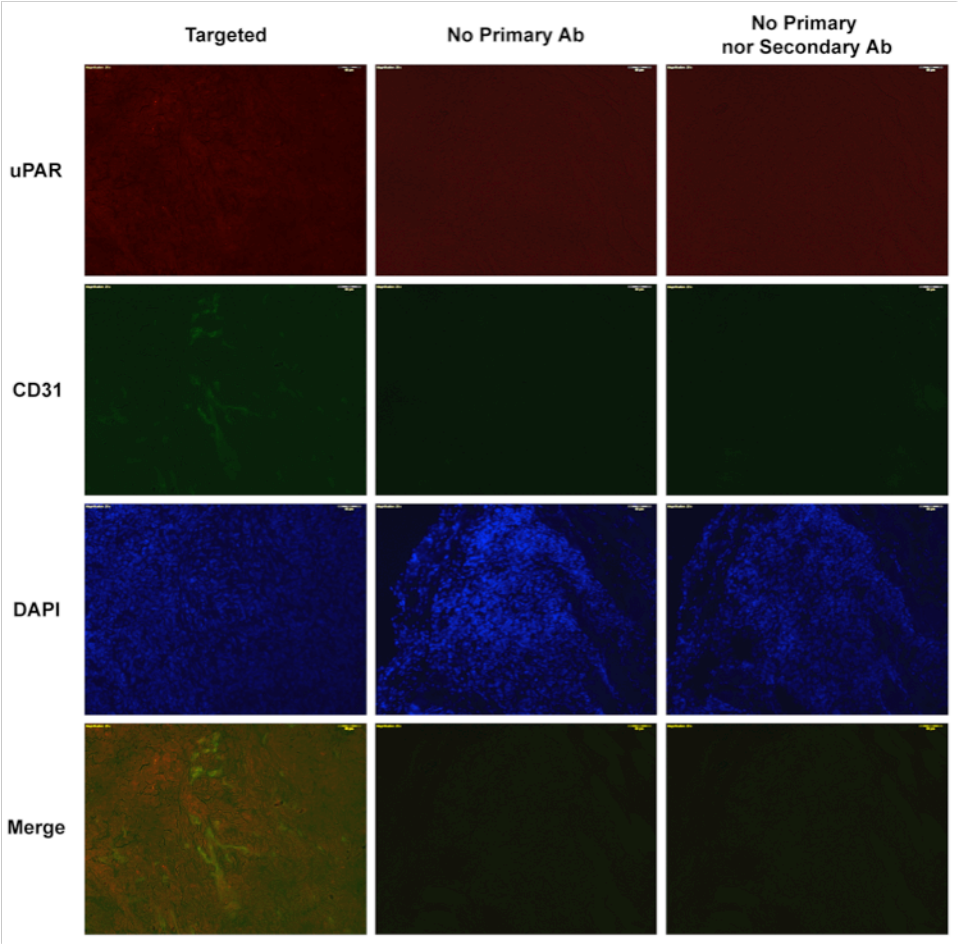

Figure 5.11 Immunofluorescence staining images of 231/LM2-4 tumour tissue slices after staining for human and mouse uPAR and CD31. DAPI was also used to stain the nucleus. Images on the left show presence of both uPAR and endothelial cells (CD31) on 231/LM2-4 tumour tissue. The fluorescence shown was qualitatively higher than auto-fluorescence represented in the far right. As a control, slices were also incubated with just the secondary antibodies to visualize any non-specific binding and no fluorescence was observed (middle).

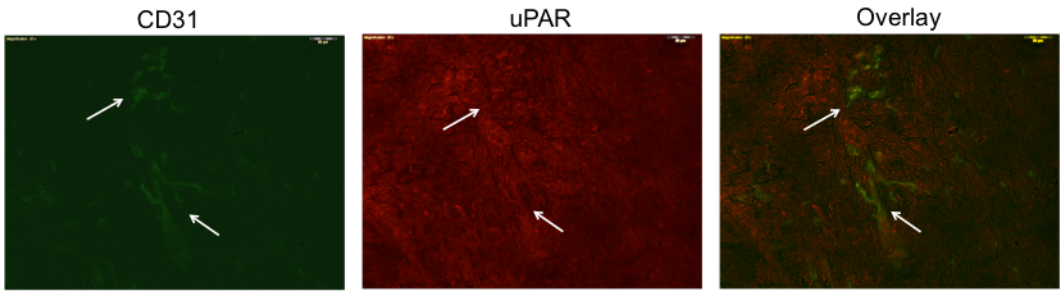

Figure 5.12 Immunofluorescence staining images of 231/LM2-4 tumour tissue. Images show expression of endothelial cells (CD31) (**left**), human and mouse uPAR (**middle**) and overlay (**right**). The overlay image shows co-localization of uPAR on endothelial cells (white arrows).

5.3 Conclusion

The reported work showcases the ability of using the inverse-electron-demand Diels-Alder reaction between Tz and TCO to created MBs that can bind to uPAR. *In vitro* studies using a flow chamber system showed that uPAR mediated MBs localization was observed on cells. Furthermore, targeting of MBs was achieved using both the direct- and pre-targeting strategies. Unfortunately, the evaluation of the direct targeting strategy *in vivo* did not show difference in signal enhancement between targeted and non-targeted MB_{Tz}. The inability in targeting MB_{Tz} using the human-specific uPAR antibody could be due to the lack of expression or accessibility of human uPAR on mouse endothelial cells in the tumour xenograft due to the large MBs. With respect to the former hypothesis no improvement was seen when a human and mouse specific uPAR antibody was employed suggesting accessibility and effective binding to the target was the main

issue.

5.4 Materials, Instruments and General Information

Microbubbles (MBs) were obtained using MicroMarker™ Target-Ready Contrast Agent Kit (VisualSonics Inc., Toronto, Canada; 8.4×10^8 MBs/vial). Streptavidin coated magnetic beads (New England BioLabs) and MACSiMAG™ Separator (MiltenyiBiotec) magnet were used during the purification of MBs. Conjugated-antibodies were analyzed on a MALDI Bruker Ultraflextreme Spectrometer. MBs size and concentration were determined using Z2 Coulter counter (Beckman Coulter, Fullerton, California). Biotin-Tz (Figure 5.2) was synthesized as previously reported.[29]

5.5 Experimental

5.5.1 Preparation of TCO-modified anti-uPAR antibody

The TCO-modified antibody was prepared following the reported literature procedure.[29] Briefly, the pH of a solution of anti-uPAR antibody in PBS (American Diagnostica Inc., 3936) (450 µL, 225 µg, 1.5 nmol) was adjusted to 9 by adding 3 µL of 1 M Na_2CO_3(aq). This was followed by the addition of (E)-cyclooct-4-enyl-2,5-dioxopyrrolidin-1-yl carbonate (TCO-NHS, 8 µg, 30 nmol, 20 eq) in DMSO (4 µL). The solution was left on a shaker overnight at 4 °C. The desired product was isolated from excess TCO using an Amicon Ultra-0.5 Centrifugal filter (30 kDa) and washed with PBS three times. MALDI-TOF MS

analysis of the antibody before and after conjugation to TCO showed an average of 2.5 TCO groups per antibody. The process was repeated using a polyclonal rabbit anti-uPAR antibody (FL-290, sc-10815) that reacts with both human and mouse uPAR.

5.5.2 Cells and Culture Methods

A431 (CRL-1740) cells were cultured in DMEM media supplemented with 10% fetal bovine serum and 1% penicillin streptomycin. MCF7 (HTB-22) cells were cultured in Eagle's Minimum Essential Medium (EMEM) supplemented with 10% fetal bovine serum and 1% penicillin streptomycin. The cell lines were maintained at 37 °C under 5% CO_2.

5.5.3 Preparation of Microbubbles (MBs)[29]

Streptavidin coated MBs (MicroMarker™ Target-Ready contrast agents, VisualSonics) were reconstituted in 500 µL sterile saline (0.9% sodium chloride) according to the manufacturer's instructions. To prepare the tetrazine-coated MBs (MB_{Tz}), biotin-Tz (70 µg, 1.35×10^{-4} mmol) in 50 µL of saline:MeOH (1:1 v/v) was added dropwise to the reconstituted MBs. After 45 min, 200 µL of the bottom of the solution was removed carefully with minimal agitation of the bubbles and was discarded. Streptavidin coated magnetic beads (200 µL) were added whereupon after 20 min, 200 µL of bottom solution was removed carefully and discarded and the sample placed beside a magnet. After decanting the solution, MBs were rinsed with 200µL saline and then transferred to another vial. MB_{Tz}-

$_{TCO\text{-}antibody}$ was prepared by incubating 50 μL of MB_{Tz} solution with 20 μL of TCO-antibody (10 μg) for 20 min before running the experiment.

5.5.4 Flow Chamber Cell Adhesion Assay[†]

The flow assay was adapted from the reported literature procedure.[29] Cells (8×10^5) were plated separately in 30 mm Corning tissue culture dishes 2 days prior to running the assay. For MB_{Tz} and associated controls, cells were incubated with TCO-antibody (30 μg/mL) for 30 min prior to running the assay. The parallel-plate flow chamber (Glycotech, Rockville, Md.) was setup as shown in Figure S. 4.3. Using a syringe pump (PhD 2000, Harvard Apparatus, Holliston, USA) cells were first rinsed with 1 mL PBS, 1 mL of MBs solution at a wall shear rate of 100 sec^{-1} (flow rate = 0.164 mL/min) and subsequently with 2 mL PBS at 1000 sec^{-1} shear rate. Binding of MBs was visualized using a Celestron PentaView LCD Digital Brightfield S4 Microscope with 20× objective. Images were recorded and the extent of binding assessed by comparing the area covered by MBs to the total area covered by cells in each image using image analysis (FIJI) software.[31]

5.5.5 Animal Model

All animal studies were approved by the Animal Research Ethics Board at Sunnybrook Health Sciences Centre. Mice were maintained with 12 hour light/dark cycles and given food and water ad libitum. 231/LM2-4 cells which are

[†] TCO-anti-uPAR preparation, cell culture and flow assay was conducted with Mahmoud El-Gamal.

a highly metastatic variant of the human breast cancer cell line MDA-MB-231 were used in the *in vivo* studies. Preparation of the tumour mice xenograft was performed by Melissa Yin.

5.5.6 Tumour Extraction

Mice were sacrificed directly after imaging and the tumours were excised, rinsed with PBS, frozen in liquid N_2 and then stored at -80 °C.

5.5.7 Ultrasound (US) Imaging

Imaging Non-linear contrast mode ultrasound imaging was performed using a Vevo 2100 imaging system (VisualSonics). Imaging was performed at 18 MHz on 231/LM2-4 tumour bearing mice using a solid-state transducer (MS-250; VisualSonics). During imaging, animals were kept under anesthesia using isoflurane (4% initiation, 2% maintenance). Using a syringe pump (600 μL/min) and in random order, mice were injected with 70 μL of either MB_{Tz} followed by $MB_{Tz\text{-}TCO\text{-}anti\text{-}uPAR}$ or $MB_{Tz\text{-}TCO\text{-}anti\text{-}uPAR}$ followed by MB_{Tz}. After each injection, MBs were allowed to circulate for 4min before a destruction replenishment sequence was initiated. A set of 200 frames was acquired before a continuous high power destruction pulse (100% transmit power) was applied within the imaging window. Freely circulating MBs were allowed to refill the tumour for 5 seconds before acquiring another set of 200 frames. There was a 20 min delay after each imaging to ensure complete clearance of previously injected MBs. The differential targeted enhancement (dTE) signal was measured using the advanced

contrast quantification software analysis tool (VevoCQ, VisualSonics). Regions of interest were determined based on the distribution of the MBs in the tumour (the vascular region), which was the same in each mouse between the two types of MBs injected.

5.5.8 Tumour lysate preparation

Excised frozen tumours were divided to two halves, one for lysate preparation and the other for immunohistochemical analysis. Frozen tumour was thawed and put into lysis buffer containing 1% IGEPAL CA-630 (Sigma-Aldrich, I3021), 20 mM Tris pH 8.0 (Sigma-Aldrich, 154563), 137 mM NaCl (Sigma-Aldrich, S6191), 10% glycerol (Caledon Laboatories, 5350-1), 2 mM EDTA (Sigma-Aldrich, E5134) and Protease Inhibitor cocktail (Bioshop, PIC003). Tumour was then homogenized using VWR PowerMax AHS 200 homogenizer (5 × 75 mL troemner) and lysate was collected after centrifugation (2000 × g, 5 min) and washing 3× with PBS. Protein concentration was determined using a Pierce® BCA Protein Assay Kit (ThermoFisher Scientific).

5.5.9 Western Blot analysis on 231/LM2-4 tumour lysates

Using immunoblotting, uPAR-expression in 231/LM2-4 tumour lysates was assessed. 10 μg of protein from each cell lysate was loaded on 10% Mini-PROTEAN TGX precast gels and fractionated by SDS-PAGE. After electro-transferring the protein extracts to polyvinylidene difluoride (PVDF) membranes, the PVDF membrane was incubated with a mixture of Rabbit anti-uPA receptor

antibody (ab103791, 1:100) and β-actin (13E5) rabbit mAb (Cell Signalling Technology, 4970S, 1:2000) overnight at 4 °C. Following washing the membrane, it was incubated with AP-Goat anti-rabbit IgG (H+L) (Jackson ImmunoResearch, 111055045, 1:5000) for 1 hr at room temperature. The membrane was finally washed and incubated with a chemiluminescent reagent (ECF substrate, GE RPN5785) for 5 min and imaged using a STORM 840 imaging system.

5.5.10 Immunohistochemistry analysis on 231/LM2-4 tumour slices

Frozen tissue slices of the tumour (20 μm thick) were thawed and incubated for 15 min in 4% PFA (paraformaldehyde) in PBS at room temperature. Slides were then washed with 0.25% Triton X-100 and 0.1% Tween before outlining the sections with immunopen. Slices were incubated with a blocking buffer containing 2% donkey serum, 1% BSA, 0.1% Tween 20 and 0.3 M glycine in PBS for 1 hr at room temperature. Tissue sections were then incubated with a mixture of hamster anti-CD31 antibody [2H8] (ab119341, 1:100) and rabbit anti-uPA receptor antibody (ab103791, 1:100) overnight at 4 ºC. The targets were then visualized with fluorescein (FITC) AffiniPure goat anti-Armenian hamster IgG (H+L) (Jackson immuno; 127-095-099, 1:100) and Cy5-conjugated AffiniPure donkey anti-rabbit IgG (Jackson Laboratories, 711-175-152, 1:200) respectively. After washing with 0.1% tween in PBS, slices were mounted using permount + DAPI mounting medium and covered with a cover slip. All slices were imaged using an upright brightfield and fluorescent microscope (BX53, Olympus) and

images are captured using a QImaging Retiga 2000R camera (monochromatic, BX53) and processed using cellSens Dimension™ software. As a control, slices were also imaged without incubation of any antibody to visualize auto fluorescence and without primary antibody to visualize any non-specific binding of the secondary antibody.

5.6 References

[1] F. Blasi, P. Carmeliet, *Nat. Rev. Mol. Cell Biol.* **2002**, *3*, 932–943.

[2] M. Ploug, V. Ellis, *FEBS Letters* **1994**, *349*, 163–168.

[3] N. Sidenius, F. Blasi, *Cancer Metastasis Rev.* **2003**, *22*, 205–222.

[4] E. Bianchi, R. L. Cohen, A. T. Thor, R. F. Todd, I. F. Mizukami, D. A. Lawrence, B. M. Ljung, M. A. Shuman, H. S. Smith, *Clin. Cancer Res.* **1994**, *54*, 861–866.

[5] Y. Li, P. J. Cozzi, *Cancer Treat. Rev.* **2007**, *33*, 521–527.

[6] L. Abou-Elkacem, S. V. Bachawal, J. K. Willmann, *Eur. J. Radiol.* **2015**, *84*, 1685–1693.

[7] X. Fan, L. Wang, Y. Guo, Z. Tu, L. Li, H. Tong, Y. Xu, R. Li, K. Fang, *PLoS ONE* **2015**, *10*, e0127419.

[8] J. K. Willmann, R. Paulmurugan, K. Chen, O. Gheysens, M. Rodriguez-Pocel, A. M. Lutz, I. Y. Chen, X. Chen, S. S. Gambhir, *Radiology* **2008**, *246*, 508–518.

[9] N. Deshpande, Y. Ren, K. Foygel, J. Rosenberg, J. K. Willmann, *Radiology* **2011**, *258*, 804–811.

[10] N. Deshpande, A. M. Lutz, Y. Ren, K. Foygel, L. Tian, M. Schneider, R. Pai, P. J. Pasricha, J. K. Willmann, *Radiology* **2012**, *262*, 172–180.

[11] B. A. Kaufmann, C. L. Carr, J. T. Belcik, A. Xie, Q. Yue, S. Chadderdon, E.S. Caplan, J. Khangura, S. Bullens, S. Bunting, et al., *Arterioscler. Thromb. Vasc. Biol.* **2010**, *30*, 54–59.

[12] S. Nozaki, Y. Endo, S. Kawashiri, K. Nakagawa, E. Yamamoto, Y. Yonemura, T. Sasaki, *Oral Oncol.* **1998**, *34*, 58–62.

[13] M. V. Carriero, P. Franco, S. Del Vecchio, O. Massa, G. Botti, G. D'Aiuto, M. P. Stoppelli, M. Salvatore, *Clin. Cancer Res.* **1994**, *54*, 5445–5454.

[14] F. Blasi, *Fibrinolysis* **1988**, *2*, 73–84.

[15] A. Singh, J. Settleman, *Oncogene* **2010**, *29*, 4741–4751.

[16] H. W. Smith, C. J. Marshall, *Nat. Rev. Mol. Cell Biol.* **2010**, *11*, 23–36.

[17] H. Miyake, I. Hara, K. Yamanaka, S. Arakawa, S. Kamidono, *Int. J. Oncol.* **1999**, *14*, 535–541.

[18] G. Y. Lee, W. P. Qian, L. Wang, Y. A. Wang, C. A. Staley, M. Satpathy, S. Nie, H. Mao, L. Yang, *ACS Nano* **2013**, *7*, 2078-2089.

[19] Y. Chen, L. Gong, N. Gao, J. Liao, J. Sun, Y. Wang, L. Wang, P. Zhu, Q. Fan, Y. A. Wang, et al., *Int. J. Nanomed.* **2015**, *10*, 6689–6698.

[20] Y. Sun, X. Ma, K. Cheng, B. Wu, J. Duan, H. Chen, L. Bu, R. Zhang, X. Hu, Z. Deng, et al., *Angew. Chem. Int. Ed. Engl.* **2015**, *54*, 5981–5984.

[21] A. M. LeBeau, N. Sevillano, M. L. King, S. Duriseti, S. T. Murphy, C. S. Craik, L. L. Murphy, H. F. VanBrocklin, *Theranostics* **2014**, *4*, 267–279.

[22] L. Xi, S. R. Grobmyer, G. Zhou, W. Qian, L. Yang, H. Jiang, *Journal of Biophotonics* **2014**, *7*, 401–409.

[23] M. Persson, K. Juhl, P. Rasmussen, M. Brandt-Larsen, J. Madsen, M. Ploug, A. Kjaer, *Mol. Pharm.* **2014**, *11*, 2796–2806.

[24] M. Hu, J. Chio, T. Wu, R. Simms, J. Forbes, K. Stephenson, J. Valliant, *J. Nucl. Med.* **2014**, *55*, 1074–1074.

[25] M. Persson, H. H. El Ali, T. Binderup, A. Pfeifer, J. Madsen, P. Rasmussen, A. Kjaer, *Nucl. Med. Biol.* **2014**, *41*, 290–295.

[26] M. Persson, A. Kjaer, *Clin. Physiol. Funct. Imaging* **2013**, *33*, 329–337.

[27] M. Persson, M. Nedergaard, M. Brandt-Larsen, D. Skovgaard, J. T. Jørgensen, S. R. Michaelsen, J. Madsen, U. Lassen, H. S. Poulsen, A. Kjaer, *J. Nucl. Med.* **2015**, *57*, 272–278.

[28] K. Hirata, N. Tamaki, *J. Nucl. Med.* **2016**, *57*, 169–170.

[29] A. Zlitni, N. Janzen, F. S. Foster, J. F. Valliant, *Angew. Chem. Int. Ed.*

Engl. **2014**, *53*, 6459–6463.

[30] R. Munoz, S. Man, Y. Shaked, C. R. Lee, J. Wong, G. Francia, R. S. Kerbel, *Clin. Cancer Res.* **2006**, *66*, 3386–3391.

[31] J. Schindelin, I. Arganda-Carreras, E. Frise, V. Kaynig, M. Longair, T. Pietzsch, S. Preibisch, C. Rueden, S. Saalfeld, B. Schmid, et al., *Nat. Methods* **2012**, *9*, 676–682.

6 Chapter 6: Data analysis and application of bioorthogonal chemistry to other classes of US contrast agents

6.1 Image acquisition and processing refinement for targeted US imaging using tetrazine functionalized microbubbles (MB_{Tz})

6.1.1 Introduction

All US imaging experiments described in previous chapters were based on the acquisition sequence reported by Willmann and coworkers[1] (Figure 6.1). In collaboration with the Foster group, the evaluation of targeting MB_{Tz} to VEGFR2 *in vivo* using the direct and pre-targeted strategy in a larger cohort of animals was performed and the data compared to the traditional targeting approach used by Willmann and coworkers.[1] After looking at the results, it was found that a new US sequence was needed due to the difference in distribution and stability of streptavidin coated MBs (MB_C) loaded with biotin-Tz (MB_{Tz}) versus biotin-antiVEGFR2 antibody (MB_V) used by Willmann *et al*.‡

‡ The work described in sections 6.1 was done through collaboration with Dr. Stuart Foster's group. A manuscript on this work is under preparation for submission to the journal of Ultrasound in Medicine and Biology as a technical note. The paper is coauthored with Melissa Yin where all the experiments were conceived and performed equally by Melissa and myself.

6.1.2 Results and Discussion

6.1.2.1 In vivo US imaging of VEGFR2 using the previously reported[1] US Image Acquisition Sequence

The pre-targeting strategy was evaluated in a mouse bearing a Lewis Lung Carcinoma tumour that is known to express VEGFR2. Tumour xenograft mice (n= 4) were injected with TCO-antiVEGFR2 antibody (100 μg, 200μL) 24 hr before imaging session. In the imaging session, the pre-treated mice were injected with MB_{Tz} (70 μL, ~ 6.9×10^6 MBs/mL) and US imaging was conducted as previously reported.[2] Briefly, MBs were allowed to bind to the target and clear from circulation for 4 min before a distruction replenishment sequence was initiated (Figure 6.1). As a control, another set of tumour xenograft mice (n= 3) that had not been pre-treated with TCO-antiVEGFR2, were injected with the same amount of MB_{Tz} and imaged following the same US sequence. US images were analyzed as previously reported in Chapter 3[2] and US signal enhancement and parametric images were produced.

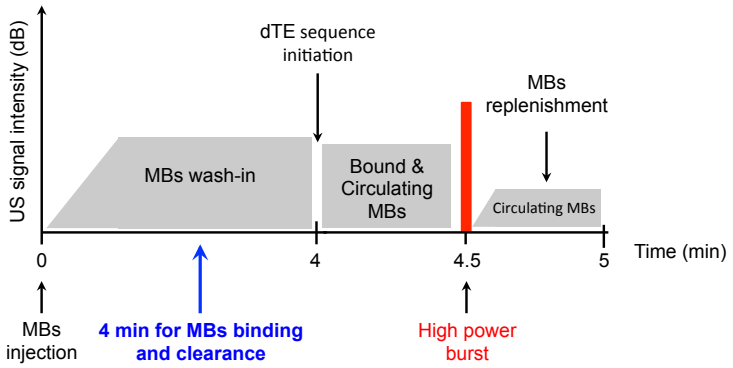

Figure 6.1 Original US image acquisition sequence used by Willmann and coworkers.[1] MBs are injected and allowed to bind to the target and clear from circulation for 4min before initiating the destruction replenishment sequence (dTE).

Looking at the parametric US images overlaid on the non-linear contrast mode US image, we found that higher signal enhancement when injecting MB_{Tz} to mouse xenografts pre-treated with TCO-antiVEGFR2 was observed (Figure 6.2). These results correlate with the previously reported imaging results.[2] Furthermore, when quantifying the signal enhancement in the images, the pre-targeting strategy had 2.6 fold more signal enhancement and was significantly higher than that of non-targeted MB_{Tz} (Figure 6.3).

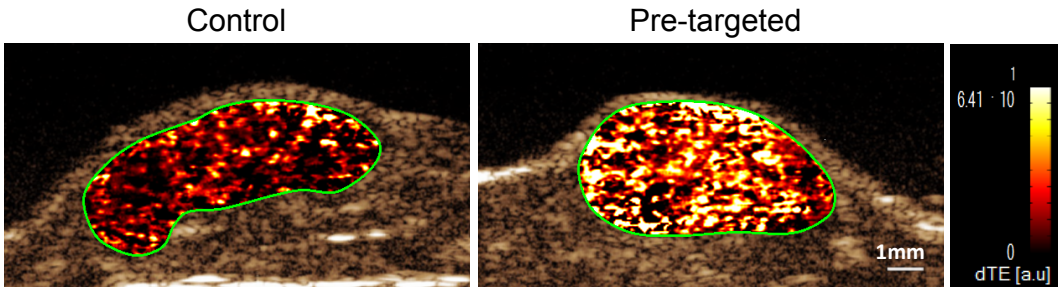

Figure 6.2 Transverse color-coded parametric nonlinear contrast mode ultrasound images acquired 4 min after intravenous administration of MB_{Tz} to **left:** Lewis Lung Carcinoma tumour model (VEGFR2 +) without administering TCO–antiVEGFR2; and **right:** pre-administered with TCO–antiVEGFR2 24 hr before imaging. Regions of interest were based on the vascularity of the tumours determined from the initial distribution of the MBs following injection. dTE= differential targeted enhancement.

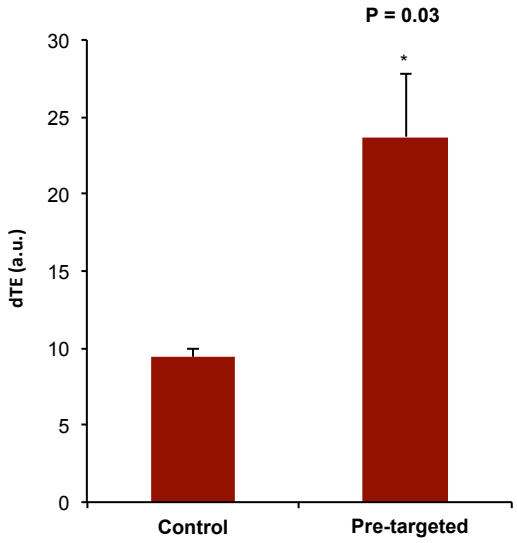

Figure 6.3 Quantitative analysis of the differential targeted enhancement (dTE) signal obtained from the ultrasound images. Control= MB_{Tz} without pre-treating the animal with TCO-antiVEGFR2 24 hr before imaging (n= 3), and pre-targeted= MB_{Tz} in animals pre-treated with TCO-antiVEGFR2 24 hr before

imaging (n= 4). *Statistically significant difference (p= 0.03) relative to control (analyzed using one-way ANOVA).

6.1.2.2 Comparison of Targeting Strategies

A direct head-to-head comparison between the traditional approach (MB_V) involving biotinylated antiVEGFR2 directly ligated to MBs, pre-targeting (MB_{Tz} + TCO-antiVEGFR2) and direct targeting ($MB_{Tz\text{-}TCO\text{-}antiVEGFR2}$) strategies was conducted. Mice bearing a Lewis Lung Carcinoma tumour (n= 6 per study) were injected with either MB_V, MB_{Tz} (non-targeted control) or $MB_{Tz\text{-}TCO\text{-}antiVEGFR2}$. Furthermore, another set of mice (n= 6) were injected with TCO-antiVEGFR2 (200 μg, 100 μL) 24 hr before imaging with MB_{Tz} to evaluate the pre-targeting strategy. The imaging sequence and US data analysis was performed as previously discussed (Figure 6.1).

Looking at the quantified US signal enhancement (Figure 6.4), we found that other than the conventional targeting strategy (MB_V), both the direct and indirect strategy did not show much difference in signal enhancement compared to the control. This was unexpected since the direct strategy ($MB_{Tz\text{-}TCO\text{-}antiVEGFR2}$) and conventional approach (MB_V=$MB_{Biotin\text{-}antiVEGFR2}$) employed the same antibody and MBs differing only in the nature of the linker. Furthermore, the results obtained using the pre-targeting strategy did not coincide with the previous evaluation in section 6.1.2.1 (Figure 6.3).

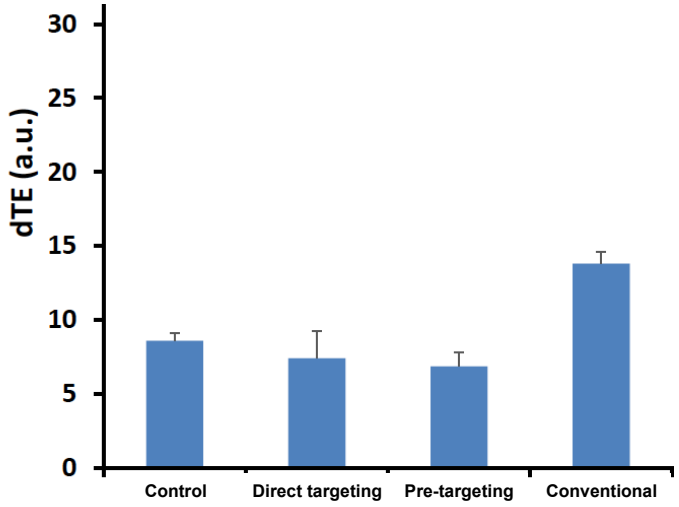

Figure 6.4 Quantitative analysis of the differential targeted enhancement (dTE) signal obtained from the ultrasound images. Control= MB_{Tz} without pre-treating the animal with TCO-antiVEGFR2 24 hr before imaging, direct targeting= $MB_{Tz\text{-}TCO\text{-}antiVEGFR2}$, pre-targeting= MB_{Tz} in animals pre-treated with TCO-antiVEGFR2 24 hr before imaging and conventional= MB_V.

A full quantitative analysis of the US signal enhancement, which correlates to the amount of MBs in the imaging window, was performed in all mice used in the study (Table 6.1). One observation was the relatively low peak enhancement during the pre-targeting strategy evaluation (419 a.u. ± 130) compared to conventional, control and direct targeting experiments (824 a.u. ± 271; 792 a.u. ± 108 and 744 a.u. ± 230 respectively). This suggested that the amount of MBs injected during the evaluation of the pre-targeting strategy was less than that in the other studies. This could be due to either an error during the tail vein injection or due to not using a fresh batch of MBs during the imaging session, whereby the concentration of intact MBs would decrease.

Table 6.1 Summary of the quantified US signal enhancement within the imaging window for each mouse. **Peak enhancement** represents the US signal enhancement upon injecting the MBs (i.e. amount of MBs injected); **Pre-burst enhancement** represents the US signal before bursting the MBs (i.e. signal coming from bound and free-circulating MBs); **Post-burst enhancement** represents the signal after bursting MBs within the region of interest (i.e. signal coming from free-circulating MBs).

		Peak Enhancement (a.u.)	Pre-burst Enhancement (a.u.)	Post-burst Enhancement (a.u.)
Control (MB_{Tz})	M1	931	803	648
	M2	824	656	452
	M3	610	541	384
	M4	828	644	488
	M5	819	536	457
	M6	741	550	420
AVERAGE		**792.17**	**621.67**	**474.83**
Direct targeting Strategy ($MB_{Tz\text{-}TCO\text{-}antiVEGFR2}$)	M1	1049	729	496
	M2	601	435	289
	M3	700	475	394
	M4	402	305	219
	M5	916	677	620
	M6	796	461	386
AVERAGE		**744.00**	**513.67**	**400.67**
Pre-targeting Strategy (MB_{Tz} + TCO-antiVEGFR2)	M1	627	424	312
	M2	369	256	177
	M3	461	392	238
	M4	480	434	287
	M5	284	256	174
	M6	295	256	184
AVERAGE		**419.33**	**336.33**	**228.67**
Conventional (MB_V= $MB_{Biotin\text{-}antiVEGFR2}$)	M1	1167	433	168
	M2	1019	564	286
	M3	644	390	149
	M4	1009	393	186
	M5	561	335	141
	M6	545	340	144
AVERAGE		**824.17**	**409.17**	**179.00**

A plot of the US signal intensity (which correlates to number of MBs within the imaging window) over time during the destruction replenishment sequence for MB_{Tz}, $MB_{Tz\text{-}TCO\text{-}antiVEGFR2}$ and MB_V was created (Figure 6.5). Although the peak signal enhancement from all the MBs was relatively similar, lower post-burst signal when using MB_V compared to the other evaluated MBs constructs was observed (Figure 6.5). This indicated that even when the amount of bound and circulating MBs between the three conjugates was relatively the

same, the amount of replenished MB_V was significantly less. Such observation suggests that MBs loaded with biotin-antiVEGFR2 clear differently than the other MBs conjugates (MB_{Tz}, $MB_{Tz\text{-}TCO\text{-}antiVEGFR2}$). This suggested that the original US imaging sequence was not optimal to assess the extent of MB_{Tz} binding and that a new targeted US imaging sequence was needed.

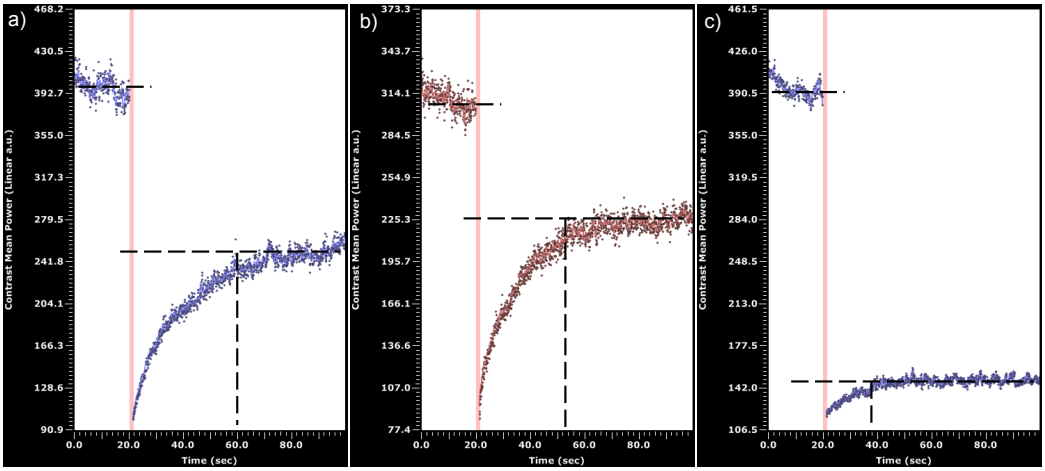

Figure 6.5 A plot of the change in US signal intensity within the imaging window (the tumour) over time during the differential targeted enhancement sequence. **a)** Signal enhancement monitoring at 4 min after injection of MB_{Tz}, **b)** Signal enhancement monitoring at 4 min after injection of $MB_{Tz\text{-}TCO\text{-}antiVEGFR2}$ and **c)** signal enhancement monitoring at 4 min after injection of MB_V. $MB_{Tz\text{-}TCO\text{-}anti\text{-}VEGFR2}$= MB_{Tz} incubated with TCO-anti-VEGFR2 for 20 min; MB_V= MB_C incubated with biotin-anti-VEGFR2 for 20 min.

6.1.2.3 Development of the new US Image Acquisition Sequence

Before developing the new sequence, there was a need to determine the clearance rate of MBs conjugates in order to choose the optimal time to initiate the differential targeted enhancement sequence. MBs clearance within the

imaging window (the tumour) was assessed and compared to streptavidin-coated MBs (MB_C) using US. Each mouse (n= 2 per study) was injected with MB_C and the decrease in US signal enhancement (i.e. number of MBs) over time (6 min) was monitored. Following MB_C, either $MB_{Tz\text{-}TCO\text{-}antiVEGFR2}$ or MB_V was tested and a plot of the change of US signal enhancement over time was created. A steep decrease in the US signal (i.e. decrease in circulating MBs) when monitoring MB_V compared to non-conjugated MBs (MB_C) or MB_{Tz} pre-loaded with TCO-antiVEGFR2 ($MB_{Tz\text{-}TCO}$) was observed (Figure 6.6a). Furthermore, MB_C and $MB_{Tz\text{-}TCO}$ had similar clearance rates (Figure 6.6a). The percentage of residual US signal enhancement using each MBs conjugate was calculated by dividing the US signal enhancement at the end of the plot over the US signal enhancement at a specific time point after injection of MBs (Figure 6.6a, red dashed line). After 6 min of MBs injection, the amount of MBs left circulating were 85%, 80% and 45% for MB_C, $MB_{Tz\text{-}TCO}$ and MB_V respectively (Figure 6.6b). This suggests that in order for the circulating MBs to not significantly interfere with the quantification, the US image acquisition should be initiated at a time at which the number of MBs is decreased by at least 50%.

Based on this goal, clearance of MB_{Tz} over 25 min was assessed to determine the optimal time to initiate the US sequence. Lewis Lung Carcinoma models were injected with MB_{Tz} via the tail vein and US signal enhancement in the tumour was monitored for 25 min. The monitoring was conducted every 6.25

min until 25 min and the same study was performed with MB_C for comparison. Looking at the plot of the US signal enhancement over time, similar clearance rate of MB_{Tz} and MB_C were found (Figure 6.7). The plot was then used to determine the optimal time when the amount of circulating MBs was reduced by half. Based on the graph, 24 min was found to be the optimal time to initiate the US image acquisition sequence. Based on those experiments, a new differential targeted enhancement US sequence was developed to image using MB_{Tz} (Figure 6.8).

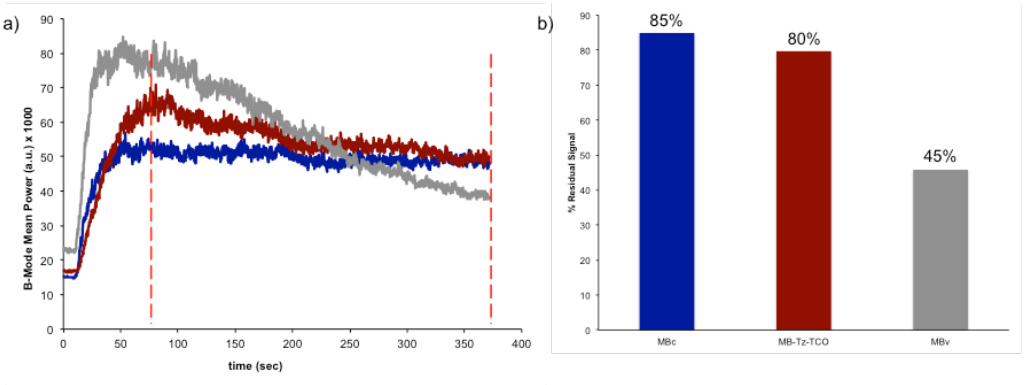

Figure 6.6 a) Monitoring the change in US signal intensity (i.e. number of MBs) within the field of view (the tumour) over time upon bolus injection of streptavidin coated MBs (MB_C, blue), MB_C loaded with biotin-Tz and TCO-antiVEGFR2 ($MB_{Tz\text{-}TCO}$, maroon) and MB_C loaded with biotin-antiVEGFR2 (MB_V, grey); **b)** Percentage residual US signal enhancement (i.e. number of MBs) after 6 min of administering MBs via the tail vein. Red dashed line in (a) represents the time point chosen to quantify the US signal. MB_C= unmodified MBs; $MB_{Tz\text{-}TCO}$= MB_{Tz} incubated with TCO-anti-VEGFR2 for 20 min; MB_V= MB_C incubated with biotin-anti-VEGFR2 for 20 min.

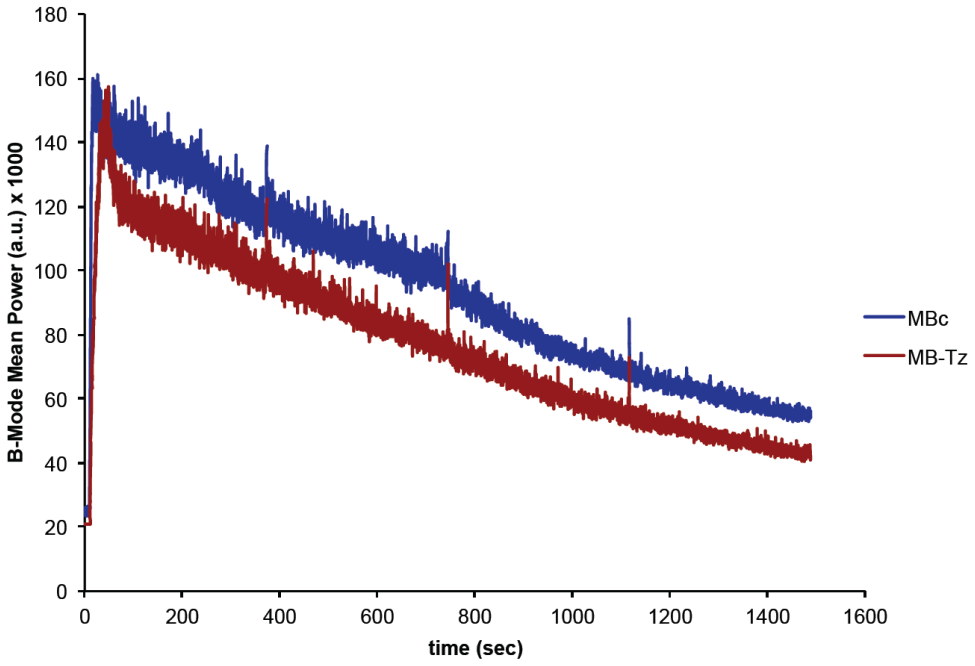

Figure 6.7 Monitoring the change in US signal intensity (i.e. number of MBs) within the field of view (the tumour) over time upon bolus injection of streptavidin coated MBs (MB_C, blue) and MB_C loaded with biotin-Tz (MB_{Tz}, maroon). Monitoring was conducted in 6.25 min sessions for 4 times (total monitoring time = 25 min).

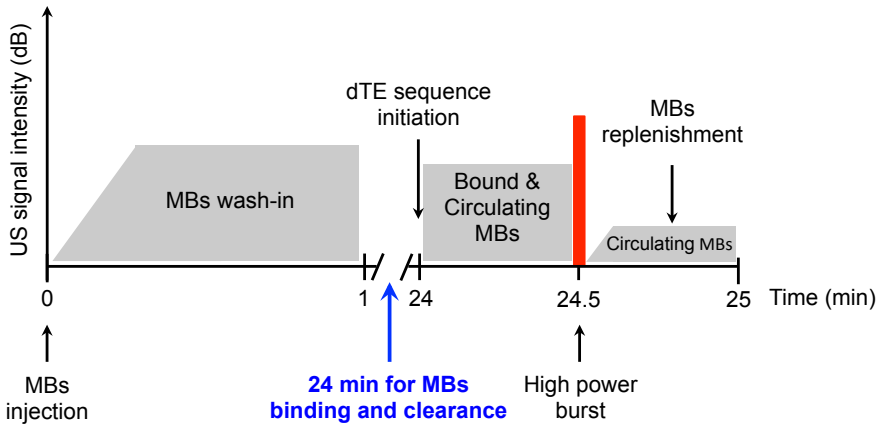

Figure 6.8 Revised US image acquisition sequence. MBs are injected and allowed

to bind to the target and clear from circulation for 24 min before initiating the destruction replenishment sequence (dTE).

6.1.2.4 In vivo US imaging of VEGFR2 using the new acquisition sequence

The newly developed US image acquisition sequence was used to reevaluate the direct and pre-targeting strategy using MB_{Tz}. As a control, each mouse (n= 2) was imaged with MB_C, which were allowed to clear before evaluating either of the targeting strategies within the same plane of view. Briefly, MBs were injected and allowed to bind and clear for 24 min before initiating the destruction replenishment sequence. In the pre-targeting strategy, mice (n= 2) were injected with TCO-antiVEGFR2 (100 μg, 200 μL) 24 hr before imaging study. Parametric images and quantified US signal enhancement were analyzed as previously described.[2]

Looking at the parametric US images, we find that qualitatively higher signal enhancement was observed using both the direct targeting strategy (Figure 6.9) and pre-targeting strategy (Figure 6.10) compared to non-conjugated MBs (MB_C). When quantifying the US signal enhancement, ~2 fold and 2.5 fold increase in the signal enhancement was observed when using the direct and pre-targeting strategy respectively (Figure 6.11). In this evaluation, the pre-targeting strategy did have higher signal enhancement than the direct strategy but a study with higher number of animals is needed to determine if the difference is statistically significant.

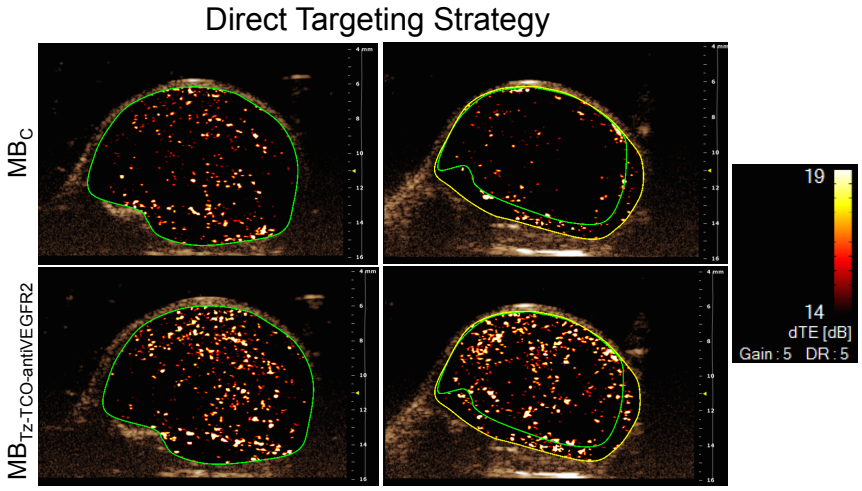

Figure 6.9 Transverse color-coded parametric nonlinear contrast mode ultrasound images of Lewis Lung Carcinoma mouse tumour model (VEGFR2(+)). Images were acquired 24 min after intravenous administration of non-conjugated MBs (MB_C, top), followed by another imaging session 24 min after intravenous administration of MB_C loaded with biotin-Tz and TCO-antiVEGFR2 ($MB_{Tz\text{-}TCO\text{-}antiVEGFR2}$, bottom) in the same mouse and the same plane of view. Each column represents a mouse (n= 2) and region of interest was based on the vascularity of the tumours determined from the initial distribution of the MBs following injection. dTE = differential targeted enhancement.

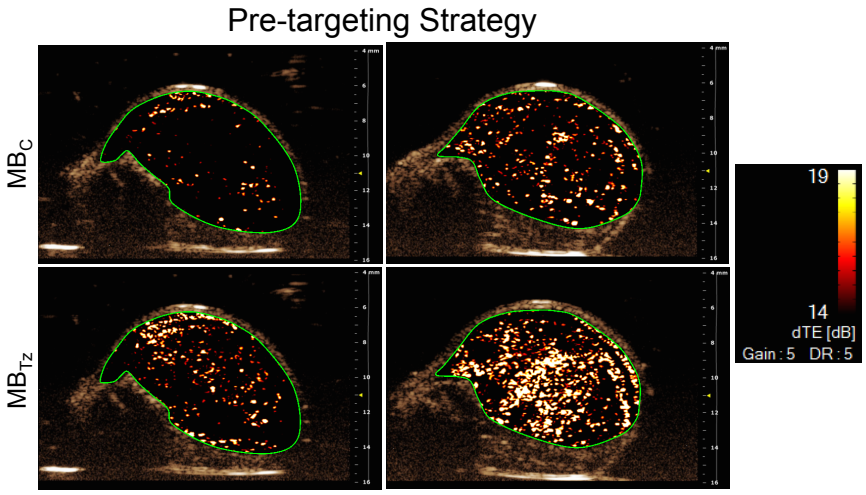

Figure 6.10 Transverse color-coded parametric nonlinear contrast mode ultrasound images of Lewis Lung Carcinoma mouse tumour model (VEGFR2(+)) pre-administered with TCO–antiVEGFR2 24 hr before imaging. Images were acquired 24 min after intravenous administration of non-conjugated MBs (MB_C, top), followed by another imaging session 24 min after intravenous administration of MB_C loaded with biotin-Tz (MB_{Tz}, bottom) in the same mouse and the same plane of view. Each column represents a mouse (n= 2) and region of interest was based on the vascularity of the tumours determined from the initial distribution of the MBs following injection. dTE= differential targeted enhancement.

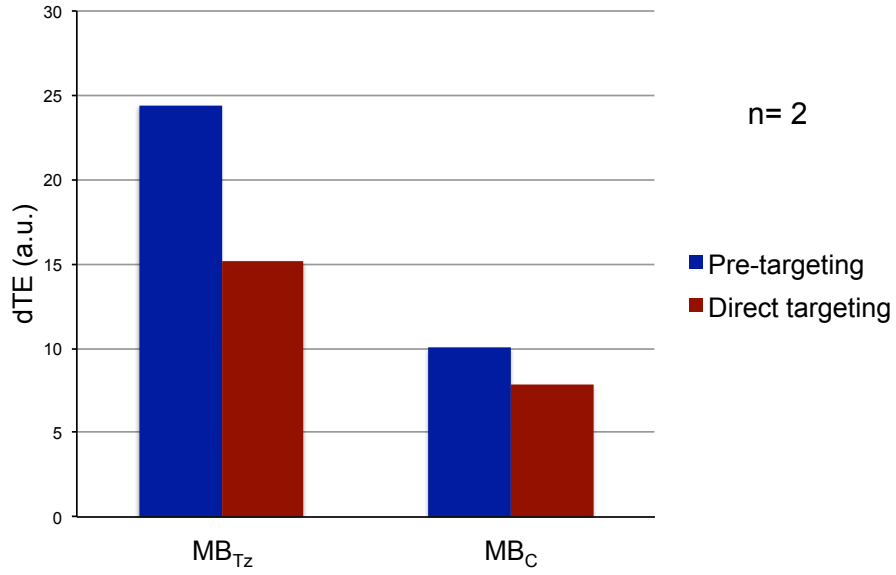

Figure 6.11 Quantitative analysis of the differential targeted enhancement (dTE) signal obtained from the ultrasound images. **Blue:** dTE signal quantified from the pre-targeting strategy evaluation and **maroon:** dTE signal quantified from the direct targeting strategy evaluation. MB_C: streptavidin coated MBs, MB_{Tz}: MB_C loaded with biotin-Tz; n= 2 per evaluation.

6.2 The development and evaluation of Tz- and TCO- functionalized gas vesicles as potential targeted US contrast agents

6.2.1 Introduction

With the new sequence in hand, which will in future be used with targeted MB_{Tz} based systems, focus shifted to other classes of US contrast agents that could exploit the Tz-TCO chemistry. Because of the known limitations of MBs as US contrast agents, which is largely due to their size and limited *in vivo* stability, there is an increasing interest in nano-sized echogenic agents with improved *in vivo* stability. One example are gas vesicles (GVs) which are produced by aquatic bacteria to help control their buoyancy for ideal access to nutrients and light.[3,4]

Genetically encoded GVs that are produced in Halobacteria are biconical in shape, 45-250 nm in width and stabilized by a 2 nm protein shell.[4] One unique aspect of these GVs is their shell's permeability to gas,[3] making them less pressure sensitive and more stable than MBs.[5] Furthermore, Shapiro and coworkers have demonstrated that these GVs are echogenic and have US enhancing properties both *in vitro* and *in vivo*.[5] Because of their echogenicity, small size and higher stability, this class of GVs can be imaged for longer periods of time and can be used to access biomarkers beyond the vasculature. The latter would require the development of new targeting strategies.

The amine groups in the protein shell of GVs provide a site for functionalization using TCO-NHS and Tz-NHS amide coupling chemistry. The long shelf life of these GVs in solution (up to one month) make them suitable for surface modification and preclinical *in vitro* and *in vivo* studies. The initial focus was to prepare TCO-conjugated GVs (TCO-GVs) and label with a ^{99m}Tc-Tz derivative developed by Holly Bilton from our group. These experiments were performed to determine the feasibility of modifying the surface of this class of contrast agents and to assess the hitherto unknown *in vivo* distribution of GVs using *ex vivo* tissue gamma counting and SPECT-CT imaging. As a complement to the TCO-GVs, Tz-derivatized GVs were also developed by Lili Southcott, a 4th year thesis student in our group under my supervision. Only the TCO derivatives are described here.

6.2.2 Results and Discussion[§]

TCO-conjugated GVs (TCO-GVs) were prepared by adding excess of an activated TCO (TCO-NHS) to GVs at pH 8. The solution was left mixing in a shaker for 2.5 hr and TCO-GVs were purified by dialysis and concentrated using centrifugal flotation (Figure 6.12). ^{99m}Tc-labeling of GVs was performed by taking advantage of the fast and selective reaction between Tz and TCO. First, a tridentate chelate derivative of tetrazine **1** was synthesized, fully characterized and labeled with ^{99m}Tc in 45% radiochemical yield (^{99m}Tc-Tz, compound **3b**). The purity and identity of **3b** was determined by HPLC through co-injection with the fully characterized rhenium derivative **3a** as a reference standard (Scheme 6.1 B).

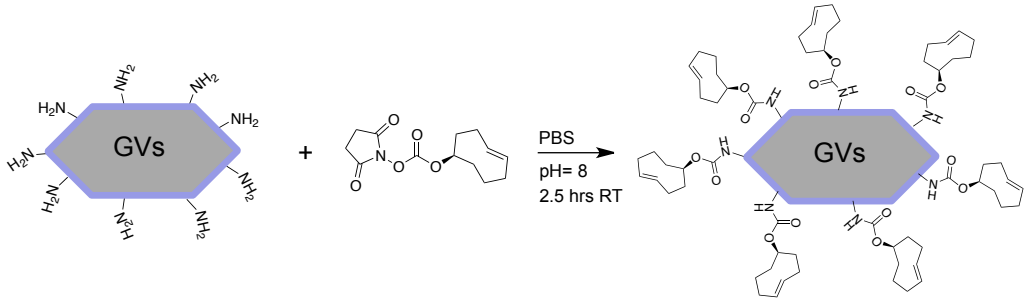

Figure 6.12 Representation of the chemistry used to prepare TCO-conjugated GVs

[§] This manuscript is under preparation for submission to the journal of Ultrasound in Medicine and Biology. I was responsible for developing the TCO-conjugated GVs and preparing the ^{99m}Tc-labeled GVs. Holly Bilton was responsible for developing and characterizing the precursor, the Re standard and ^{99m}Tc-labeled Tz derivative. Melissa Yin prepared and provided the GVs and Johann Le Floc'h is leading the project and conducting all the SPECT-CT imaging experiments.

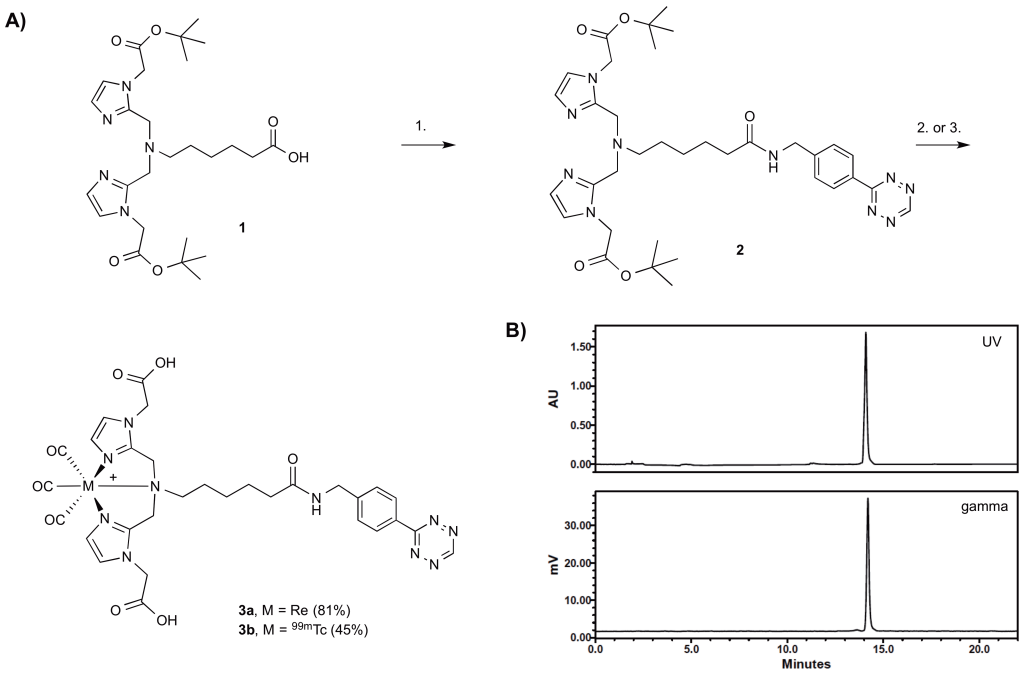

Scheme 6.1 A) Synthesis of tetrazine-Tc(I) and Re(I) complexes 3a and 3b respectively. **1.** PyBOP, DIPEA, DMF, ((4-tetrazine-3-yl)phenyl)methanamine hydrochloride, rt, 12 h **2.** (i) $[Re(CO)_3(H_2O)_3]Br$, CH_3CN, MW, 60 °C, 20 min. (ii) TFA, DCM 60 °C (MW), 6 min. **3.** (i) $[^{99m}Tc(CO)_3(H_2O)_3]^+$, MeOH, saline, 60 °C (MW), 20 min. (ii) TFA, DCM, 60 °C (MW), 6 min. **B)** HPLC chromatograms (UV and γ) of 3a (**top**) co-injected with 3b (**bottom**).

Compound **3b** was then introduced to the solution of TCO-GVs at room temperature and left shaking for 30 min. ^{99m}Tc-labeled GVs (^{99m}Tc-GVs) were then washed with PBS and purified from any residual **3b** using centrifugal flotation (Figure 6.13). As a quality control, a sample of the mixture was taken before and after purification, sonicated and injected into a HighTrap size-exclusion cartridge attached to an HPLC (Figure 6.14). The gamma trace of the crude mixture showed two broad peaks, one representing ^{99m}Tc-GVs (R_t= ~ 2

min) while the other is free ^{99m}Tc-Tz (**3b**, R_t= ~ 6 min). After purification, HPLC (gamma) exhibited one peak where the desired product was isolated in 59% radiochemical yield (RCY).

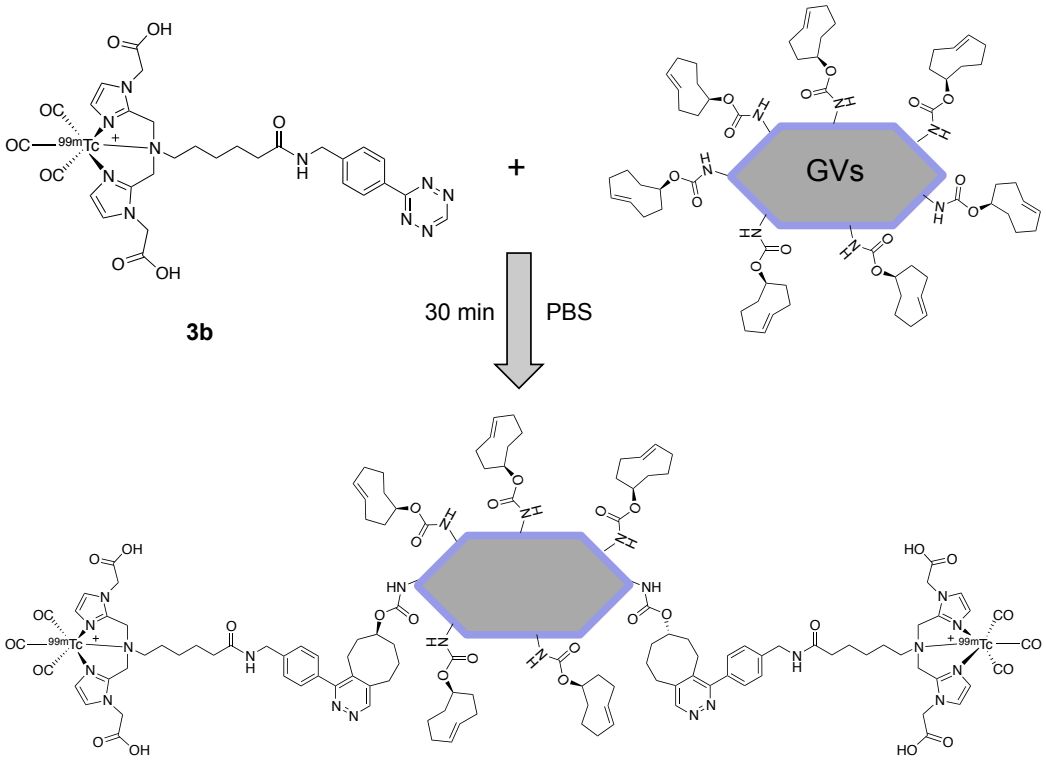

Figure 6.13 Representation of the chemistry used to label TCO-GVs with compound **3b**.

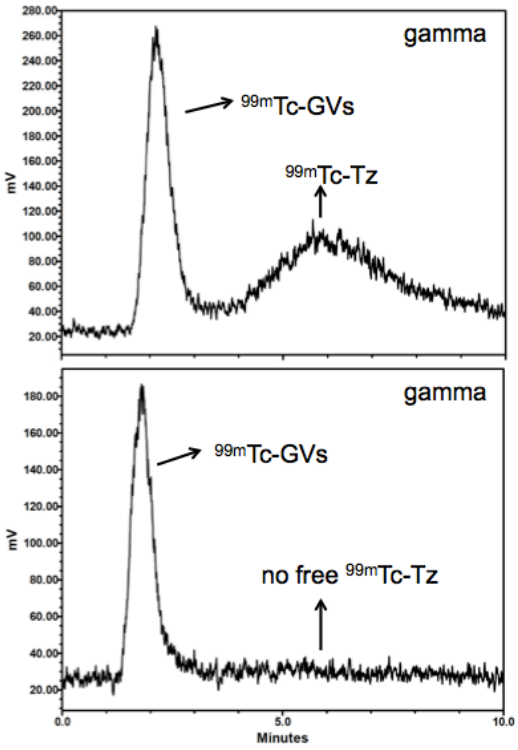

Figure 6.14 Analysis of ^{99m}Tc-labeled GVs using a HiTrap size-exclusion cartridge attached to an HPLC (γ-detection). **Top:** γ-Trace of crude reaction mixture containing ^{99m}Tc-GVs and free ^{99m}Tc-Tz; **bottom:** γ-trace of ^{99m}Tc-GVs after centrifugal flotation purification.

In vivo distribution of ^{99m}Tc-GVs was evaluated by *ex vivo* tissue counting following necropsy and dynamic SPECT/CT imaging. For the tissue counting study, ^{99m}Tc-GVs were injected in healthy mice before sacrificing the animals at 5, 20, 60 and 120 min. The amount of activity in each organ was measured in a gamma counter and normalized to the weight of the organ (n= 3 per time point). The percent-injected dose per gram (%ID/g) plot was produced showing initial accumulation of ^{99m}Tc-GVs in the gall bladder, liver, lung, spleen and urine

bladder (Figure 6.15). ^{99m}Tc-GVs accumulation in the small intestine increased while a decrease was observed in the previously mentioned organs over time. As expected, these GVs clear through the reticuloendothelial system (RES), which is commonly associated with comparable nanoparticles. *In vivo* dynamic SPECT/CT imaging scans further confirm the previous observations. ^{99m}Tc-GVs uptake (in %ID/cc) was observed in the liver (42%), spleen (27%), duodenum (15%), stomach (2%) and bladder (15%). GVs were rapidly and consistently taken-up in the liver, reaching a plateau within 60 sec and then decreasing slightly after 30 min. In contrast, duodenum uptake was only observed after 20 min (Figure 6.16).

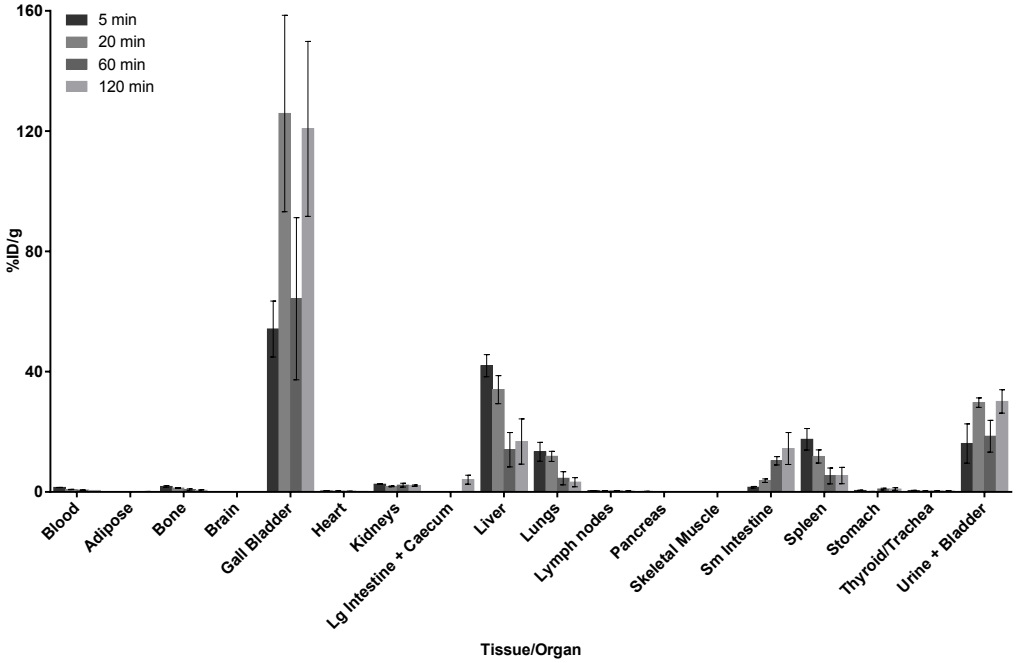

Figure 6.15 Bar graph representation of *in vivo* biodistribution of ^{99m}Tc-GVs in CD1 mice. Mice were sacrificed at 5 min, 20 min, 60 min and 120 min post-injection. Data are expressed as percent injected dose per gram of tissue/fluid

(%ID/g) (n= 3 per time point).

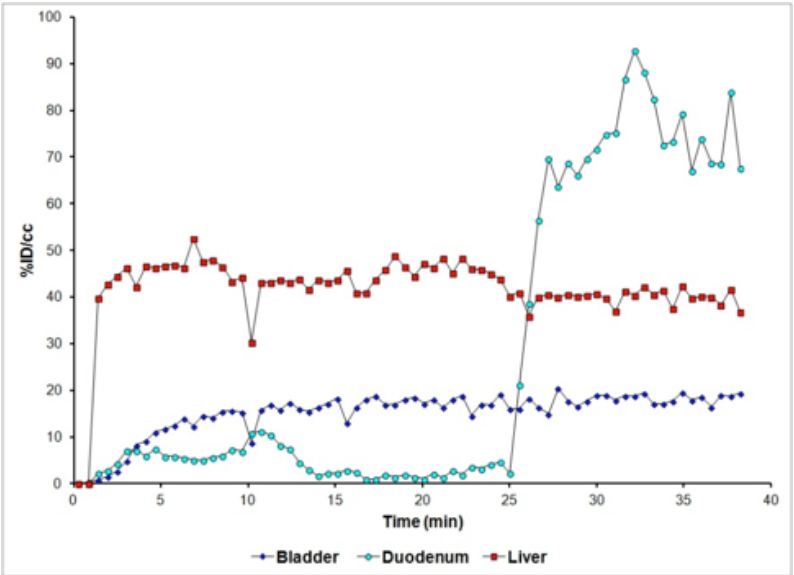

Figure 6.16 Time activity curves (TACs) showing the uptake of ^{99m}Tc-GVs in mouse organs (bladder, duodenum and liver) over time.

6.2.3 Conclusion

The ability to modify the surface of GVs by taking advantage of the Tz-TCO reaction was demonstrated. Using this approach, GVs were labeled with ^{99m}Tc and quantitative biodistribution data obtained for the first time. Similar *in vivo* studies in tumour bearing mice to evaluate the feasibility of these GVs to accumulate in the tumour through enhanced permeability and retention effect (EPR) are planned. Having established an easy and translatable platform to derivatize GVs, future work will also include adding groups (e.g. PEG spacers) to reduce RES sequestration. Once successful, the translation of the modified GVs in targeted US imaging will be evaluated on previously studied targets (i.e.

VEGFR2, PSMA and uPAR). The ability of these GVs to extravasate will expand the utility of targeted US molecular imaging.

6.2.4 Experimental

6.2.4.1 Synthesis of compound 1, 2, 3a and 3b:

The synthesis and characterization of compounds **1**, **2**, **3a** and **3b** were accomplished by Holly Bilton from the Valliant research group and reported in a published meeting abstract.[6]

6.2.4.2 Gas vesicle (GVs) preparation and purification:

GVs were produced in Halobacteria salinarum NRC-1 (Halo, Carolina Biological Supply, Burlington, NC) and purified by centrifugal assisted flotation following a previously reported literature procedure.[5] The GVs were provided by Melissa Yin from Dr. Stuart Foster's group at Sunnybrook Research Institute in Toronto.

6.2.4.3 Preparation of TCO-conjugated Halo GVs:

(E)-Cyclooct-4-enyl-2,5-dioxopyrrolidin-1-yl carbonate (TCO-NHS) (855.1 µg, 3.2 µmol; Click Chemistry Tools, 1016-100) in DMSO (197.3 µL) was added to a solution of GVs (OD_{500nm}= 55.2, 1.8 mL) in PBS and incubated for 2.5 hr at room temperature on a shaker. The TCO-GVs were then purified from excess TCO-NHS using a dialysis kit (Spectra/Por 1 Dialysis Tubing, 132645; 6-8 kDa MWCO) overnight at 4 °C and concentrated to the original volume using

centrifugal flotation at 300 rcf for 15 min.

6.2.4.4 ^{99m}Tc-labeling of TCO-GVs:

Compound **3b** (774 μCi, 29 MBq, 100 μL) in PBS was added to TCO-GVs (OD_{500nm}= 50, 400 μL) and incubated for 30 min at room temperature on a shaker (Figure 6.13). Using centrifugal flotation at 300 rpm and washing with PBS excess compound **3b** was removed (2×). For quality control, a sample of both the crude and purified mixture was sonicated and injected in a HiTrap size exclusion column attached to a gamma detector. The column was eluted with 100 mM ammonium bicarbonate in water at 1 mL/min flow rate (Isocratic elution 0-8 min 100%). The peak representing ^{99m}Tc-GVs eluted at ~2 min and peak representing free compound **3b** eluted at ~6 min (Figure 14). RCY= 59%

6.2.4.5 Animal Studies

All animal studies were approved by the Animal Research Ethics Board at McMaster University. Mice were maintained under clean conditions in an established animal facility with 12 hour light/dark cycles and given food and water ad libitum.

6.2.4.6 In vivo biodistribution study in healthy mice

Biodistribution studies were performed on female, 5-6 week old, CD1 mice ordered from Charles River Laboratory (Kingston, NY). Mice were injected with approximately 0.4 MBq of ^{99m}Tc-GVs. At 5 min, 20 min, 60 min and 120 min post-injection (n= 3 per time point), mice were anesthetized with 3%

isoflurane and euthanized by cervical dislocation. Blood, adipose, bone, brain, gall bladder, heart, kidneys, large intestine and caecum (with contents), liver, lungs, lymph nodes (axillary and brachial), pancreas, skeletal muscle, small intestine (with contents), spleen, stomach (with contents), thyroid/trachea, urine + bladder and tail were collected, weighed and counted in a Perkin Elmer Wizard 1470 Automatic Gamma Counter. Decay correction was used to normalize organ activity measurements to time of dose preparation for data calculations with respect to injected dose (i.e. %ID/g) (Figure 6.15, Table 6.2).

Table 6.2 Tissue distribution of ^{99m}Tc-nGVs in CD1 mice

	Time (min)			
Organs	5	20	60	120
Blood	1.51 ± 0.02	0.83 ± 0.04	0.59 ± 0.03	0.50 ± 0.01
Adipose	0.13 ± 0.01	0.10 ± 0.00	0.06 ± 0.01	0.14 ± 0.03
Bone	1.85 ± 0.28	1.33 ± 0.08	0.71 ± 0.34	0.54 ± 0.25
Brain	0.03 ± 0.00	0.02 ± 0.00	0.01 ± 0.00	0.01 ± 0.00
Gall Bladder	54.20 ± 9.30	125.87 ± 32.69	64.26 ± 26.98	120.75 ± 29.09
Heart	0.36 ± 0.03	0.27 ± 0.03	0.22 ± 0.02	0.19 ± 0.02
Kidneys	2.61 ± 0.08	1.85 ± 0.13	2.25 ± 0.64	2.08 ± 0.25
Lg Intestine + Caecum	0.08 ± 0.00	0.05 ± 0.00	0.07 ± 0.02	4.08 ± 1.51
Liver	42.00 ± 3.70	34.04 ± 4.66	14.05 ± 5.72	16.77 ± 7.50
Lungs	13.37 ± 3.14	11.85 ± 1.69	4.57 ± 2.18	3.26 ± 1.53
Lymph nodes	0.38 ± 0.04	0.35 ± 0.05	0.36 ± 0.06	0.30 ± 0.09
Pancreas	0.19 ± 0.06	0.10 ± 0.01	0.08 ± 0.01	0.12 ± 0.03
Skeletal Muscle	0.14 ± 0.01	0.11 ± 0.02	0.08 ± 0.01	0.08 ± 0.02
Sm Intestine	1.57 ± 0.27	3.74 ± 0.58	10.37 ± 1.41	14.45 ± 5.30
Spleen	17.52 ± 3.57	11.83 ± 2.19	5.34 ± 2.65	5.47 ± 2.71
Stomach	0.51 ± 0.10	0.17 ± 0.03	0.98 ± 0.29	1.00 ± 0.42
Thyroid/Trachea	0.48 ± 0.07	0.28 ± 0.03	0.27 ± 0.02	0.29 ± 0.05
Urine + Bladder	16.12 ± 6.54	29.70 ± 1.57	18.53 ± 5.30	30.12 ± 3.89

Data are expressed as %ID/g ± SEM

6.2.4.7 SPECT/CT imaging of ^{99m}Tc-GVs in healthy mice[**]

Dynamic whole body scans were performed on U-SPECT using a high energy collimator. Mice were anaesthetized with isoflurane (2-2.5% maintenance) and body temperature was maintained at 37 °C. Following dose calibration of ^{99m}Tc-GVs, a frame was acquired prior to its injection. Subsequent frames were then collected at frame rate raging from 30 to 70 sec for up to 90 min. Mice were then scanned *in vivo* with microCT (pixel size= 35 µm, keV, µA) to obtain anatomical details. For calibration of SPECT images, a 1 mL syringe filled with a solution of known activity of ^{99m}Tc-GVs in PBS was scanned. SPECT images were reconstructed (0.512 mm^3 voxelsize, 16 subsets, 15 iterations), corrected for decay, scattering and attenuation and calibrated. Images were then processed using the segmentation and 3D rendering tools in PMOD (PMOD Technologies Ltd). SPECT/CT experiments were performed using healthy mice (n= 5) and imaging studies were performed following injection in the tail vein of either intact or collapsed ^{99m}Tc-GVs (2.2-5.4 MBq, 90-130 µL, OD_{500nm}= 18).

[**] Provided by Dr. Johann Le Floc'h

6.3 References

[1] J. K. Willmann, R. Paulmurugan, K. Chen, O. Gheysens, M. Rodriguez-Porcel, A. M. Lutz, I. Y. Chen, X. Chen, S. S. Gambhir, *Radiology* **2008**, *246*, 508–518.

[2] A. Zlitni, N. Janzen, F. S. Foster, J. F. Valliant, *Angew. Chem. Int. Ed. Engl.* **2014**, *53*, 6459–6463.

[3] A. E. Walsby, *Microbiol. Rev.* **1994**, *58*, 94–144.

[4] F. Pfeifer, *Nat. Rev. Microbiol.* **2012**, *10*, 705–715.

[5] M. G. Shapiro, P. W. Goodwill, A. Neogy, M. Yin, F. S. Foster, D. V. Schaffer, S. M. Conolly, *Nat. Nanotechnol.* **2014**, *9*, 311–316.

[6] H. Bilton, Z. Ahmad, John F Valliant, *J. Label Compd. Radiopharm.* **2015**, *58*, S61.

7 Chapter 7: Summary and Future work

7.1 Summary

The overall objective was to develop a platform for the preparation of targeted and multi-modal US contrast agents. In Chapter 2, methods to prepare and characterize MBs labeled with the radioisotope ^{99m}Tc and/or a rhodamine dye were developed. The use of the signaling moiety on the MBs to characterize distribution, surface functionalization and loading capabilities were shown to be feasible. Various fluorescent assays were also developed to confirm functionalization of MBs. In the same chapter, means to prepare targeted multi-modal MBs were also investigated. Such approach depended on the ability to load two biotinylated ligands on the surface of streptavidin-coated MBs, one representing the signaling agent with the other being the targeting vector. This resulted in the development of a series of novel biotinylated derivatives of a PSMA inhibitor, which were evaluated in a PSMA binding assay. With this strategy, the first example of ^{99m}Tc-labled MBs targeted to VEGFR2 (a marker of angiogenesis) and PSMA (a marker for prostate cancer) *in vitro* were reported. Unfortunately, this approach was only able to target MBs *in vitro* but *in vivo* studies were not successful. Nevertheless, the platform to conjugate and purify MBs, the associated assays (flow chamber, fluorescent binding, loading study) and choice of optimal cells for *in vitro* and *in vivo* evaluation were utilized in the ultimately successful approach.

The initial strategies for MBs functionalization led to the creation of a new approach to target MBs for molecular US imaging applications. Such strategy was needed due to the cumbersome and long development pathways currently faced when developing targeted MBs using conventional approaches. The new strategy employed the bioorthogonal reaction between Tz and TCO. Tz-coated MBs (MB_{Tz}) were developed and targeted to the biomarker of interest either by directly attaching a TCO-antibody (direct targeting strategy) or by injecting TCO-antibody first, allowing the targeting construct to clear from circulation and non-target sites, followed by injection of MB_{Tz} (pre-targeting strategy). This thesis provides the first example of using bioorthogonal chemistry to localize micron-sized particles for molecular US imaging. The first target of interest was VEGFR2, a marker of angiogenesis widely evaluated using targeted US imaging providing a means to directly compare the new strategy to conventional methods (Chapter 3). MB_{Tz} was then targeted to PSMA-expressing cancer cells *in vitro* and *in vivo* using the direct and pre-targeting strategy (Chapter 4). Furthermore, *in vivo* analysis provided a comparison between using two different PSMA antibodies to target MB_{Tz} to PSMA. Finally, the new strategy was also evaluated to target MBs to a known marker of cancer, uPAR (Chapter 5). *In vitro* analysis showed the feasibility of targeting MBs to uPAR expressing cells unfortunately, *in vivo* studies proved unsuccessful.

Subsequent work focused on improving the arising US data by modifying

image acquisition parameters and applying the TCO-Tz chemistry to an emerging class of nano-US contrast agents (Chapter 6). To this end a new US image acquisition sequence was developed to better evaluate targeting of MB_{Tz} using the pre- and direct targeting strategy *in vivo*. In addition, the Tz-TCO platform was then translated to modify the surface of nano-sized GVs, as potential US contrast agents. This facilitated the labeling of TCO-modified GVs with ^{99m}Tc to study their biodistribution.

7.2 Future Work

7.2.1 Expanding the technology to develop targeted human-compatible MBs

Having established the effectiveness of targeting MBs to the site of disease using Tz-TCO chemistry, the next step is to adapt the approach to create targeted human compatible MBs. More specifically, means to develop Tz-coated MBs without the use of biotin-streptavidin interaction are necessary. One simple approach involves preparing a Tz-derivative of FDA approved US contrast agents. Because of the existing regulatory and manufacturing data, such route could potentially simplify the translation of the new constructs to the clinic.

In collaboration with GE Healthcare, two FDA approved US contrast agents have been obtained (Optison™ and Sonazoid™)(Table 1.2). Optison™ is a perflutren gas-filled MBs stabilized by a human serum albumin (HSA) shell. We hypothesize that the amine functional groups on HSA can provide an accessible

site for modification.[1][2] Briefly, Tz can be conjugated to the surface of formulated MBs through amide coupling chemistry. Surface functionalization will be first confirmed using fluorescent microscopy after incubating MB-Tz with a commercially available TCO-Cy5 dye. Targeting of the new construct to previously evaluated vascular markers *in vitro* and *in vivo* will be conducted as a proof of principle study.

Sonazoid™ is a perfluorobutane gas filled MBs stabilized by a phosphatidyl serine shell. Otani and coworkers have demonstrated the ability of targeting Sonazoid™ MBs to $\alpha_V\beta_3$ integrin *in vitro* by loading these MBs with lactadherin.[3] The C2 domain of lactadherin binds to phosphatidyl serine and its N-terminal domain binds to $\alpha_V\beta_3$ and $\alpha_V\beta_5$ integrin[4] (Figure 7.1). In order to translate our previously established platform to prepare Sonazoid™-coated Tz MBs, commercially available lactadherin can be coupled to Tz through amide coupling chemistry before loading on MBs. From the work reported by Otani and coworkers, loading Sonazoid™ with lactadherin did not affect its size or US properties.[3] Furthermore, they showed that the binding of lactadherin to Sonazoid™ MBs was strong enough to withstand vigorous shaking.[3] Although the lactadherin-Sonazoid™ construct was only evaluated *in vitro*, translating this agent to prepare Tz-coated MBs is promising.

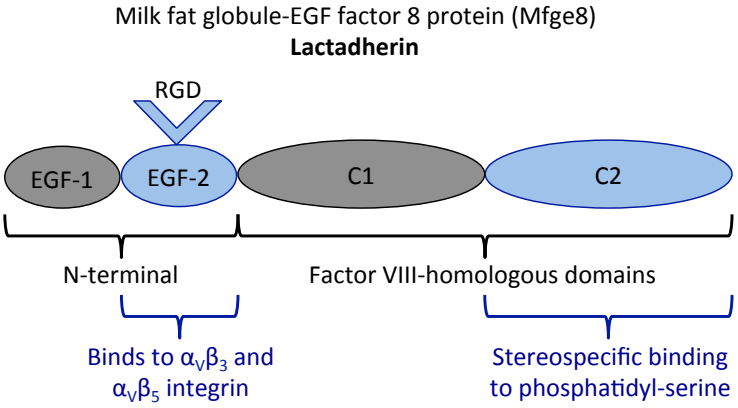

Figure 7.1 A schematic illustrating the structure of lactadherin

One major hurdle in the production of these two agents is the long processing time needed to prepare these Tz-coated MBs (more than 2 hr). In addition, having multiple purification steps will increase the chances of contamination and decrease the number of prepared MBs. This is why transforming this strategy to a stable and reproducible instant kit without the need for purification will be crucial to facilitate its translation into the clinic.

As mentioned in section 1.4.4, after more than two decades of research on developing targeted US contrast agents, only one is in clinical trials (BR55, specific to VEGFR2). We believe that developing human-compatible Tz-coated MBs would provide a single agent that can be easily translated to different targets just by changing the TCO-conjugated antibody, thus simplifying the route to evaluate other markers of disease using targeted molecular US imaging.

7.2.2 MBs as shuttles for drug and imaging probe delivery

When combining MBs with high intense focused US (HIFU), higher vascular and cellular membrane permeability is observed (sonoporation).[5,6] There is therefore increased interest in using MBs as vehicles for delivery of drugs and molecular imaging probes. Such strategy provides better means to deliver less stable therapeutics or compounds with poor pharmacokinetic properties to the site of interest.[5,6] Furthermore, the combination of MBs with HIFU has been shown to temporarily disrupt the blood brain barrier, a major hurdle in developing therapeutics for central nervous system disorders (CNS), allowing for delivery of therapeutics into the CNS.[7-10] Another advantage of using MBs as shuttles is the potential reduction of drug side effects by preventing their interaction with other sites in the body.[5,6]

The chemistry developed during the course of the work presented in this thesis offers different means to load drugs on to US contrast agents. The developed Tz-coated contrast agents can be loaded with small molecule, biological, or nanoparticle- based pharmaceuticals on the surface using the inverse electron demand Diels-Alder reaction. One potential nano-carrier that can be linked to MBs are pluronic F127-based micelles. Pluronic F127 has a temperature sensitive critical micelle concentration (CMC), resulting in its conversion to monomers once the temperature is lowered.[11] However in the presence of a hydrophobic compound, pluronic F127 produces kinetically robust micelles

(Figure 7.2).[12] "Frozen" micellar naphtallocyanines were used previously by Zhang and coworkers for multi-modal functional imaging of the intestine. The micelles were shown to be stable in the gut and effective as imaging agents for photoacoustic and PET imaging.[12] Based on those studies, Tz-functionalized pluronic F127 (Tz-F127) can be prepared (Scheme 7.1) and used to form frozen micelles in the presence of a hydrophobic therapeutic or imaging agent. Finally, those micelles can be loaded on TCO-conjugated US contrast agent for drug delivery using sonoporation.

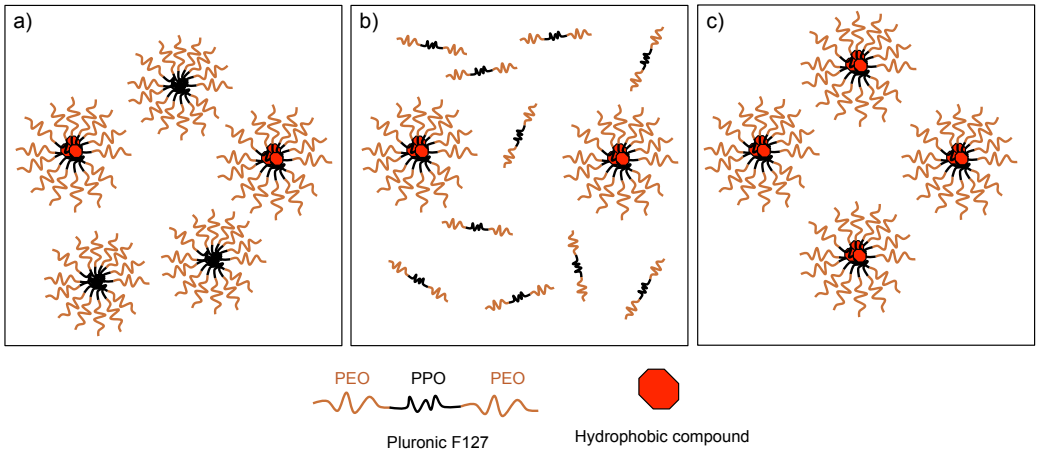

Figure 7.2 A schematic illustrating the preparation and purification of frozen micelles (adapted from Zhang and coworkers).[12] **a)** Formation of pluronic F127 micelles in the presence of a hydrophobic compound resulting frozen micelles and unloaded micelles, **b)** decreasing the temperature to 4 °C resulted in forming monomers of the unloaded micelles and **c)** purified frozen micelles with no presence of unloaded micelles. PEO: polyethylene oxide, PPO: polypropylene oxide.

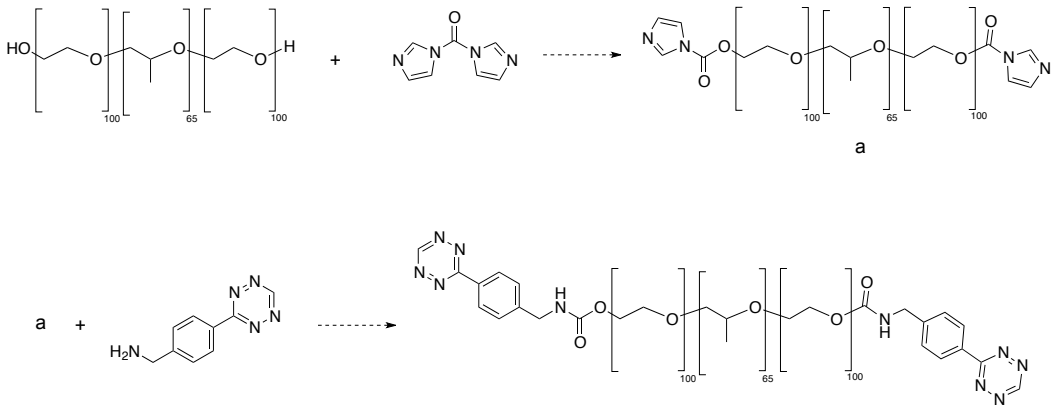

Scheme 7.1 Proposed scheme for preparation of Tz-functionalized Pluronic F127. The amine functionalized Tz used can be replace by any other derivatives of Tz. The first step of this scheme is adapted from Zhang and coworkers.[13]

7.3 References

[1] R. J. Williams, M. Lipowska, G. Patonay, L. Strekowski, *Anal. Chem.* **1993**, *65*, 601–605.

[2] A. Becker, B. Riefke, B. Ebert, U. Sukowski, H. Rinneberg, W. Semmler, K. Licha, *Photochem. Photobiol.* **2000**, *72*, 234–241.

[3] K. Otani, K. Yamahara, *Mol. Imaging Biol.* **2013**, *15*, 534–541.

[4] R. Hanayama, M. Tanaka, K. Miwa, A. Shinohara, A. Iwamatsu, S. Nagata, *Nature* **2002**, *417*, 182–187.

[5] S. Tinkov, R. Bekeredjian, G. Winter, C. Coester, *J. Pharm. Sci.* **2009**, *98*, 1935–1961.

[6] F. Kiessling, S. Fokong, J. Bzyl, W. Lederle, M. Palmowski, T. Lammers, *Adv. Drug Deliv. Rev.* **2014**, *72*, 15–27.

[7] C.-Y. Lin, H.-Y. Hsieh, W. G. Pitt, C.-Y. Huang, I.-C. Tseng, C.-K. Yeh, K.-C. Wei, H.-L. Liu, *J. Control. Release* **2015**, *212*, 1–9.

[8] J. Park, Y. Zhang, N. Vykhodtseva, F. A. Jolesz, N. J. McDannold, *J. Control. Release* **2012**, *162*, 134–142.

[9] K. F. Timbie, B. P. Mead, R. J. Price, *J. Control. Release* **2015**, *219*, 61–75.

[10] K. Hynynen, *Adv. Drug Deliv. Rev.* **2008**, *60*, 1209–1217.

[11] P. Chandaroy, A. Sen, P. Alexandridis, S. W. Hui, *Biochim. Biophys. Acta* **2002**, *1559*, 32–42.

[12] Y. Zhang, M. Jeon, L. J. Rich, H. Hong, J. Geng, Y. Zhang, S. Shi, T. E. Barnhart, P. Alexandridis, J. D. Huizinga, et al., *Nat. Nanotechnol.* **2014**, *9*, 631–638.

[13] W. Zhang, Y. Shi, Y. Chen, J. Ye, X. Sha, X. Fang, *Biomaterials* **2011**, *32*, 2894–2906.

APPENDIX I

Supporting Information for Chapter 3

Materials, Instruments and General Information

All chemicals and reagents for synthesis were purchased from Sigma-Aldrich, EMD chemicals, Toronto Research Chemicals and Bachem and were used without further purification. Compounds **2**,[2] **3**[3] and **4**[4] were prepared following literature procedures. Solvents were purchased from Caledon and dried using a Pure-Solv system (Innovative Technology). Microbubbles (MBs) were obtained using MicroMarker™ Target-Ready Contrast Agent Kit (VisualSonics Inc., Toronto, Canada; 8.4×10^8 MBs/vial).[1] Streptavidin coated magnetic beads (New England BioLabs) and MACSiMAG™ Separator (MiltenyiBiotec) magnet were used during the purification of MBs. ^{1}H and ^{13}C NMR spectra were measured on a Bruker Avance AV-600 spectrometer (^{1}H = 600.13 MHz, ^{13}C = 150.90 MHz). ^{1}H and ^{13}C NMR chemical shifts are expressed in parts per million (ppm) while coupling constants are expressed in Hertz (Hz). Low-resolution mass spectra were obtained on an Agilent 630 ion trap electron spray ionization (ESI) instrument, using a 1200 series LC system eluting with H_2O:MeOH (1:1). High-resolution mass spectra (HRMS) were obtained using a Waters Micromass Global Ultima Q-TOF in ESI mode. Conjugated-antibodies were analyzed on a MALDI Bruker Ultraflextreme Spectrometer. HPLC (analytical and semi-preparative) was performed on a Varian Pro Star model 330 PDA detector monitoring at 254 nm

with a model 230 delivery system. For analysis of compounds, a Phenomenex Synergi Polar-RP 80Å column (4 μm, 4.6 × 250 mm) was used, eluting at a flow rate of 1.0 mL/min. For semi-preparative HPLC, a Phenomenex Synergi Polar-RP 80Å column (4 μm, 10.0 × 250 mm) was used, eluting at a flow rate of 4.0 mL/min. HPLC method 1: Solvent A = 0.1% trifluoroacetic acid (TFA) in water; Solvent B = 0.1% TFA in acetonitrile: gradient elution, 5% B at injection, 39% B (0-8 min), 95% B (8-11 min), 95% B (11-18 min), 5% B (18-19 min), 5% B (19-21 min). MBs size and concentration were determined using Z2 Coulter counter (Beckman Coulter, Fullerton, California).

Synthesis of *N*-(4-(1,2,4,5-tetrazin-3-yl)benzyl)-6-(5-((4*S*)-2-oxohexahydro-1*H*-thieno[3,4-*d*]imidazol-4-yl)pentanamido)hexanamide (5)

(4-(1,2,4,5-Tetrazin-3-yl)phenyl) methanamine hydrochloride (6.2 mg, 0.033 mmol) was dissolved in dry DMF (1 mL) containing TEA (0.033 mL, 0.24 mmol) and added to a solution of dry DMF (2 mL) containing **4** (25 mg, 0.049 mmol). The mixture was stirred at room temperature under argon for 1 hour before removing the solvent by rotary evaporation and drying the resulting pink solid under vacuum overnight. The solid was subsequently dissolved in a mixture of MeOH:DCM and purified by semi-preparative HPLC (R_t = 13.9 min). The product was isolated as a pink solid (13 mg, 75%). HRMS (ESI+) m/z for $C_{25}H_{34}N_8O_3S$: calculated 527.2553, observed 527.2527. ^{1}H NMR (DMSO-*d6*, 600 MHz): δ 10.58 (s, 1H), 8.46 (d, 2H, *J*= 8.4), 8.44 (t, 1H, *J*= 6.0), 7.74 (t, 1H, *J*=

6.0), 7.53 (d, 2H, *J*= 8.4), 6.41 (bs, 2H), 4.39 (d, 2H, *J*= 6.0), 4.30 (dd, 1H, J_A= 4.8, J_B= 7.8), 4.12 (dd, 1H, J_A= 4.8, J_B= 7.5), 3.09 (m, 1H), 3.01 (q, 2H, *J*= 6.6), 2.81 (dd, 1H, J_A= 5.4, J_B= 12.6), 2.57 (d, 1H, *J*= 12.6), 2.18 (t, 2H, *J*= 7.8), 2.04 (t, 2H, *J*= 7.8), 1.64-1.37 (m, 8H), 1.37-1.23 (m, 4H); ^{13}C NMR (DMSO-*d6*, 150 MHz) δ 172.3, 171.8, 165.4, 162.7, 158.1, 145.1, 130.3, 128.0, 127.8, 61.0, 59.2, 55.4, 41.8, 38.3, 35.3, 35.2, 29.0, 28.2, 28.0, 26.2, 25.3, 25.0.

Preparation of TCO-modified antiVEGFR2 antibody.

AntiVEGFR2 antibody (eBioscience, 14-5821) (1mL, 500 μg, 3.34 nmol) was added to 6μL of (E)-cyclooct-4-enyl-2,5-dioxopyrrolidin-1-yl carbonate (TCO-NHS, 17.8 μg, 66.6 nmol) in DMSO (18 μL). The pH of the solution was adjusted to 9-9.5 by adding 10 μL of 1 M Na_2CO_3(aq). The solution was left on a shaker overnight at 4 °C. The desired product was isolated from excess TCO using an Amicon Ultra-0.5 Centrifugal filter (30 kDa) and washed with PBS three times. The molecular weight of the sample before and after the conjugation was determined by MALDI-TOF MS indicating an average of 2.8 TCO groups per antibody.

Cells and Culture Methods.

A431 (CRL-1740) cells were cultured in DMEM media supplemented with 10% fetal bovine serum and 1% penicillin streptomycin. H520 (HTB-182) cells were cultured in RPMI-1640 media supplemented with 10% fetal bovine serum and 1% penicillin streptomycin. SKOV-3 (HTB-77) cells were cultured in

McCoy's 5a media supplemented with 10% fetal bovine serum and 1% penicillin streptomycin. The cell lines were maintained at 37 °C under 5% CO_2.

Western Blot analysis.

VEGFR2-expression in H520 and A431 cell lysates was verified through immunoblotting. 10 μg of protein from each cell lysate were loaded on 10% Mini-PROTEAN TGX Precast gels. The protein extracts of the cell lysates were fractionated by SDS-PAGE and electro-transferred to polyvinylidene difluoride (PVDF) membranes. The PVDF membrane was incubated with a rabbit antiVEGFR2 primary antibody (Millipore 07-158) in a 1:250 dilution overnight at 4 °C. After washing the membrane with goat anti-rabbit secondary antibody (Jackson Immuno Research, 111-055-045) a chemiluminescent reagent (ECF substrate, GE RPN5785) was then applied to the membrane for 5 min and an image collected using a STORM 840 imaging system. β-actin (Cell Signaling Tech. 4970) was used as a protein loading control.

Preparation of Microbubbles (MBs).

Streptavidin coated MBs (MicroMarker Target-Ready contrast agents, VisualSonics) were reconstituted in 500 μL sterile saline (0.9% sodium chloride) according to the manufacturer's instructions. To prepare the tetrazine-coated MBs (MB_{Tz}), compound **5** (1.4 mg, 2.7×10^{-3} mmol) was dissolved in 1 mL of saline:MeOH (1:1 v/v) and 50 μL added dropwise to the reconstituted MBs. After 45 min, 200 μL of the solution was removed carefully with minimal agitation of

the bubbles and was discarded. Streptavidin coated magnetic beads (200 μL) were added whereupon after 20 min, 200 μL of solution was removed carefully and discarded and the sample placed beside a magnet. After decanting the solution MBs were rinsed with 200 μL saline and then transferred to another vial. MBs labeled with antiVEGFR2 (MB_V) were prepared similarly except that biotin-antiVEGFR2 (eBioscience 13-5821, 200 μL) was used in place of **5**.

VEGFR2 Binding Assay.

H520 cells (8×10^5) were plated in a 6 well plate 2 days prior to running the assay. Cells were washed with media (3 × 1 mL) before incubating with TCO-antiVEGFR2 (30 μg, 0.2 nmol) in media (1 mL) for 30 min at room temperature. Compound **5** (2.63 μg, 5 nmol) diluted in media (1 mL) was then incubated with the cells for another 15 min at room temperature followed by washing with media (3 × 1 mL). FITC-antiBiotin (300 μg, 2 nmol) diluted in media (1 mL) was added to the cells for 30 min before washing with PBS (3 × 1 mL). Cells were lysed in 1mL of 1 % Triton X-100 at 37 °C for 30 min and samples transferred to a 96 well plate and the fluorescence measured (Tecan infinite M1000). The excitation wavelength was 495 nm and emission monitored at 520 nm. To determine the amount of non-specific binding of **5** and FITC-antiBiotin, the fluorescence of cell lysates that had not been incubated with the TCO modified antibody were also measured. Furthermore, as a positive control, commercially available biotin-antiVEGFR2 (eBioscience 13-5821, 30 μg, 0.2 nmol) in media (1 mL) was

incubated with H520 cells and FITC-antiBiotin added subsequently and the fluorescence determined as described above.

Flow Chamber Cell Adhesion Assay.

H520 and A431 cells (8×10^5) were plated separately on 30 mm Corning tissue culture dishes 2 days prior to running the assay. For MB_{Tz} and associated control experiments TCO-antiVEGFR2 (30 μg) diluted in PBS (1 mL) was incubated for 30 min prior to running the assay. The parallel-plate flow chamber (Glycotech, Rockville, Md.) was connected to the tissue culture dish and the latter inverted. Using a syringe pump (PhD 2000, Harvard Apparatus, Holliston, USA) cells were first rinsed with PBS for 2 min, the MB solution for 4 min at a wall shear rate of 100 sec^{-1} (flow rate = 0.164 mL/min)[5] and subsequently with PBS for 2 min at 1000 sec^{-1} shear rate. Binding of MBs was visualized using a Celestron PentaView LCD Digital Brightfield Microscope with 20× objective. Movies and images were recorded and the extent of binding assessed by comparing the area covered by MBs to the total area covered by cells in each image using image analysis (FIJI) software.[6]

Animal Models.

All animal studies were approved by the Animal Research Ethics Board at McMaster University. Mice were maintained with 12 hour light/dark cycles and given food and water ad libitum. A431 (CRL-1555, VEGFR2−) and SKOV-3 (HTB-77, VEGFR2+) cells were purchased from ATCC. Female 4-5 week old

CD1 nu/nu mice (Charles River Laboratories, Wilmington, MA) were injected with 2.0×10^6 A431 or 2.6×10^6 SKOV-3 cells in Matrigel:DPBS (1:1) subcutaneously into the right flank. Ultrasound studies were performed 10 days following tumor inoculation.

Ultrasound (US) Imaging.

Non-linear contrast mode ultrasound imaging was performed using a Vevo 2100 imaging system (VisualSonics) and a 20 MHz high-frequency solid-state transducer (MS-250S; VisualSonics) having a lateral and axial resolution of 165 and 75 μm respectively. The focal length was 6.04 mm, transmit power was 4% and dynamic range was 35 dB. During imaging, animals were kept under anesthesia using isoflurane (3.5-4.5%) in medical air. Mice receiving TCO-labeled antibody were injected with 200 μL of TCO-antiVEGFR2 in PBS (0.5 μg/μL) 24 hours prior to imaging. MBs injections (approximately 6×10^7 MBs) were performed via the tail vein (70 μL). After 4 min a destruction-replenishment sequence was initiated [1] where 120 imaging frames were acquired before a continuous high power destruction pulse (100% transmit power) was applied to the MBs within the imaging window. Freely circulating MBs were allowed to refill into tumor vessels for 6 seconds before acquiring another set of 120 imaging frames. Images were analyzed using the Advanced Contrast Quantification Software Analysis Tool (VevoCQ, VisualSonics). Regions of interest were drawn over the area with highest vascularity in the tumors based on the distribution of

MBs observed following injection. The extent of binding in each case was determined by subtracting the average intensity over 120 frames acquired after destruction from the average intensity of the 120 frames acquired before destruction.[1]

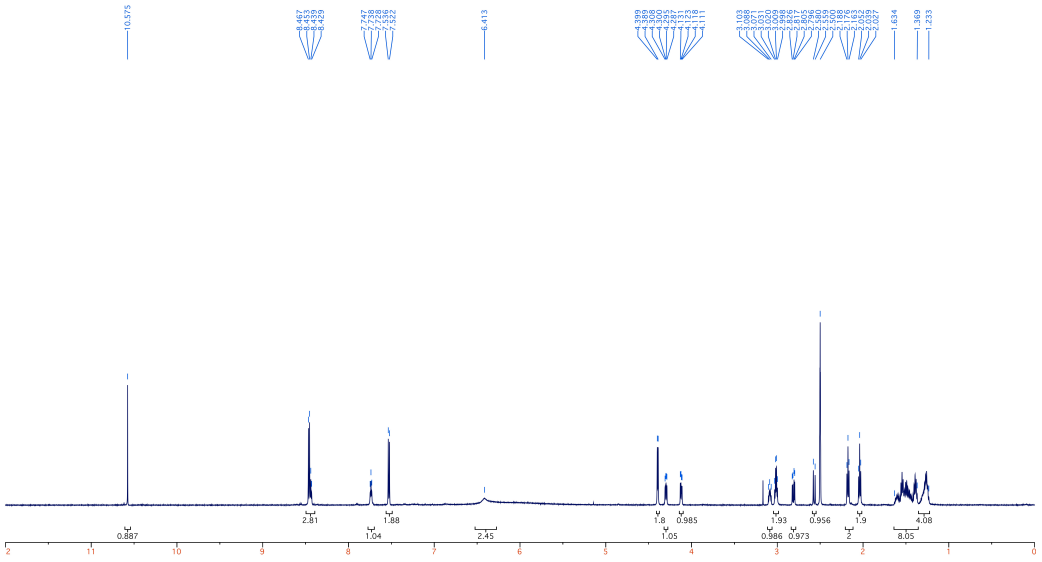

Figure S 3.1 ^{1}H NMR spectrum (DMSO-*d6*, 600 MHz) of *N*-(4-(1,2,4,5-tetrazin-3-yl)benzyl)-6-(5-((4*S*)-2-oxohexahydro-1*H*-thieno[3,4-*d*]imidazol-4-yl)pentanamido)hexanamide **(5)**

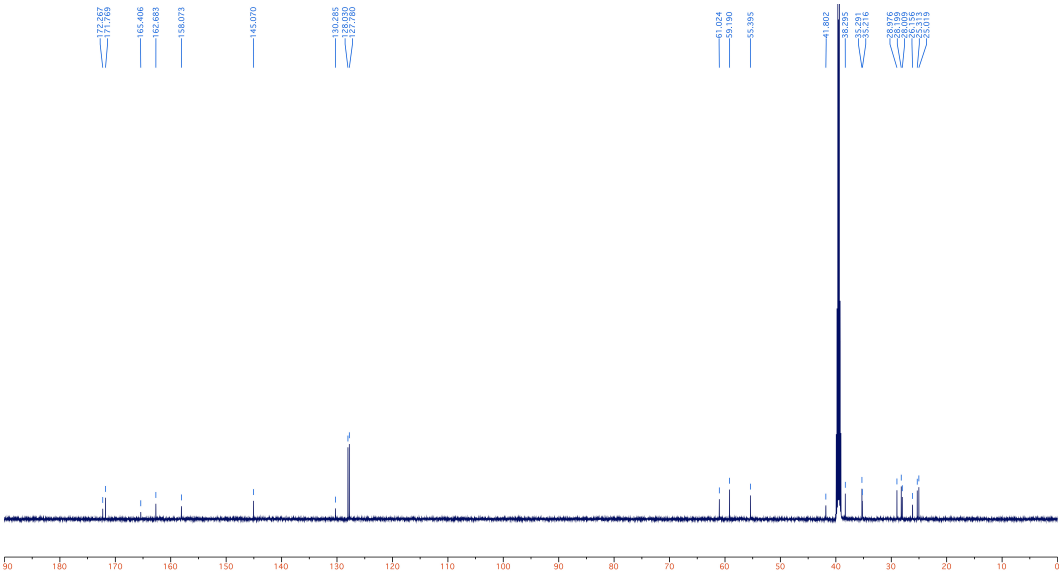

Figure S 3.2 ^{13}C NMR spectrum (DMSO-*d6*, 150 MHz) of *N*-(4-(1,2,4,5-tetrazin-3-yl)benzyl)-6-(5-((4*S*)-2-oxohexahydro-1*H*-thieno[3,4-*d*]imidazol-4-yl)pentanamido)hexanamide **(5)**

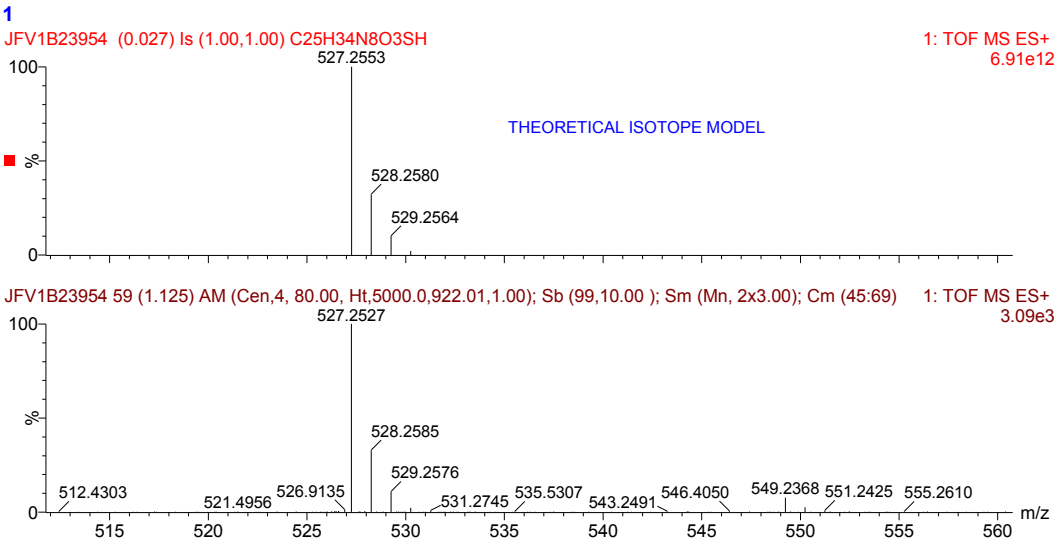

Figure S 3.3 HRMS (ESI+) of *N*-(4-(1,2,4,5-tetrazin-3-yl)benzyl)-6-(5-((4*S*)-2-oxohexahydro-1*H*-thieno[3,4-*d*]imidazol-4-yl)pentanamido)hexanamide **(5)**

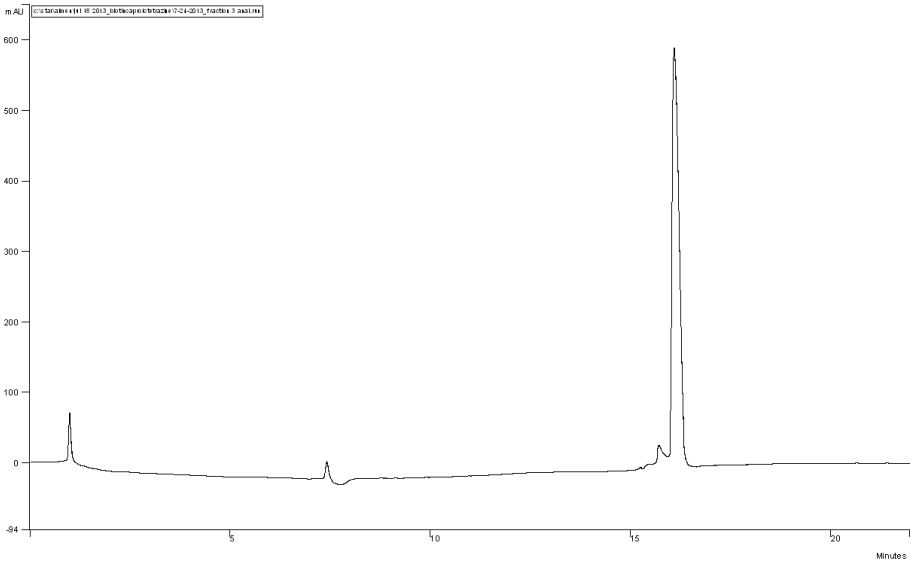

Figure S 3.4 Analytical HPLC (UV) trace of *N*-(4-(1,2,4,5-tetrazin-3-yl)benzyl)-6-(5-((4*S*)-2-oxohexahydro-1*H*-thieno[3,4-*d*]imidazol-4-yl)pentanamido)hexanamide **(5)**

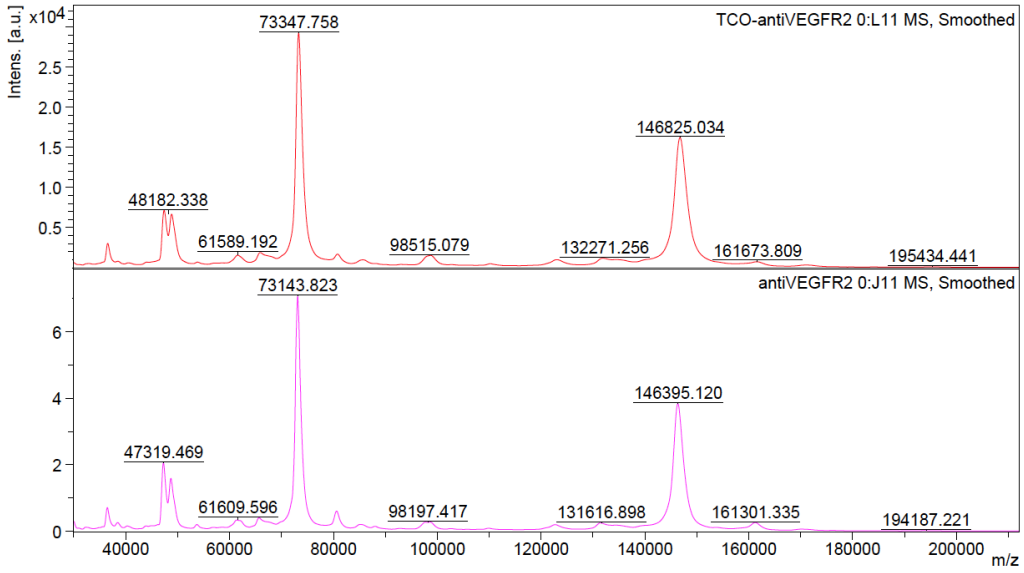

Figure S 3.5 MALDI-TOF analysis of TCO-antiVEGFR2 (**top**) and antiVEGFR2 (**bottom**)

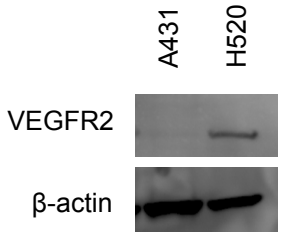

Figure S 3.6 Western blot analysis of VEGFR2 expression in A431 and H520 cell lysates

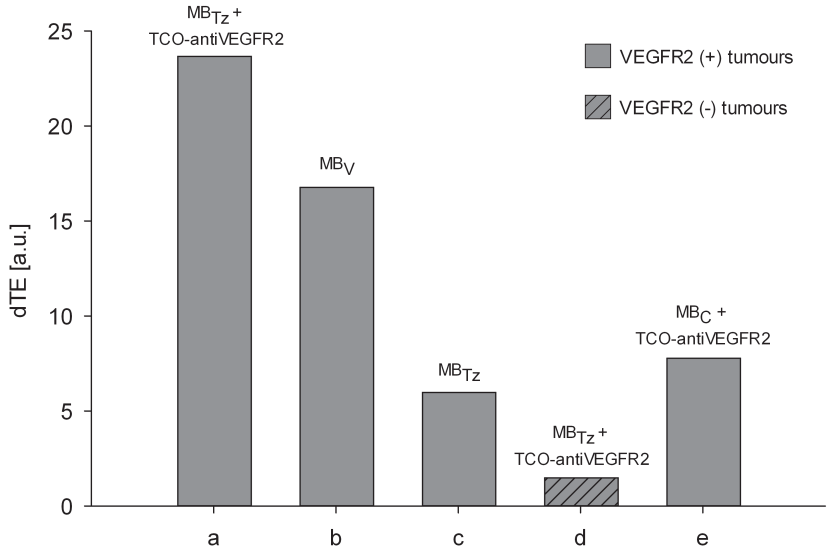

Figure S 3.7 Differential targeted enhancement (dTE) signal obtained from the ultrasound images. **(a)** MB_{Tz} + TCO-antiVEGFR2 **(b)** antiVEGFR2 targeted MBs (MB_V) **(c)** MB_{Tz} in the absence of TCO-antiVEGFR2 **(d)** MB_{Tz} + TCO-antiVEGFR2 in a VEGFR2(−) tumour model **(e)** unmodified MBs (MB_C).

References

[1] J. K. Willmann, R. Paulmurugan, K. Chen, O. Gheysens, M. Rodriguez-Pocel, A. M. Lutz, I. Y. Chen, X. Chen, S. S. Gambhir, *Radiology* **2008**, *246*, 508–518.

[2] D. S. Wilbur, D. K. Hamlin, R. L. Vessella, J. E. Stray, K. R. Buhler, P. S. Stayton, L. A. Klumb, P. M. Pathare, S. A. Weerawarna, *Bioconjugate Chem.* **1996**, *7*, 689–702.

[3] N. M. Green, *Biochem. J.* **1963**, *89*, 599-609.

[4] A. C. Morgan Jr, D. S. Wilbur, P. M. Pathare, *US Patent*, **2000**, 6083926.

[5] R. K. Jain, *Cancer Res.* **1988**, *48*, 2641–2658.

[6] J. Schindelin, I. Arganda-Carreras, E. Frise, V. Kaynig, M. Longair, T. Pietzsch, S. Preibisch, C. Rueden, S. Saalfeld, B. Schmid, J. Y. Tinevez, D. J. White, V. Hartenstein, K. Eliceiri, P. Tomancak, A. Cardona, *Nat. Methods* **2012**, *9*, 676–682.

APPENDIX II

Supporting Information for Chapter 4

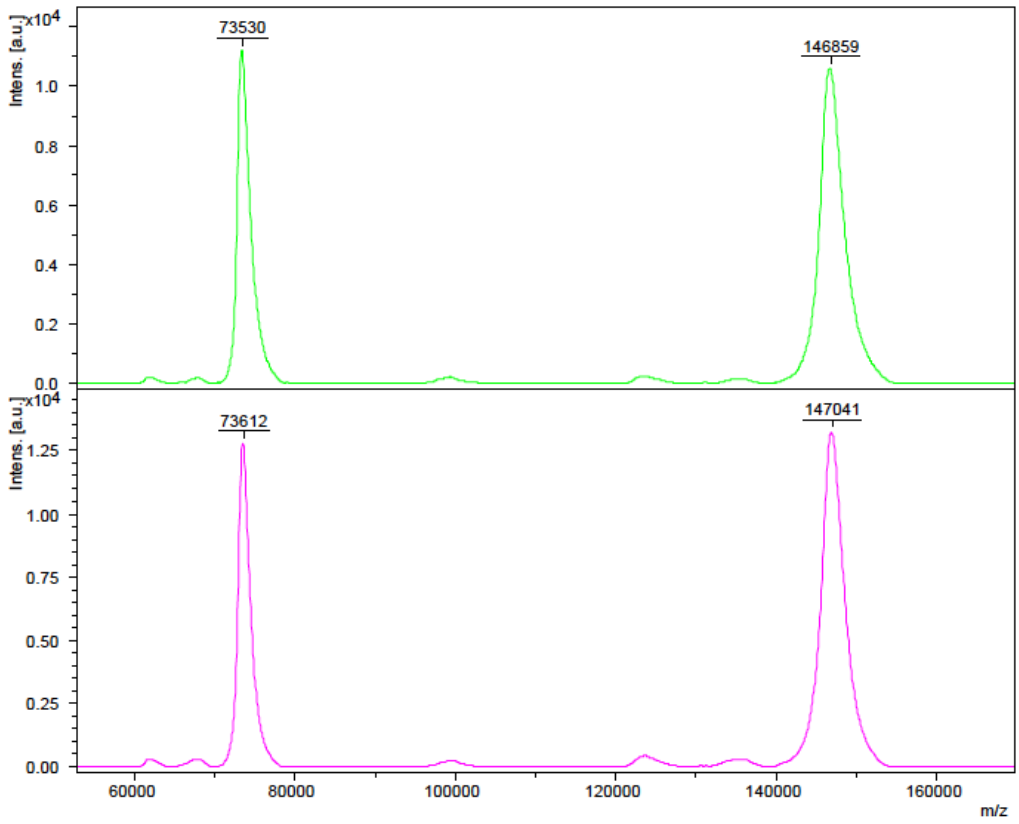

Figure S 4.1 MALDI-TOF MS analysis of J591 (**top**) and TCO-J591 (**bottom**). The difference in molecular weight between the two samples showed an average of 1.2 TCO molecules per antibody.

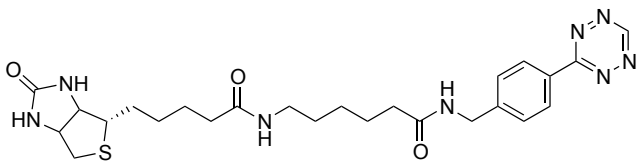

Figure S 4.2 Structure of biotin-Tz

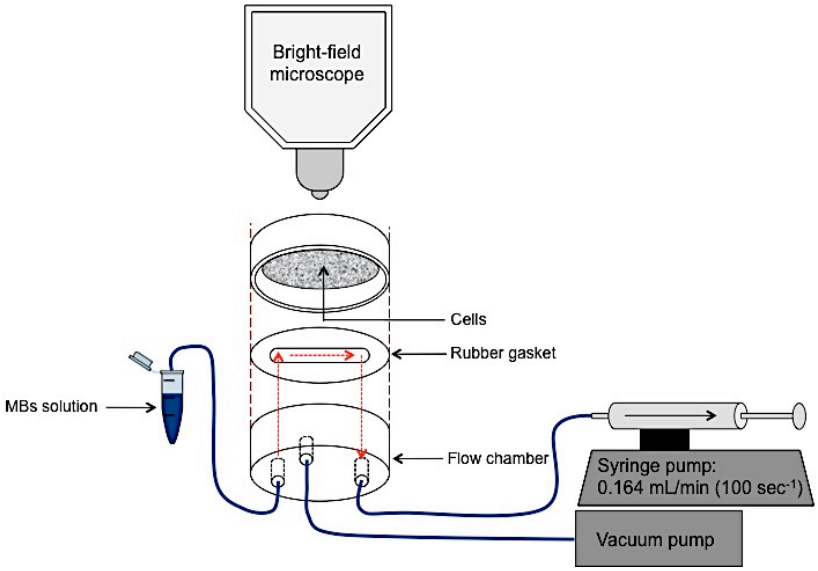

Figure S 4.3 Schematic diagram of the components and function of the parallel plate flow chamber used to test and visualize the binding of MBs to cultured cell lines. Flow conditions that result in a shear rate of 100 sec^{-1} were determined by application of the syringe pump.

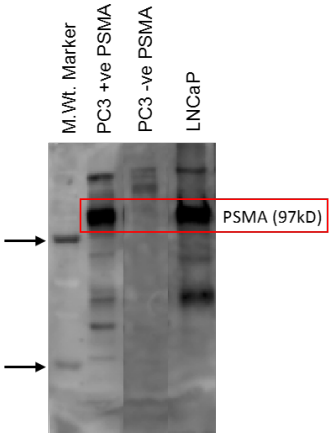

Figure S 4.4 PSMA protein expression by LNCaP and PC-3 cell lines compared by western blot. Cell lysates where from PSMA transfected (+ve) PC-3 cells, PSMA (-ve) PC-3 cells, and LNCaP cells grown in culture. Arrows indicate MW markers (75 and 25 kDa).

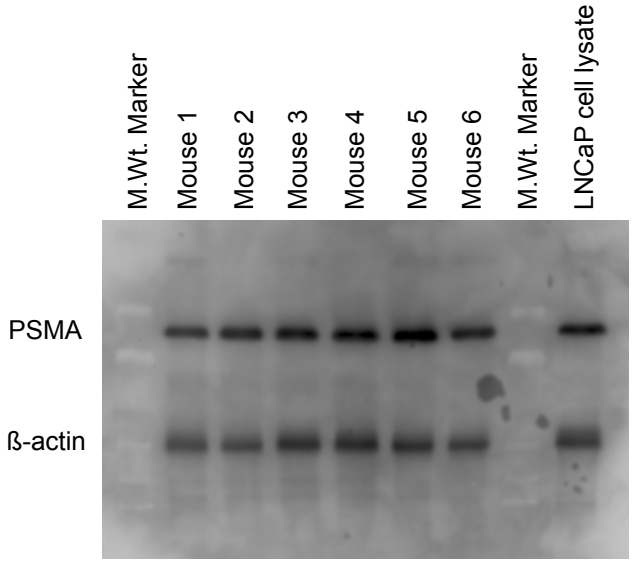

Figure S 4.5 Western Blot analysis of PSMA expressed by LNCaP tumors. Cell lysates were prepared and proteins separated by electrophoresis, before immunostaining for PSMA and β-actin. Top band indicates PSMA (97 kDa), and bottom band β-actin. Lysate from LNCaP cells grown *in vitro* are shown on right.

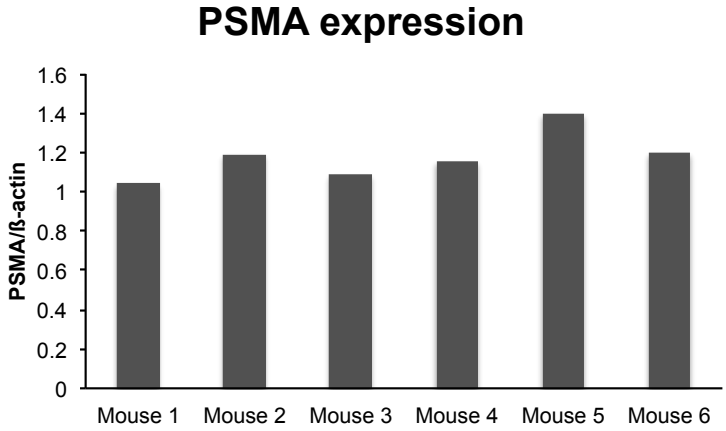

Figure S 4.6 PSMA protein expression in LNCap tumor lysates, analyzed by western blot and after normalizing to ß-actin levels. No significant difference in PSMA expression is among six tumors found (western image analysis was done using ImageQuant TL).

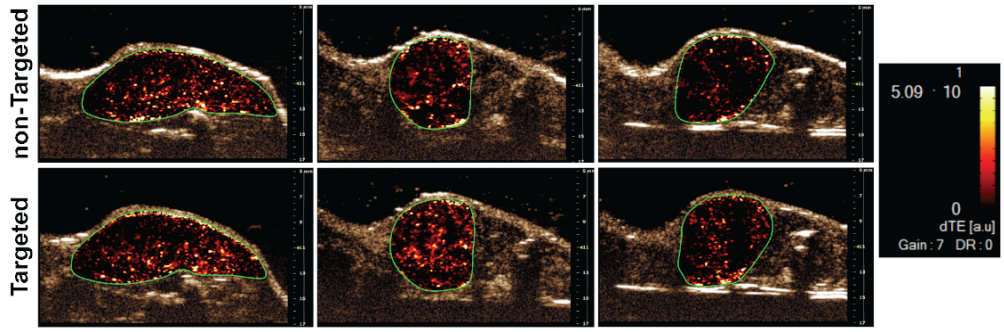

Figure S 4.7 Mice were given LNCaP xenograft tumors (green outline) as described in methods. Transverse color-coded parametric images overlaid on a nonlinear contrast mode ultrasound images were acquired 4 min after intravenous administration of either non-targeted MB_{Tz} (**top**) or direct PSMA-targeted $MB_{Tz\text{-}TCO}$-J591 (**bottom**). Signals are indicated by dTE= differential targeted enhancement (color scale, right).

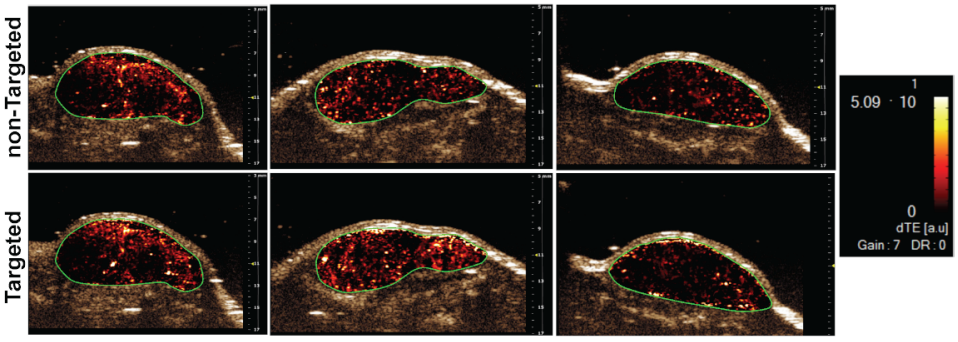

Figure S 4.8 Mice were given LNCaP xenograft tumors (green outline) as described in methods. Transverse color-coded parametric images overlaid on a nonlinear contrast mode ultrasound images were acquired 4 min after intravenous administration of either non-targeted MB_{Tz} (**top**) or direct PSMA-targeted $MB_{Tz\text{-}TCO}$-anti-hu/muPSMA (**bottom**). Signals are indicated by dTE= differential targeted enhancement (color scale, right).